

Fabrication and Optoelectronic Properties of Graphene Nanoribbons

THÈSE N° 5758 (2013)

PRÉSENTÉE LE 23 MAI 2013
À LA FACULTÉ DES SCIENCES DE BASE
LABORATOIRE DE SCIENCE À L'ÉCHELLE NANOMÉTRIQUE
PROGRAMME DOCTORAL EN PHYSIQUE

ÉCOLE POLYTECHNIQUE FÉDÉRALE DE LAUSANNE

POUR L'OBTENTION DU GRADE DE DOCTEUR ÈS SCIENCES

PAR

Eberhard Ulrich STÜTZEL

acceptée sur proposition du jury:

Prof. O. Schneider, président du jury
Prof. K. Kern, directeur de thèse
Prof. A. Kls, rapporteur
Dr T. Müller, rapporteur
Dr R. Sordan, rapporteur



ÉCOLE POLYTECHNIQUE
FÉDÉRALE DE LAUSANNE

Suisse
2013

Abstract

Graphene, a single layer of carbon atoms, exhibits excellent charge transport properties. However, due to the absence of a band gap in this two-dimensional carbon nanostructure, graphene-based field effect transistors cannot be turned off. One strategy to increase the on/off ratio relies on patterning graphene into narrow stripes, so-called graphene nanoribbons (GNRs). The present thesis aimed at developing novel fabrication and chemical functionalization methods for GNRs. Along these lines, electrical transport studies and spectroscopic investigations were envisioned as a major tool to monitor the changes brought about by the functional groups attached to the GNRs.

GNRs were fabricated with the aid of V_2O_5 nanofibers or CdSe nanowires as an etching mask during the plasma etching of graphene. The resulting GNRs exhibited good electrical conductivity for ribbon widths as small as 10 nm. Moreover, the transport gap in the GNRs was found to scale inversely with the ribbon width. Scanning tunneling microscopy and surface enhanced Raman spectroscopy testified a good structural quality of the GNRs.

Electrical characterization of GNRs revealed a pronounced hysteresis, which was exploited for the fabrication of electrically switchable GNR memory cells. Dynamic pulse response measurements demonstrated reliable switching between two conductivity states for clock frequencies of up to 1 kHz and pulse durations as short as 500 ns for $>10^7$ cycles. As the most likely switching mechanism, charge trapping within a water layer in the GNR surrounding could be identified.

Furthermore, the optoelectronic properties of individual GNRs were studied by scanning photocurrent microscopy. The pronounced photocurrent signal close to the nanoribbon/metal contacts was found to be directly proportional to the conductance of the devices, suggesting that a local voltage source is generated at the nanoribbon/metal interface by the photo-thermoelectric Seebeck effect. The dominance of this mechanism over charge separation via built-in electrical fields was attributed to

strong local heating of the GNRs by the laser spot, combined with the reduced thermal conduction capability of the nanoribbons in comparison to extended graphene sheets.

Chemical functionalization of graphene and GNRs was attempted via different gas- and liquid-phase approaches. While electrical transport and Raman measurements revealed the presence of significant doping effects, it was not possible to unequivocally prove the covalent attachment of atoms at the GNR edges, neither through changes in the charge transport characteristics, nor via scanning microscopy studies.

Keywords : graphene, graphene nanoribbons, nanoscale, field effect transistors, optoelectronics, metal contacts, data storage, functionalization

Zusammenfassung

Graphen, eine atomar dünne Kohlenstoffschicht, zeichnet sich durch exzellente elektronische Eigenschaften aus. Jedoch besitzt es keine Bandlücke, weshalb Graphen-basierte Feldeffekttransistoren nicht in den Aus-Zustand gebracht werden können. Ein Ansatz um das An/Aus-Verhältnis zu erhöhen ist die Strukturierung von Graphen in schmale Streifen, sogenannte Graphen-Nanostreifen (GNS). Die vorliegende Arbeit zielte darauf ab, neue Herstellungs- und chemische Funktionalisierungsmethoden für GNS zu entwickeln. Hierfür wurden elektrische Transportmessungen und spektroskopische Untersuchungen durchgeführt, mit dem Ziel Änderungen aufgrund der Anbindung funktionaler Gruppen an die GNS zu beobachten.

GNS wurden durch Plasmaätzen aus Graphen mit Hilfe von V_2O_5 Nanofibern oder CdSe Nanodrähten als Ätzmaske gewonnen. Die resultierenden GNS zeigten eine gute elektrische Leitfähigkeit für Breiten hinab zu 10 Nanometern. Darüber hinaus wurde gefunden, dass die Transportbandlücke in den GNS reziprok mit der Nanostreifen-Breite skaliert. Mit Hilfe von Rastertunnelmikroskopie sowie oberflächenverstärkter Raman-Spektroskopie ließ sich eine hohe strukturelle Qualität der GNS nachweisen.

Die elektrische Charakterisierung von GNS zeigte eine ausgeprägte Hysterese, welche für die Herstellung von elektrisch schaltbaren GNS Speicherelementen genutzt wurde. Messungen unter Anlegen von definierten Spannungspulsen ergaben zuverlässiges Schalten zwischen zwei Leitfähigkeitszuständen für Taktfrequenzen von bis zu 1 kHz und Pulsdauern von nur 500 Nanosekunden über mehr als $>10^7$ Zyklen. Als Ursache für die Hysterese wurde das Einfangen von Ladungsträgern in einer dünnen Wasserschicht in der Umgebung der GNS ausgemacht.

Weiterhin wurden die optoelektronischen Eigenschaften einzelner GNS mit Hilfe orts aufgelöster Photostrom-Messungen untersucht. Ein deutliches Photostromsignal

wurde nahe den Metallkontakten beobachtet, welches sich proportional zur Leitfähigkeit der Proben verhielt. Dies wurde auf eine lokal durch den photo-thermoelektrischen Seebeck Effekt erzeugte Spannungsquelle zurückgeführt. Die Dominanz dieses Mechanismus gegenüber dem photoelektrischen Effekt (Trennung von Elektron-Loch-Paaren durch interne elektrische Felder) wurde durch eine starke lokale Erwärmung erklärt, die durch den Laserstrahl in Kombination mit einer reduzierten thermischen Leitfähigkeit der GNS im Vergleich zu ausgedehntem Graphen verursacht wird.

Schließlich wurden unterschiedliche Gas- und Flüssigphasen-basierte Methoden eingesetzt, um eine chemische Funktionalisierung von Graphen und GNS zu erreichen. Mit Hilfe von elektrischen Transportmessungen und Ramanspektroskopie konnte eine deutliche Dotierung nachgewiesen werden. Allerdings konnte weder anhand von Änderungen im Ladungstransportverhalten, noch mittels mikroskopischer Untersuchungen ein eindeutiger Nachweis für die kovalente Anbindung von Atomen an die GNS Kanten erbracht werden.

Schlagwörter : Graphen, Graphen-Nanostreifen, Nanoskala, Feldeffekttransistor, Optoelektronik, Metallkontakt, Datenspeicherung, Funktionalisierung

Contents

Abstract	iii
Zusammenfassung	v
1. Introduction	1
2. Basics of graphene and graphene nanoribbons	7
2.1. Sp ² -hybridized carbon nanomaterials	7
2.2. Electronic properties	8
2.3. Raman spectroscopy	12
2.4. Surface enhanced Raman spectroscopy	14
2.5. Optoelectronic properties	15
3. Experimental techniques	17
3.1. Atomic force microscopy	17
3.2. Scanning tunneling microscopy	18
3.3. Electron microscopy	19
3.4. Confocal Raman spectroscopy	21
3.5. Scanning photocurrent microscopy	22
4. Graphene nanoribbon fabrication and structural characterization	25
4.1. Nanofiber/nanowire etching masks	25
4.2. V ₂ O ₅ nanofiber mask	26
4.3. CdSe nanowire mask	31
5. Surface enhanced Raman spectroscopy of graphene nanoribbons	37
5.1. Graphene nanoribbons	37
5.2. Mechanism of surface enhancement	40

6. Graphene nanoribbon memory cell	47
6.1. Electrical characterization of the graphene nanoribbons	47
6.2. Memory effect	49
6.3. Dynamic pulse response measurements	50
6.4. Origin of hysteresis	51
6.5. Influence of etching time on hysteresis and device operation	53
7. Spatially resolved photocurrents in graphene nanoribbon devices	57
7.1. Electrical characterization of the graphene nanoribbons	59
7.1.1. CdSe nanowire etching mask removed	59
7.1.2. CdSe nanowire left on top	60
7.2. Photocurrent measurements	61
7.2.1. Built-in electric field model	62
7.2.2. Photo-thermoelectric Seebeck effect	64
8. Edge functionalization of graphene	67
8.1. Functionalization by bromine	67
8.2. Graphite step edges exposed to Br ₂	68
8.3. Electrical and Raman characterization of Br ₂ -treated graphene	68
8.4. Scanning tunneling microscopy of Br ₂ -treated graphite edges	69
8.5. Transmission electron microscopy of graphene exposed to Br ₂	70
9. Low temperature transport through graphene nanoribbon quantum dots	73
9.1. Single-electron charging behavior	73
9.2. Excited states	75
9.3. Possible Kondo features	76
9.4. Functionalization of graphene nanoribbons	79
9.4.1. Gas phase approach: Hydrogenation	79
9.4.2. Liquid-phase approach: Cobalt ions	82
10. Summary and outlook	85
A. Appendix: Photocurrent data of graphene nanoribbons	89
B. Appendix: Abbreviations	91

C. Appendix: Publications	93
Bibliography	95
Curriculum vitae	117
Acknowledgements	119

1. Introduction

The development of the transistor - the fundamental building block of modern electronic circuits - in the late 1940's, complemented by Richard Feynman's inspiring concept of "nanotechnology" put forward several years later, triggered a scientific and technological revolution (see figure 1.1 for the first transistor).[1, 2] This advancement was strongly promoted by the invention and further development of scientific instruments, in particular the transmission electron microscope, the scanning tunneling microscope, and the laser.[3, 4] Additional impetus came from newly devised approaches to high purity materials, as well as the transition in semiconductor technology from germanium to silicon already in the 1960's, followed by an increasing miniaturization of the circuits.[5] In the 1970's, gallium arsenide then moved into the center of interest, with respect to both, technological development and fundamental research. The subsequent improvements in vacuum physics and the development of molecular beam epitaxy provided access to high quality two-dimensional electron gas systems embedded in three-dimensional semiconductor heterostructures.[6, 7]



Figure 1.1.: The first transistor from Bell Labs.[8]

More recently, graphene representing a one-atom thick layer of carbon atoms arranged in a honeycomb lattice has attracted enormous attention from both the experimental and theoretical scientific communities.[9] Even though monolayer graphene had been isolated before,[10] it took until the year 2004 to obtain individual graphene sheets suitable for device fabrication. On this basis, the first field-effect transistor (FET) comprised of a truly two-dimensional material could be demonstrated for the first time.[11] Previously, two-dimensional crystals were often presumed not to exist in the free state, because thermal fluctuations should induce melting of the crystal.[12, 13, 14, 15] It is currently believed that graphene is stable because it is not perfectly flat, but exhibits microscopic corrugations on the scale of 1 nm.[16]

Several features render graphene's electronic properties unique. Most prominently, carriers in graphene are described by a Dirac-like equation rather than the Schrödinger equation, opening the possibility to explore relativistic quantum phenomena in a bench top experiment.[17, 18] Moreover, graphene exhibits Klein tunneling, i.e., the transmission of the Dirac fermions encountering a potential step at normal incidence is 100 %, independent of height and width of the barrier.[19, 20] However, experimentally exploiting the full spectrum of graphene's outstanding electronic properties requires specific strategies such as combining it with other two-dimensional crystals (see figure 1.2a).[21, 22, 23] For instance, graphene deposited on a boron nitride sheet has been reported to reach significantly enhanced carrier mobilities compared to graphene on Si/SiO₂ substrates.[24]

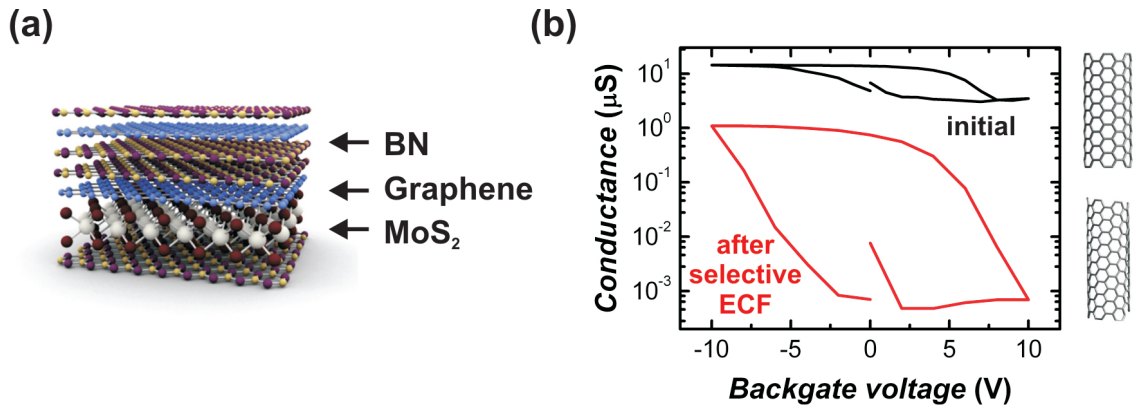


Figure 1.2.: (a) Example of a heterostructure composed of different two-dimensional crystals. Adapted from reference [23]. (b) Increase of on/off ratio in a network of single-walled carbon nanotubes. After functionalization of the metallic nanotubes, only semiconducting nanotubes contribute to the charge transport. Adapted from reference [25].

With respect to technological applications, graphene's tunable electrical ambipolar behavior, near-ballistic transport at room temperature, as well as high mobility render it into a promising, novel component of devices like nanometer-scale FETs.[26, 27, 28, 29] Prototypes like electronic analog or optoelectronic devices have already been demonstrated from graphene.[30, 31, 32, 33, 34, 35, 36] Ultimately, progress in this direction may help to overcome the limits of silicon-based technology expected at the sub-10 nm scale.[37] Owing to its high optical transparency and mechanical stability, graphene is also attractive for application in flexible electronics.[38, 39] Furthermore, due to its high surface area and good biocompatibility, graphene represents a close-to-ideal component of (bio)sensors.[40, 41] For technological applications monolayers obtained via the so-called scotch tape method are too small in size.[11] Hence, production methods yielding large graphene sheets with good quality (low defect density) are currently developed, e.g. the reduction of graphene oxide, the epitaxial growth on silicon carbide, or chemical vapor deposition on metal substrates.[42, 43, 44]

The absence of a band gap in graphene prevents the possibility to turn off graphene FETs, which strongly limits their use in digital electronic circuits. Several ways exist for the introduction of a band gap in graphene. The attachment of atomic hydrogen to each carbon atom of the graphene lattice creates graphane. This functionalization is accompanied by a change of the hybridization of carbon atoms from sp^2 into sp^3 , thus removing the conducting π band and opening an energy gap.[45] However, it is difficult to realize an ordered hydrogen pattern. In case of bilayer graphene, the combined action of a top and a bottom gate allows not only to control the carrier density, but also to apply a vertical electric field, which breaks the inversion symmetry of the two layers and thus leads to the opening of a tunable band gap between valence and conduction bands.[46] Unfortunately, a quite large voltage in the range of 100 V is required to obtain a reasonable band gap of approximately 250 meV.[47] In addition, the necessity of the top gate complicates the device fabrication and limits the application perspective of such a device.

Another strategy to increase the on/off ratio consists of patterning graphene into narrow stripes, so-called graphene nanoribbons (GNRs), where carrier confinement and edge effects introduce a band gap. GNRs are of particular interest as device components, as the geometry and chemical termination of their edges may enable control over their electronic, charge transport and magnetic properties, which may be exploited to improve the performance of corresponding devices.[48, 49, 50, 51] The impact of the edges is predicted to sensitively depend on their precise atomic structure, the presence of warping or scrolling-like relaxations, as well as the chemical nature of the end groups.[52, 53, 54] Numerous theory studies predict that chemical

edge functionalization is able to tune the band structure of GNRs from metal to insulator by changing the C-C bond lengths and bond angles near the GNR edges,[55] to render them less sensitive to edge irregularities because of the conversion of edge-localized HOMO and LUMO states to delocalized extended states,[56] or to enhance the local spin alignment.[57, 58] The latter property may be exploited to achieve spin-polarized metallic edge currents along zigzag edges at low temperatures, which could open novel spintronic applications.[18, 59] In general, graphene is highly suitable for spintronics due to its small spin-orbit interaction and the small influence of nuclear magnetic moments in carbon.[60] However, up to now reliable methods to attach specific functional groups to the edges of graphene are still lacking. In fact, thus far developed chemical functionalization methods for graphene mainly involve the non-covalent adsorption of electron donor or acceptor molecules, or the covalent surface functionalization with reactive species like radicals, similar to the covalent functionalization of carbon nanotubes (CNTs).[61, 62, 63] The attached moieties are distributed over the entire carbon nanostructure surface, where they act as scattering centers that substantially reduce the carrier mobility.[64] Conceptually, the spatial separation of functional groups at the edges from the GNR center is advantageous, since in this manner the carrier mobility could be largely preserved, similar to transfer doping in two-dimensional electron gas heterostructures. The available chemical functionalization methods for CNTs, which have for instance provided access to all-semiconducting nanotubes suitable as transistor channels (see figure 1.2b), witness the strong potential of chemical tailoring of the properties of carbon nanostructures.

The present thesis endeavored to develop novel methods for fabricating and chemically functionalizing GNRs. As a major difference compared to previous fabrication schemes, two novel one-dimensional etching masks were utilized. In the pioneering experiments in 2007, e-beam patterning and subsequent isotropic oxygen plasma etching of mechanically exfoliated graphene were used to create the first GNRs with a width above 20 nm and an edge roughness of several nanometers, which resulted in an inactive region not participating in charge transport.[65, 66] The novel one-dimensional etching masks should yield narrower GNRs with smoother edges, leading to less edge disorder and hence less influence of localized defect edge states. Additionally, these masks promised the advantages of (i) a rectangular instead of circular cross-section, which should help to reduce the undercut during plasma etching (in case of V_2O_5 nanofibers), and (ii) an easy and smooth removal after the etching step (in case of both, V_2O_5 nanofibers and CdSe nanowires). Another goal was to perform chemical edge functionalization in a more controlled manner from the gas phase instead of using quite reactive agents in solution, an approach that has been pursued in most previous works in this field. By leaving the one-dimensional etching masks on top of the obtained GNRs as a protection for the bulk of the GNR

during the gas phase-functionalization, it was intended to restrict the reaction to the GNR edges. To this end, graphite edges (as a test system) and GNRs were exposed to bromine vapor at higher temperatures, or plasma-generated hydrogen atoms at room temperature. The saturation of GNR edges with bromine atoms has been theoretically predicted to enhance their magnetic properties (magnetic order, anisotropy, crossover temperature, spin correlation length).[51] As an alternative approach to magnetic GNRs, devised to alleviate the restriction to zigzag nanoribbons, the attachment of hydrogen atoms to the ribbon edges could lead to spin-carrying groups.[67] Hydrogen termination of GNRs has been predicted to be useful for spintronics applications.[68, 69, 70, 71] On this basis, successful covalent edge modification should be proven by the detection of changes in the electrical and spectroscopic properties of the ribbons. The major objective with regard to the electronic, charge transport and magnetic properties was to explore their dependence on both, the ribbon structure (microscopic structure and geometry) as well as the chemical nature of the edge groups, in order to identify possible nanoscale effects in these carbon nanostructures.

This thesis is organized as follows:

Chapter 2 gives an overview of the basic concepts for graphene and GNRs, in order to establish a basis for discussing the experimental results in the later chapters. After introducing the different types of carbon nanostructures, emphasis is laid on the electronic and vibrational properties of graphene and GNRs, followed by a description of the optoelectronic properties of graphene.

Chapter 3 introduces the used experimental techniques, which allow sample characterization on the nanoscale. After the motivation for the use of a particular instrument, its working principle and limitations will be explained.

In **chapter 4**, the GNR fabrication with the aid of the two different etching masks is presented in detail. This is complemented by the structural characterization of the ribbons with the aid of scanning force microscopy and electron spectroscopy, respectively.

Chapter 5 addresses the vibrational properties of individual, narrow GNRs, as determined by surface-enhanced Raman spectroscopy (SERS). Subsequently, gate voltage-dependent SERS measurements on silver nanoparticle-decorated graphene are described, whose aim was to determine the mechanism of enhancement.

Chapter 6 focuses on the electrical characterization of GNR memory devices obtained using the V_2O_5 nanofiber etching mask, with emphasis on their dynamical response and the origin of the hysteresis in the transfer curves of the devices.

Chapter 7 deals with the optoelectronic properties of GNRs prepared with CdSe nanowires as etching mask. Here, the main emphasis is on the determination of the mechanism underlying the photocurrent generation close to the metal contacts.

Following the structural, vibrational, and electrical characterization of GNRs in the preceding chapters, the topic of **chapter 8** is the edge functionalization of graphene nanostructures. This involves the use of microscopic techniques to test the possibility of gas phase edge functionalization by bromine.

In **chapter 9**, a different approach to prove the edge functionalization of GNRs is described. It is based on low temperature transport measurements of GNRs which due to their short length behave as quantum dots. The Coulomb charging characteristic of these dots was analyzed with respect to the possible emergence of Kondo features.

Finally, **chapter 10** provides a summary of the most relevant results, combined with an outlook on possible future research directions.

2. Basics of graphene and graphene nanoribbons

2.1. sp^2 -hybridized carbon nanomaterials

Several carbon allotropes with sp^2 -hybridization exist. Graphene, a layer of carbon atoms arranged into a two-dimensional hexagonal lattice, is a single layer of graphite (figure 2.1a).[11] Fullerene molecules (e.g. C_{60}) are obtained by wrapping graphene, combined with the introduction of pentagons into the hexagonal lattice (figure 2.1b).[72] Carbon nanotubes (CNTs) represent rolled-up cylinders of graphene (figure 2.1c). The chirality of single-walled CNTs determines whether they are metallic or semiconducting.[73, 74, 75]

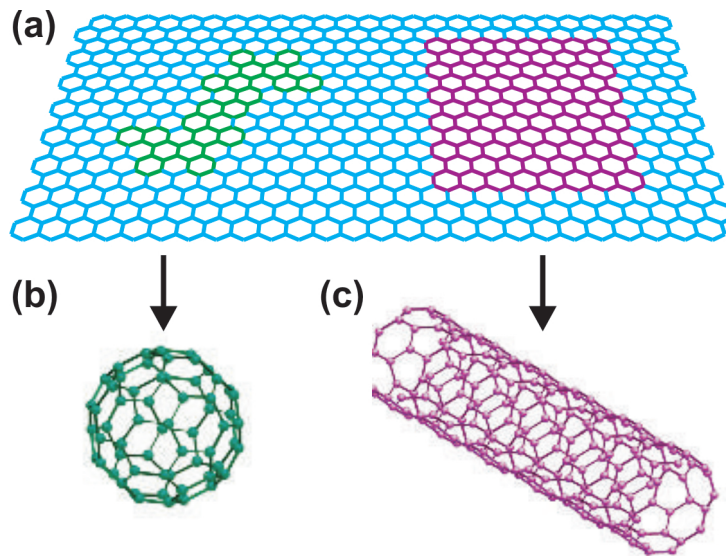


Figure 2.1.: (a) Graphene, a honeycomb lattice of carbon atoms. (b) Fullerenes (e.g. C_{60}) are molecules consisting of wrapped graphene. (c) Carbon nanotubes are rolled-up cylinders of graphene. Adapted from reference [17].

The six electrons of a carbon atom in the ground state reside within/occupy the orbitals $1s$, $2s$, $2p_x$, $2p_y$ and $2p_z$. The configuration in the ground state is $1s^2 2s^2 2p^2$. The sp^2 -hybridization of the double occupied $2s$ orbital and two $2p$ orbitals (e.g. p_x and p_y) leads to a trigonal planar structure, with an in-plane σ bond between two neighboring carbon atoms that are separated by 1.42 \AA . [18] The hexagonal graphene lattice can be seen as a triangular lattice with a basis of two atoms per unit cell (highlighted by blue and red color in figure 2.2a). Additionally, the singly occupied p_z orbital of a carbon atom, which is perpendicular to the planar structure, binds with the p_z orbitals of neighboring carbon atoms, leading to the formation of a delocalized π band, which is half filled. [18] This half filled band is the basis for the semimetallic properties of graphene.

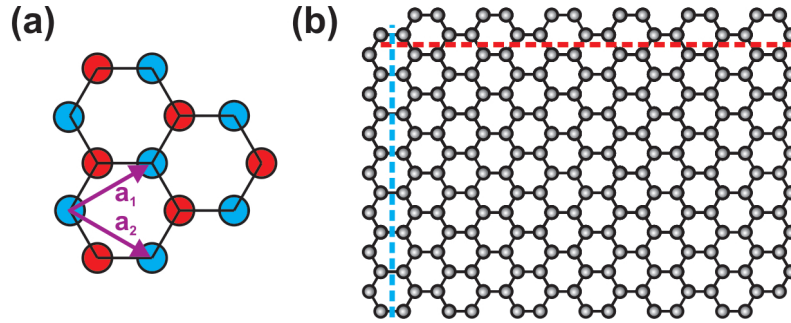


Figure 2.2.: (a) Graphene's triangular lattice with a basis of two atoms (red and blue). \mathbf{a}_1 and \mathbf{a}_2 are the lattice vectors. (b) Zigzag (blue) and armchair edges (red) of graphene.

Narrow stripes of graphene are called graphene nanoribbons (GNRs). [76, 77] Figure 2.2b shows the two basic edge types, namely zigzag (blue) and armchair edges (red). However, GNRs can have a random chirality. Additionally, the edges can be rough, i.e., they comprise a mixture of zigzag and armchair type segments. There are several possibilities for the edge termination, like the presence of functional groups.

2.2. Electronic properties

The hexagonal lattice in real space transforms into a hexagonal lattice in reciprocal space. The energy band structure of graphene can be obtained by tight-binding calculations (see figure 2.3a): [18, 78]

$$E_{\pm}(\mathbf{k}) = \pm t \sqrt{3 + f(\mathbf{k})} - t' f(\mathbf{k}), \text{ with}$$

$$f(\mathbf{k}) = 2 \cos(\sqrt{3} k_y a) + 4 \cos\left(\frac{\sqrt{3}}{2} k_y a\right) \cos\left(\frac{3}{2} k_x a\right),$$

where a is the graphene lattice spacing of 2.46 Å, t (~ 2.8 eV) the nearest-neighbor hopping energy, and t' the next nearest-neighbor hopping energy (≤ 0.1 eV). Close to the \mathbf{K} and \mathbf{K}' points in the Brillouin zone, the band structure can be approximated by $\mathbf{E}(\mathbf{q}) = \pm \hbar \cdot v_F \cdot |\mathbf{q}|$, with $v_F \approx 10^6$ m/s and $\mathbf{k} = \mathbf{K} + \mathbf{q}$. [78] Hence, graphene is a semimetal with an unusual linear dispersion relation. Since for low energies, electrons in graphene can be described as massless Dirac fermions, the cones at the \mathbf{K} and \mathbf{K}' points are called Dirac cones. For undoped graphene, the Fermi level is located at the intersection of the cones. This charge neutrality point is also called the Dirac point. The Fermi level in graphene can be shifted by an electric field via a gate electrode into the hole (negative voltage range in figure 2.3b) or electron regime (positive voltage range), depending on the polarity of the applied field. The change in carrier concentration n results in an ambipolar change in conductivity $\sigma = e \cdot n \cdot \mu$ and hence in resistance (e is the elementary charge and μ the mobility). [11] The peculiarity of two inequivalent sublattices (\mathbf{K} and \mathbf{K}' points) in combination with the two possible spin states of an electron (up, down) leads to a fourfold degeneracy, which manifests itself in an unconventional quantum Hall effect. [79, 80]

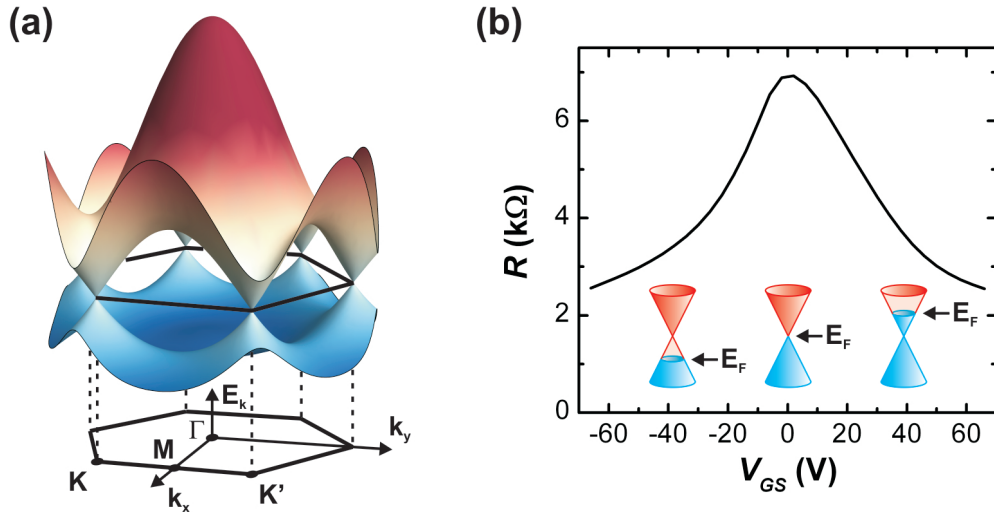


Figure 2.3.: (a) The electronic dispersion of the π bands in the Brillouin zone of graphene. For low energies, the dispersion relation of electrons (holes) is linear, and can be described by cones around the \mathbf{K} and \mathbf{K}' points. (b) Two probe resistance R in dependence of the gate-source voltage V_{GS} applied to a graphene sheet under ambient conditions. Inset: Dirac cone for different Fermi level positions. Blue: occupied states, red: unoccupied states.

Due to the absence of a band gap in graphene and the formation of electron-hole puddles, graphene-based field effect transistors (FETs) cannot be turned off (see finite resistance at $V_{GS} = 0$ V in figure 2.3b), thus limiting their use in electronics.[81] One strategy to increase the on/off ratio relies upon patterning graphene into GNRs. The on/off ratio is usually determined by dividing the electrical resistance at the Dirac point by the resistance determined well within the n- or p-type regime (e.g. at $|V_{GS}| = 30$ V).

Theoretical studies based on tight-binding approximations predict, that GNRs are metallic or semiconducting depending on the crystallographic direction of the ribbon axis and the width, similar to CNTs.[76, 77] For the semiconducting GNRs, the band gap decreases with increasing ribbon width, approaching zero in the limit of very wide GNRs.[77] The main difference between CNTs and GNRs is the existence of edges in GNRs and a relaxation of the carbon-carbon bond length from the center of the GNR toward the GNR edge region.

Density functional theory calculations have shown, that both types of edges have energy band gaps with $E_{gap} = \frac{\alpha}{W_G}$ (α ranges between 0.2-1.5 eVnm, W_G is the GNR width).[48, 82] The determining factors in the semiconducting behavior of armchair GNRs are quantum confinement and edge effects (change in bond length at the edges). Additionally, in case of zigzag GNRs the gap is influenced by antiferromagnetic interaction between magnetic edge states on the opposite edges, where the edge atoms are located on different sublattices.[82]

The pioneering experimental transport measurements on GNRs have revealed semiconducting behavior,[65, 66] independent of their crystallographic orientation. Additionally, the above models were not able to explain the observations of Coulomb diamonds (CDs) in etched GNRs, as well as the on/off ratios in wider GNRs (>20 nm), which are much higher than theoretically predicted.[83, 84] This has led to the inclusion of localized states that dominate the charge transport due to bulk and edge disorder in the theoretical models. A model based on Coulomb blockade in disordered systems can explain the observed transport through GNRs. Distinction has been made between the so-called "transport gap" (suppressed conductance in a limited gate-source voltage range) and the "drain-source gap" (suppressed conductance in a limited drain-source voltage range). The drain-source gap can be interpreted as the renormalized charging energy of strongly coupled quantum dots (QDs), and expressed as $E_{gap}(W_G) = \frac{\alpha}{W_G} e^{-\beta W_G}$ ($\alpha = 2$ eV nm, $\beta = 0.026$ nm⁻¹).[85, 86] QDs can be formed along the GNR in the presence of a quantum confinement gap, combined with a strong bulk and/or edge-disorder potential (see figure 2.4), leading to the drain-source gap.[83, 84] The quantum confinement gap ensures that real tunneling

takes place instead of Klein tunneling (transmission probability of 1). [19, 20] There are several QDs in parallel and/or in series in a long GNR, which causes the CDs to overlap. A short GNR device, by comparison, is likely to consist of only a few QDs or even a single QD, which leads to the observation of well-separated CDs (see chapter 9). The transport gap emerges as a result of the suppressed conductance in a limited gate-source voltage range, in which QDs are formed, whereas outside of this range (e.g., purple Fermi level in figure 2.4a) charge transport is not suppressed anymore. Generally, both the drain-source gap and the transport gap are larger for narrower GNRs, which results in an increased on/off ratio for narrower GNRs (see in chapters 7 and 9).

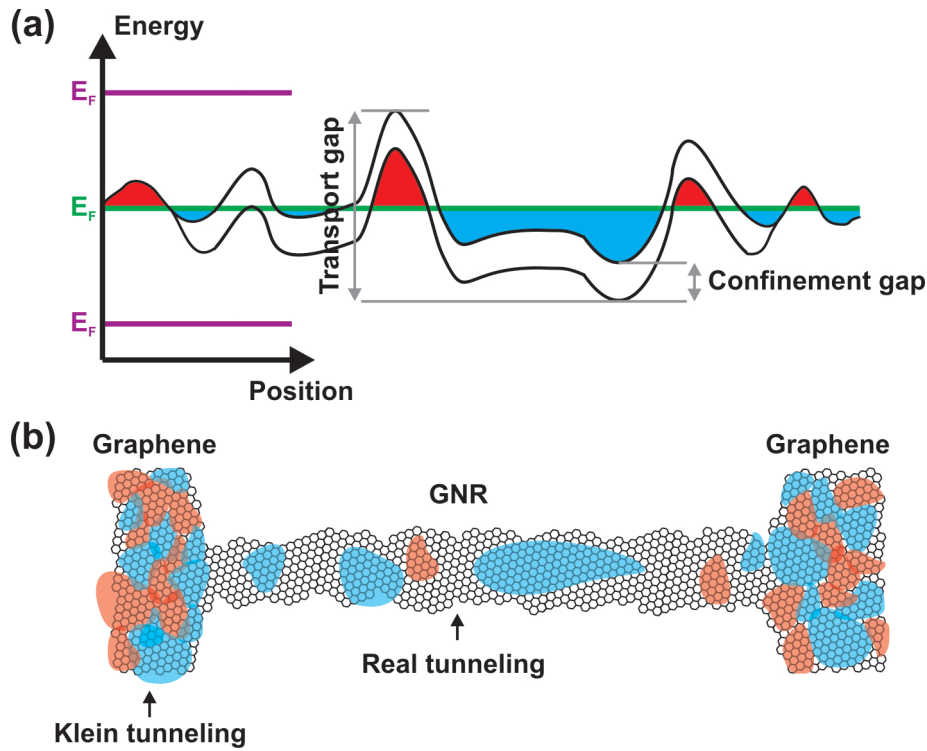


Figure 2.4.: (a) Energy landscape along a GNR when the Fermi level (green) is close to the charge neutrality point, leading to the formation of QDs. The black line corresponds to the Dirac point. In the GNR it splits into the top of the valence band and the bottom of the conduction band. (b) Geometric situation. Electron-hole puddles (blue and red regions), originating from disorder, lead to Klein tunneling in graphene, while real tunneling occurs in the GNR due to the confinement gap. Conductance is not suppressed if the Fermi level lies outside of the transport gap (purple lines in panel a). Adapted from references [84, 87].

2.3. Raman spectroscopy

Raman spectroscopy has proven to be a powerful technique not only for probing selected phonons in graphene, but also for identifying the number of layers, detecting the density of defects, determining local doping levels, studying electron-phonon coupling and thus the electronic properties themselves.[88, 89, 90, 91, 92]

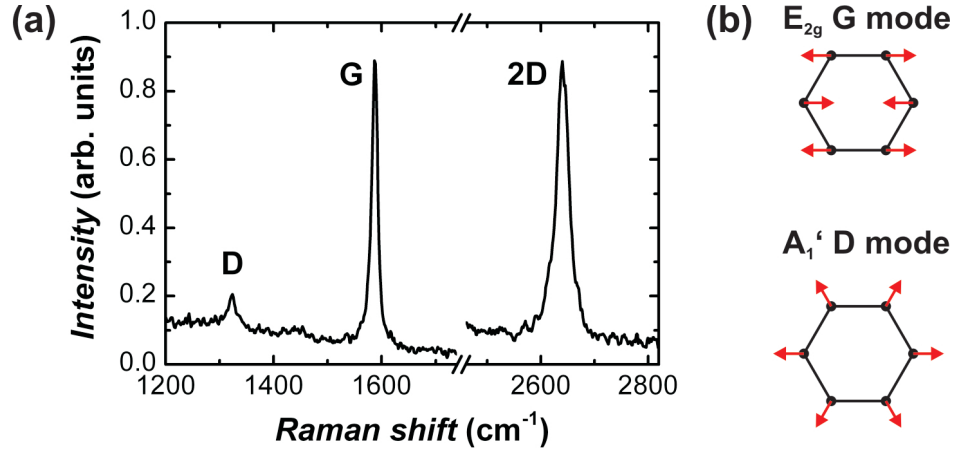


Figure 2.5.: (a) Raman spectrum of the edge of a graphene monolayer recorded with $\lambda = 633$ nm under ambient conditions. The D' signal is below the noise level. (b) Atomic displacements of the G and D mode.

The Raman spectrum of graphene is characterized by four major peaks, namely the D, G, D', and 2D peak (figure 2.5a). The G peak position (~ 1580 cm⁻¹) is independent of the excitation wavelength. It corresponds to the doubly degenerate optical phonon of E_{2g} symmetry (in-plane transverse optic plus longitudinal optic mode) at the Brillouin zone center Γ (see red circle in figure 2.6).[88, 93] The E_{2g} phonon involves in-plane bond stretching of all pairs of carbon atoms (see figure 2.5b). The Raman G peak measurement is a three step process in graphene (figure 2.7a): (i) photon absorption leads to the excitation of an electron/hole pair, (ii) relaxation of the electron (or the hole) via emission of a G phonon, and (iii) electron/hole recombination emits a red-shifted photon. As the electron is excited to a real state (the conduction band) rather than a virtual state, one speaks of a resonant Raman process.

The D peak (A_1' symmetry) is a ring-breathing mode (in-plane transverse optic phonon, see figure 2.5b), which originates from the Brillouin zone border ($\mathbf{K} < \mathbf{q} < \mathbf{M}$). In order to be Raman active, a defect is required (e.g., the edges of graphene) to reach a total momentum of approximately zero, as required for Raman scattering.[93, 96] Reference [97] identified double resonance (DR), as the scattering

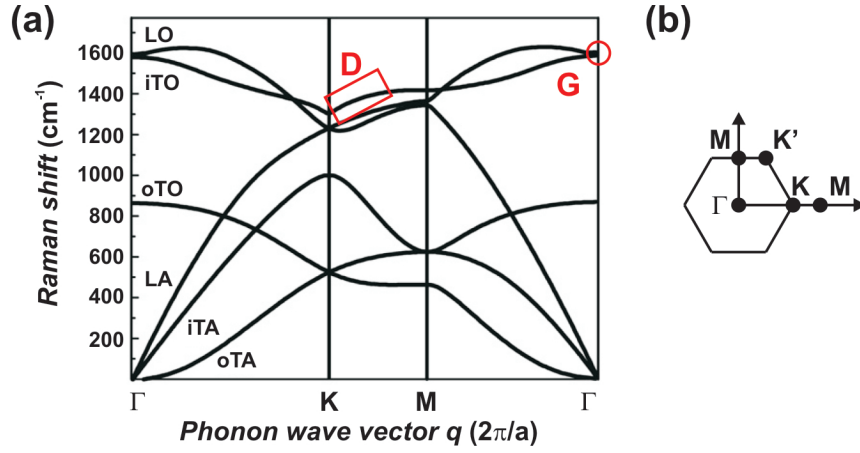


Figure 2.6.: (a) Calculated phonon dispersion relation of graphene (a is the graphene lattice spacing of 2.46 \AA). Adapted from references [94] and [95]. (b) The reciprocal space unit cell showing the Brillouin zone with its high symmetry points.

mechanism. DR Raman scattering is a four step process (figure 2.7b), comprising (i) photon absorption, (ii) elastic defect scattering, (iii) inelastic electron-phonon scattering, and (iv) electron/hole recombination plus photon emission. The DR condition is reached when the energy is conserved in all these steps. Thus DR links the phonon wave vector to the electronic band structure. Accordingly, the D peak position varies with excitation energy ($\sim 1320 \text{ cm}^{-1}$ for 633 nm , $\sim 1350 \text{ cm}^{-1}$ for 488 nm). For higher excitation energies a larger momentum transfer is needed. Due to the dispersion relation of the iTO phonon, a D phonon with larger momentum has a higher energy (see red box in figure 2.6), resulting in a larger redshift for higher excitation energies.

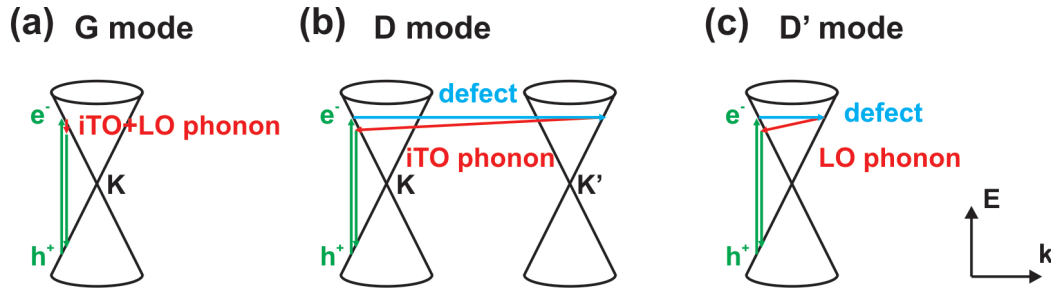


Figure 2.7.: Raman scattering process for (a) the G peak (in-plane transverse optic plus longitudinal optic mode). (b) One-phonon double resonance process for the D peak (intervalley scattering) and (c) the D' peak (intravalley scattering). Adapted from references [91, 94].

The 2D line is the second order of the D peak, and involves two iTO phonons of opposite momentum. Hence, it is always observed even in the absence of defects, and its frequency is twice the one of the D peak (2640 to 2700 cm^{-1} for 633 to 488 nm). The position and shape of the 2D peak, as well as the ratio of intensity between the G peak and 2D peak, are used to discriminate single- from multi-layered graphene. A similar process to the one shown in figure 2.7b is intravalley scattering, as schematically depicted in figure 2.7c. Again, a defect activates scattering of longitudinal optic phonons with a small wavevector, resulting in the so-called D' peak. It occurs around 1620 cm^{-1} in defective graphene.[98]

2.4. Surface enhanced Raman spectroscopy

In the present work, surface-enhanced Raman spectroscopy (SERS) is applied to graphene and GNRs (see chapter 5).[99] Metal substrates (Au, Ag, and Cu), either with rough (nanostructured) surfaces or in the form of nanoparticles (NPs), are used as typical SERS substrates, which can provide enhancement factors by up to 10^{15} for visible light. Two different SERS mechanisms, namely electromagnetic and chemical, are widely accepted to contribute to the enhancement.[100, 101]

The electromagnetic mechanism is relevant on rough metal surfaces with feature sizes smaller than the excitation wavelength. Incoming light can launch a surface plasmon resonance (SPR) in these metal structures, which is a collective oscillation of valence electrons against the positive nuclei in the metal (see figure 2.8a). The resonance frequency, at which the SPR absorbs and scatters light most efficiently, depends on the type of metal and the geometry of the nanostructure. The SPR results in a strong electromagnetic near-field. When the analyte is in close vicinity to the metal structure, its Raman scattering is intensively enhanced. The total Raman enhancement is the product of the enhancement factor for the incoming photons $f(w_0)$ and the enhancement factor for the Raman scattered photons $f(w_0 - w_{vib})$: $I \sim |f(w_0)|^2 |f(w_0 - w_{vib})|^2 \sim |E|^4$. The surface-enhanced Raman intensity approximately scales with the fourth power of the electromagnetic field. Even higher enhancement factors can be achieved through interacting surface plasmons of different metal nanostructures at so-called "hot spots".

For chemical enhancement, the analyte has to bind to the metal, in order to enable electron transfer from/to the metal, creating new electronic states in this charge transfer (CT) complex. These new states are believed to be resonant intermediates in the Raman scattering, which leads to a Raman enhancement (see figure 2.8b).

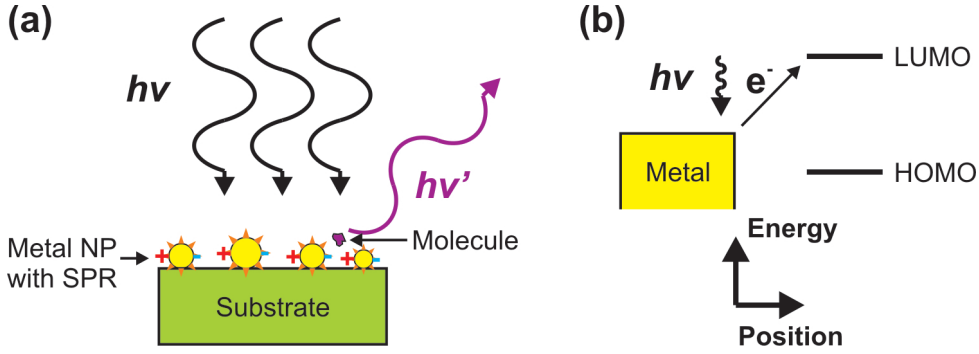


Figure 2.8.: (a) The incoming light excites surface plasmons on a nanostructured metal surface. A close-by molecule experiences more light and hence Raman scattering, since it is in the enhanced near-field region. (b) Scheme of the photoinduced metal-molecule charge transfer.

CT requires energy matching between the molecule's energy levels, the metal Fermi level and the photon energy.

2.5. Optoelectronic properties

Graphene possesses broad-band absorption in the visible range.[102] Only $\pi\alpha \sim 2.3\%$ of the incoming light is absorbed, where $\alpha = \frac{e^2}{4\pi\epsilon_0\hbar c} = \frac{1}{137}$ is the fine-structure constant. Two models, based upon built-in electric fields or the photo-thermoelectric Seebeck effect, are discussed in the literature for the conversion of light to electric energy in graphene.

In case of the built-in electric field mechanism, photon absorption leads to an excitation of electrons from the valence to the conduction band. The electron and its hole get separated in an internal electric field, thus producing an electric current.[103] The internal built-in electric field is formed near the metal electrode-graphene interface (see figure 2.9a).[104] Its magnitude depends on the difference in the work functions of the metal electrode and the graphene channel, which is given by:

$$\Delta V = \Phi_{Metal} - \Phi_G - \Delta E_F + \text{sgn}(V_{GS} - V_{Dirac}) \cdot \hbar v_F \cdot \sqrt{\pi\alpha} \cdot \sqrt{|V_{GS} - V_{Dirac}|},$$

with Φ_{Metal} the metal and Φ_G the graphene work function. ΔE_F is due to electron transfer and is responsible for the formation of an interface dipole layer. The last term accounts for the effect of the gate-source voltage V_{GS} on the Fermi level, and hence on the work function in graphene (α is determined by the gate insulator).

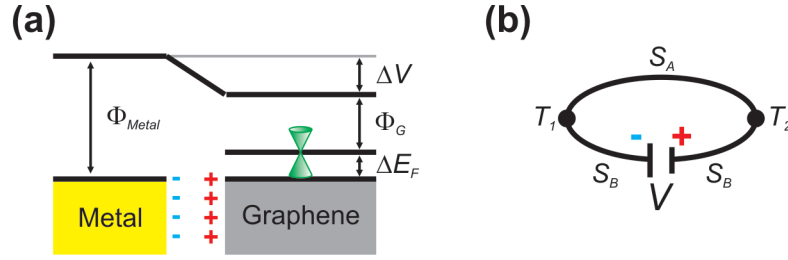


Figure 2.9.: (a) Schematic illustration of the energy level alignment associated with the built-in electric field at the graphene-metal interface. (b) Two materials with different Seebeck coefficients meet at two points of different temperature, resulting in the production of a voltage.

In the photo-thermoelectric Seebeck effect, photon energy is converted into heat and then into an electric voltage. Generally, the Seebeck effect relies upon the existence of a temperature difference $\Delta T = T_2 - T_1$ between two contacts between two materials (A, B) with different Seebeck coefficients (S_A, S_B) (see figure 2.9b). This produces a thermoelectric voltage $V = \int_{T_1}^{T_2} (S_B - S_A) \cdot dT$, which can be simplified to $V = (S_B - S_A) \cdot \Delta T$, if the Seebeck coefficients are largely independent of temperature. For a degenerate electron system like graphene the Mott relation holds and can be used for calculating the Seebeck coefficient:

$$S = -\frac{\pi^2 k_B^2 T}{3e} \cdot \frac{1}{\sigma} \cdot \frac{d\sigma}{dV_{GS}} \cdot \frac{dV_{GS}}{dE},$$

where k_B is the Boltzmann constant and σ the conductivity.[105, 106, 107]

3. Experimental techniques

Nanoscale characterization tools have become increasingly important. In this chapter the techniques used in this thesis are briefly introduced. Samples have been studied by atomic force (AFM) and scanning tunneling microscopy (STM), scanning electron (SEM) and transmission electron microscopy (TEM), confocal Raman spectroscopy, as well as scanning photocurrent microscopy (SPCM).

3.1. Atomic force microscopy

AFM is a scanning probe microscopy technique which was used in the present thesis to image the topography of nanostructures with a resolution in the nanometer range.[108] The basic concept of AFM is that forces (e.g. attractive and repulsive chemical forces, van der Waals forces, electrostatic forces) in the nN range act between a sample and a sharp tip. It allows imaging of both conductive and insulating samples. The AFM used is a commercial ambient condition instrument (Digital Instruments, Nanoscope IIIa), equipped with highly doped silicon tips in order to avoid charging effects (tip radius of curvature <10 nm). The instrument was used exclusively in tapping mode, wherein the cantilever is driven by a piezo actuator close to its resonance frequency (usually in the kHz range). The force between tip and sample surface is measured by the change in oscillation amplitude of the cantilever, whose bending is detected by the combination of a laser beam focused onto the cantilever backside and a position sensitive photodiode as shown in figure 3.1a. While the sample is scanned beneath the tip, a feedback loop adjusts the cantilever closer to / further away from the sample surface in order to keep the oscillation amplitude constant. The recorded information of the adjusted height values gives a topography image.

The lateral resolution depends on the tip size due to tip-sample convolution effects (see figure 3.1b). Lateral dimensions of 3D objects are always overestimated. Typically, a lateral resolution in the range of 10-30 nm and a vertical resolution of below 0.1 nm are reached under ambient conditions. The AFM images were analyzed and processed using the Nanoscope software and the WSxM software.[109]

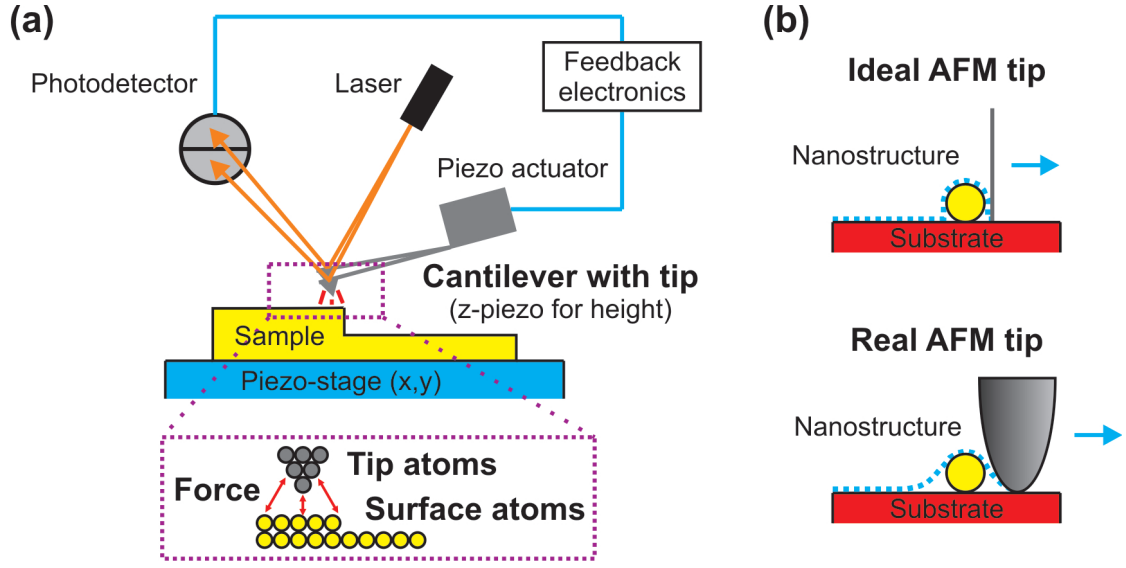


Figure 3.1.: (a) Schematic illustration of an AFM in the tapping mode. A sample is raster-scanned beneath a tip, which is attached to a cantilever. A feedback control regulates the height of the cantilever above the surface so that the cantilever amplitude, influenced by the forces between the tip and the surface, is kept constant. (b) Top: The original width of a nanostructure can only be obtained with an ideal tip. Bottom: Tip-sample interaction leads to an overestimation of the nanostructure width.

3.2. Scanning tunneling microscopy

STM is another scanning probe microscopy technique, which allows real-space atomic resolution imaging.[3] STM exploits the quantum tunnelling effect as illustrated in figure 3.2b. An electric (tunnel) current (pA-nA range) flows between a sharp metal tip and a sample, whose distance is below 1 nm, by applying a voltage V_T in the mV to V range (see figure 3.2a). One last atom sticks out at the apex, which gives the main contribution ($\sim 90\%$) to the tunnel current. The tunnel current I_T can be described by $I_T \sim e^{-\kappa \cdot d}$, where d is the tip-sample distance (figure 3.2b) and κ a constant varying for different materials. The necessity of current flow limits the use of STM to electrically conductive surfaces. The STM used in the present thesis is a commercial instrument (Omicron VT), which can be cooled down to $T = 40$ K, is operated under ultra-high vacuum (10^{-10} mbar), and is equipped with electrochemically etched tungsten tips. It was used exclusively in constant current mode. Since the tunnel current is a monotonic function of the tip-sample distance, a feedback loop, which controls the distance between the tip and the sample surface

while the tip is scanned above the sample, can be used to keep the measured current constant. Again, the recorded information of the adjusted height values yields a topography image. The STM images were analyzed and processed using the WSxM software.[109]

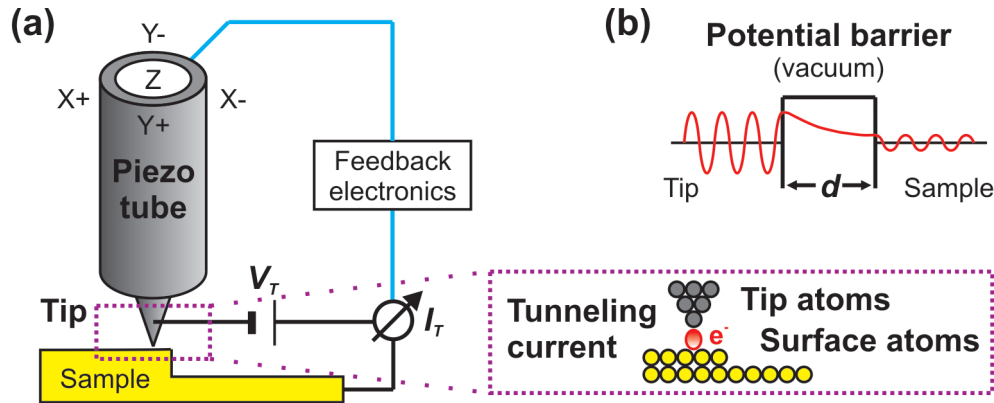


Figure 3.2.: (a) Schematic representation of a STM operated in the constant current mode. A sharp metal tip is raster-scanned with the aid of a piezoelectric tube above a sample. A feedback control regulates the height of the tip above the sample surface in order to keep the tunnel current constant. (b) Schematic representation of quantum tunnelling of an electron from the tip through a potential barrier (vacuum) of length d to the sample. The energy of the electron is the same, only the amplitude of the wave function and hence the tunneling probability of the impinging electron decreases exponentially with increasing barrier length.

3.3. Electron microscopy

SEM was used to characterize nanostructures, in particular to determine their width, since the lateral dimensions of nanostructures are generally overestimated by AFM due to tip-sample convolution effects.[110] The working principle of a SEM involves an electron source (thermal field emission) that generates an electron beam, which is focussed and deflected (raster-scanned) by a system of electromagnetic lenses over the sample surface, as schematically depicted in figure 3.3a. Samples must be (partially) electrically conductive in order to avoid charging effects. At the impact point of the primary electron beam, secondary (SE) and backscattered electrons, X-rays and light are generated. The SE, having an energy below 50 eV, are emerging directly from the topmost nanometers of the sample. On a tilted surface (e.g. at a

kink or step edge) more electrons are emitted. The SE are collected by an in-lens SE detector. The beam is scanned above the surface and the position dependent intensity of SE is used for topographic imaging. The entire SEM chamber must be under vacuum, since otherwise the electrons would be scattered by air molecules. The GEMINI in-lens SE detector of the available commercial instrument (Zeiss Ultra 55, chamber pressure in the 10^{-6} mbar range) was used in the present study. A working distance (the distance between the sample and the final lens) of 1.5-5 mm and an electron acceleration voltage of 3-15 kV were adjusted, yielding a maximum resolution of ~ 1 nm. SEM was performed after all other characterization techniques, because of the irreversible impact of the electron beam on the imaged sample.

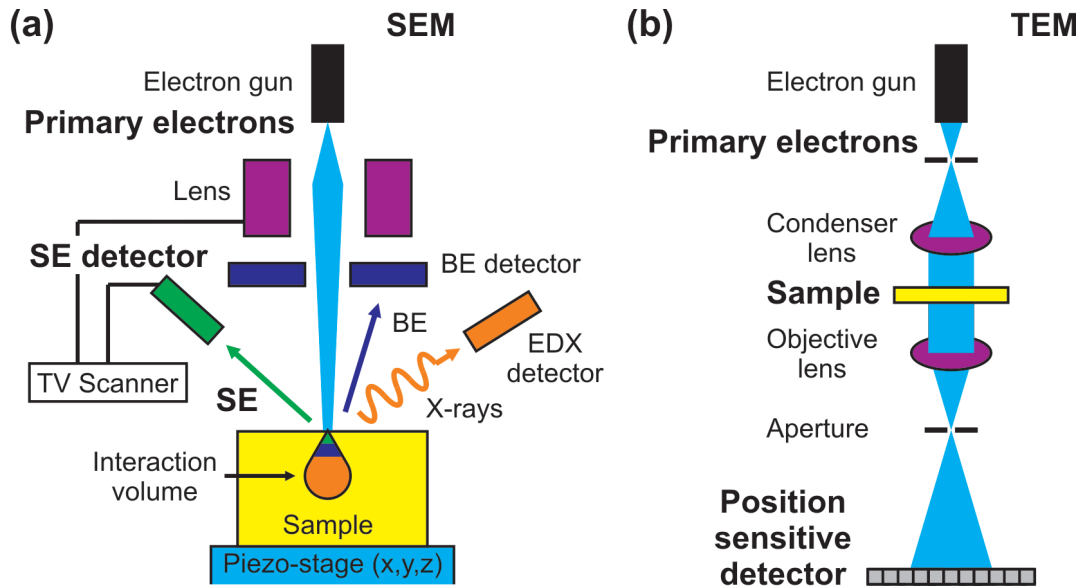


Figure 3.3.: (a) Schematic illustration of a SEM and the most often detected particles generated by the primary electrons. The secondary electrons (SE) are used for topographic imaging. (b) Schematic representation of a TEM, which uses the information of electrons, that are transmitted through a thin sample and focussed onto a position sensitive detector.

In order to reach atomic resolution of graphene a TEM was used.[3] If a sample is thin enough, electrons can be transmitted through the sample (direct and scattered). The increase in resolution of TEM compared to SEM has two origins. First a higher electron energy corresponds to a shorter de Broglie wavelength, and secondly the thin sample provides a smaller interaction volume. In a TEM, electrons from an electron source are made into a parallel beam by a (electromagnetic) condenser lens (figure 3.3b). This beam passes through the sample and is then focused by an

objective lens onto a charge coupled device (CCD) with a scintillator material that converts incident electrons to light, or directly onto an electron detector. Spherical and chromatic aberration correctors increase the resolution. The image information in high-resolution TEM relies on phase-contrast (one kind of operation mode of TEM). In phase-contrast imaging, interference of the scattered electrons leads to an image with atomic resolution. The used instrument was a high-resolution TEM (FEI Titan 80-300) equipped with a Cs-corrector. It was operated at a pressure below 10^{-7} mbar and an acceleration voltage of 80 kV in order to reduce the radiation damage of the graphene nanostructure by electron bombardment. Under the applied settings atoms appear dark.

3.4. Confocal Raman spectroscopy

A confocal Raman spectrometer was used to record Raman spectra of graphene nanostructures, in order to identify the number of layers, to detect the density of defects, and to determine the doping degree.[111] A confocal laser scanning microscope is an integral part of the confocal Raman spectrometer, and offers the advantage of a higher spatial resolution compared to a normal microscope.[112] A laser beam is focused through a pinhole to a diffraction-limited spot, as illustrated in figure 3.4a. Away from the focal plane the spatial laser intensity is therefore lower. The reflected signal is collected by the same objective and directed by a dichromatic mirror to a detector via a second pinhole, which blocks all light that is not coming from the focal plane. This two-fold light suppression allows for an increased contrast in the image. Since only one spot of the sample is in focus at a time, it is necessary to scan the sample, in order to obtain a two-dimensional image of the specimen.

In a confocal Raman setup the light emitted from the focal spot is transmitted to a spectrometer (see figure 3.4b). There, an appropriate notch filter is used to remove the much more intense Rayleigh line (unshifted laser line). The filtered light is dispersed in a monochromator (grating) and then focussed onto a CCD, which is cooled in order to decrease the dark current and hence to increase the sensitivity. Each segment of the CCD acquires a different wavelength range of the red-shifted light. A Raman spectrum is obtained by plotting the number of photons at a distinct energy (wavelength) as a function of energy.

The used confocal Raman setup is a commercial ambient condition instrument (NT-MDT, NTEGRA Spectra). It is equipped with two lasers (488 nm and 633 nm wavelength) and a 600 lines/mm monochromator grating, resulting in a wavenumber

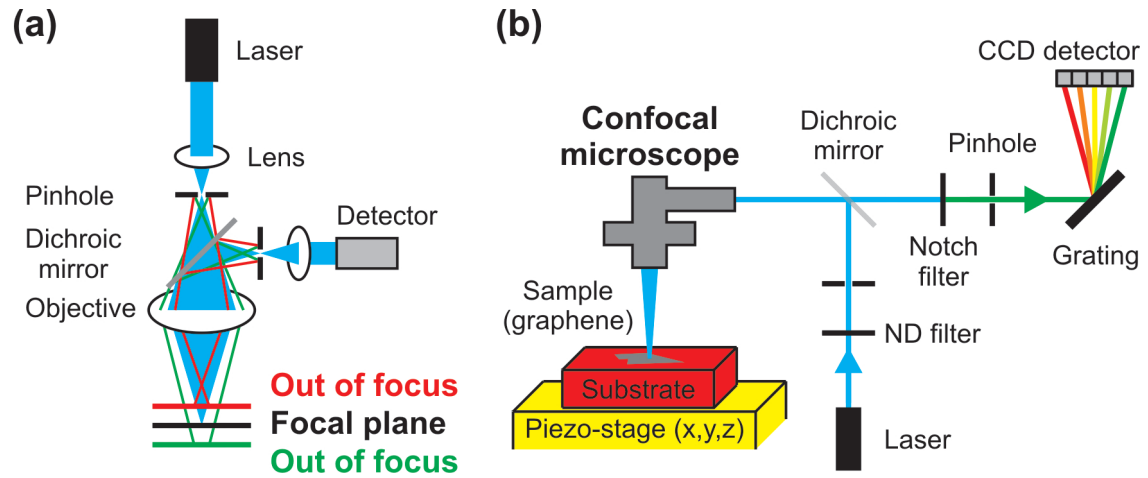


Figure 3.4.: (a) Principle of confocal microscopy. Only light emitted from the illuminated area in the focal plane is transmitted to the detector. (b) Raman spectrometer combined with a confocal microscope, using a visible laser, a neutral density (ND) filter to adjust the laser power, a notch filter to remove unshifted light, a monochromator (grating), and a CCD detector.

resolution of $\pm 1.6 \text{ cm}^{-1}$ for 633 nm and $\pm 3 \text{ cm}^{-1}$ for 488 nm. The maximum laser power is 7 mW at 488 nm and 2 mW at 633 nm, which can be decreased with the aid of a neutral density filter. The laser spot size corresponds approximately to the used laser wavelength. Raman spectra were acquired using circularly polarized light.

3.5. Scanning photocurrent microscopy

In SPCM, a sample is scanned through a laser spot, while the reflected light and generated photocurrent are recorded simultaneously, resulting in a reflection image and a photocurrent map, respectively. By overlapping both images, the photoreponse can be correlated to the structure of the investigated device. The working principle of the photocurrent part is illustrated in figure 3.5. The used instrument is a commercial ambient condition confocal microscope (Leica TCS SP2, 50x objective with NA 0.8) combined with electronic sources and meters, and a piezoelectric scanner; the setup is controlled by a home built software. The applied laser with $\lambda = 633 \text{ nm}$ (spot size \sim wavelength) has a maximum power of $240 \mu\text{W}$. The photocurrent images were analyzed and processed using the WSxM software.[109]

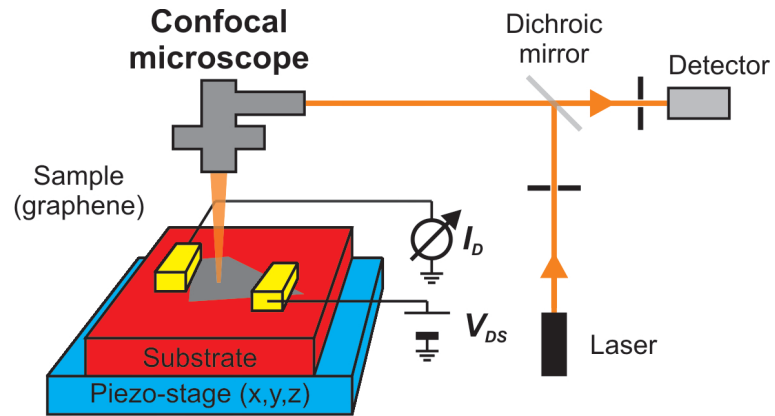


Figure 3.5.: Schematic illustration of the photocurrent setup implemented by a confocal microscope.

4. Graphene nanoribbon fabrication and structural characterization

4.1. Nanofiber/nanowire etching masks

Several fabrication approaches for graphene nanoribbons (GNRs) have been developed. One example is the bottom-up production of atomically precise GNRs of different topologies and widths, which uses surface-assisted coupling of molecular precursors.[113] However, due to their short length (<50 nm) charge transport measurements on single GNRs of this type have not yet been reported. Top-down approaches include the unzipping of multiwalled carbon nanotubes (CNTs).[114] As a disadvantage, the width and the number of graphene layers of such GNRs is undefined, and the yield of GNRs is quite low. Another top-down method is the anisotropic etching of graphene in H_2 atmosphere catalyzed by metal nanoparticles (e.g., nickel or cobalt), which yields zigzag- and armchair-edged GNRs.[115, 116]. However, this method does not provide access to well-separated GNRs of controllable width. A similar method is based on anisotropic etching of holes in graphene.[117] The etching starts from unintentional defects or prepatterned holes, and gradually transforms them into hexagonal holes with zigzag edges, which can be narrowed until two edges are very close to each other, forming a GNR in between.

Up to now, the only established fabrication method that provides electrically conductive GNRs, which are spatially separated and long enough to be contacted, is the patterning of exfoliated graphene into GNRs. To this end, electron-beam lithography (EBL) and subsequent oxygen plasma etching has been used.[65, 66, 83, 84] The advantages of this approach are the knowledge of the number of layers, and the possibility of controlling the GNR width. However, EBL limits the width to >20 nm, and yields an edge roughness of several nanometer resulting in an inactive region not participating in charge transport. Additionally, the often used hydrogen-silsesquioxane resist introduces additional scattering and doping, and cannot be easily removed.[118] Poly(methyl methacrylate) is advantageous in the latter respect, but does not allow such small device dimensions. In this thesis, the "patterning" approach was adapted by the use of V_2O_5 nanofibers (NFs) and CdSe nanowires

(NWs) as etching mask.[119, 120, 121] The smooth NFs/NWs with a regular cross-section allowed reaching a smaller GNR width. Because of their succesful use in the fabrication of metallic nanowires in the past,[119] first transport experiments were performed with V_2O_5 NFs as etching mask (see chapter 6). Due to the low electrical conductivity of the as-produced GNRs, CdSe NWs were utilized in the later stage as alternative etching mask. In the following, the characterization of the two etching masks and the details concerning the specific GNR fabrication method will be presented.

4.2. V_2O_5 nanofiber mask

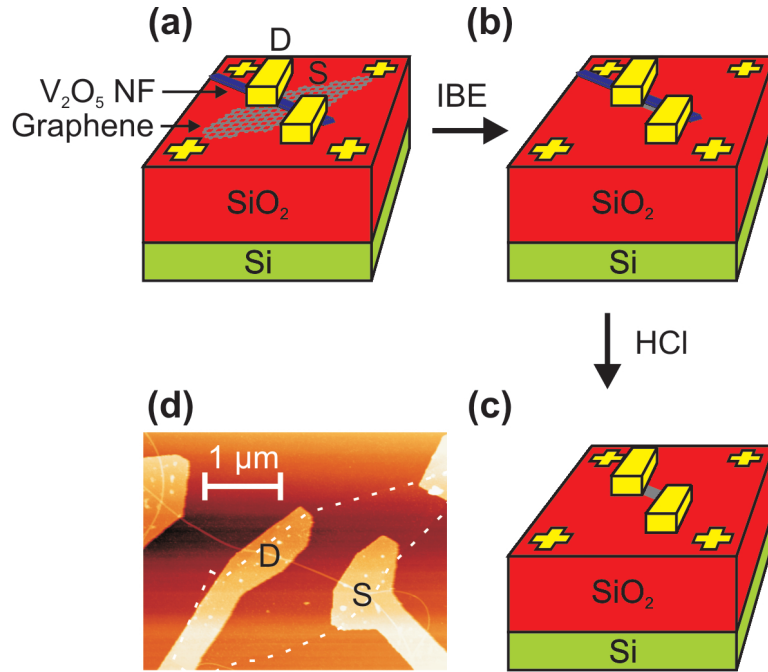


Figure 4.1.: Flowchart of the GNR device fabrication using V_2O_5 NFs. (a) Mechanical exfoliation of graphene onto a Si/SiO₂ substrate with metal markers, followed by deposition of V_2O_5 NFs and definition of metal contacts. (b) The NFs serve as an etching mask during subsequent Ar IBE. (c) Removal of V_2O_5 NFs by dilute HCl solution. (d) AFM topography image of a GNR device before Ar IBE corresponding to stage (a). The graphene sheet is highlighted by the white dashed line.

The GNR fabrication starts with the mechanical exfoliation of graphene monolayers from highly oriented pyrolytic graphite (HOPG) (Momentive Performance Mate-

materials, grade ZYA) onto highly doped Si substrates coated with a 300 nm thick thermally grown SiO_2 layer as gate dielectric by the scotch tape method.[11] Graphene monolayers were located by optical microscopy before the NF deposition, to simplify the search, otherwise disturbed by all these NFs. Prior to NF deposition, the SiO_2 surface was modified by (3-aminopropyl)-triethoxysilane to bind the NFs. Subsequently, V_2O_5 NFs obtained from a mixture of 0.2 g ammonium metavanadate and 2 g acidic ion exchange resin (DOWEX 50WX8-100) in 40 ml deionized water were deposited.[122] Graphene monolayers covered by a few NFs were located by atomic force microscopy (AFM). Subsequently, monolayers identified with the aid of confocal Raman spectroscopy were contacted by metal electrodes (see configuration in figure 4.1a and the AFM topography image in panel d).[88] To this end, optical images comprising metal markers with known position overlaid with the corresponding AFM images were imported into the EBL software. The used metal combination (1 nm Ti adhesion layer / 25 nm AuPd) ensured a smooth lif-toff during EBL. The contacted samples were briefly (3 s) exposed to an Ar ion beam (IBE) (with an accelerating voltage of 200 V, a beam current of 20 mA, and a pressure of 10^{-4} mbar) (see figure 4.1b). Finally, V_2O_5 NFs were removed by 10 % HCl for 10 min (see figure 4.1c).

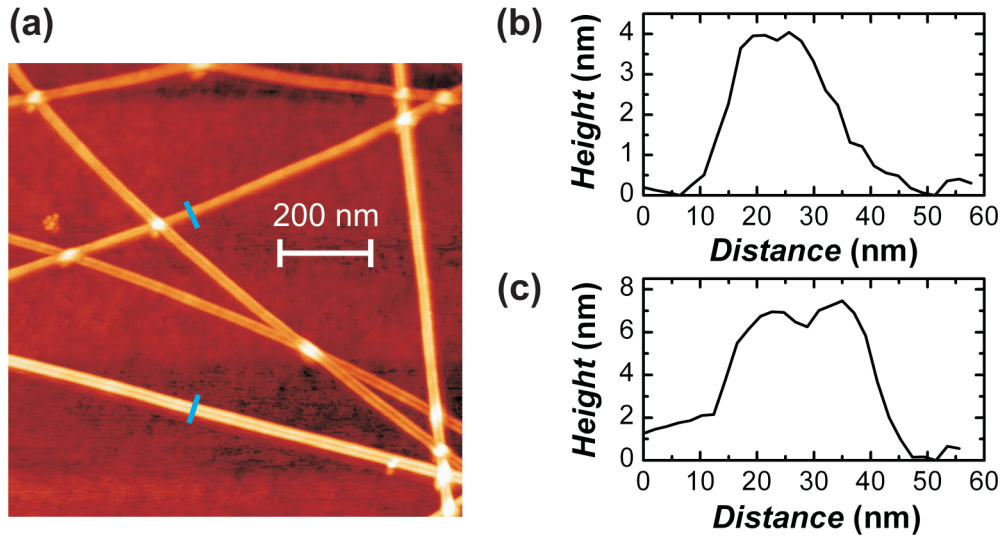


Figure 4.2.: AFM scan of representative V_2O_5 NFs. (a) AFM topography image. Height profile measurements were performed at the position of the blue bars. (b) Top bar. The height of the fiber is 4 nm. (c) Bottom bar. The fiber height is 7.4 nm.

V_2O_5 NFs were characterized both by tapping mode AFM and scanning electron microscopy (SEM). Figure 4.2 shows a representative AFM topography image

of V_2O_5 NFs. NFs with an average length of several μm and a height of 4-8 nm were obtained after ageing of the solution for several weeks under ambient conditions. AFM does not allow determining the width of the NFs, but yields only an upper limit for the width due to the tip-sample interaction. The width of the V_2O_5 NFs was determined by high-resolution SEM to be 10-20 nm (figure 4.3). AFM and SEM scans confirm that the V_2O_5 NFs have a rectangular rather than circular cross-section.[122]

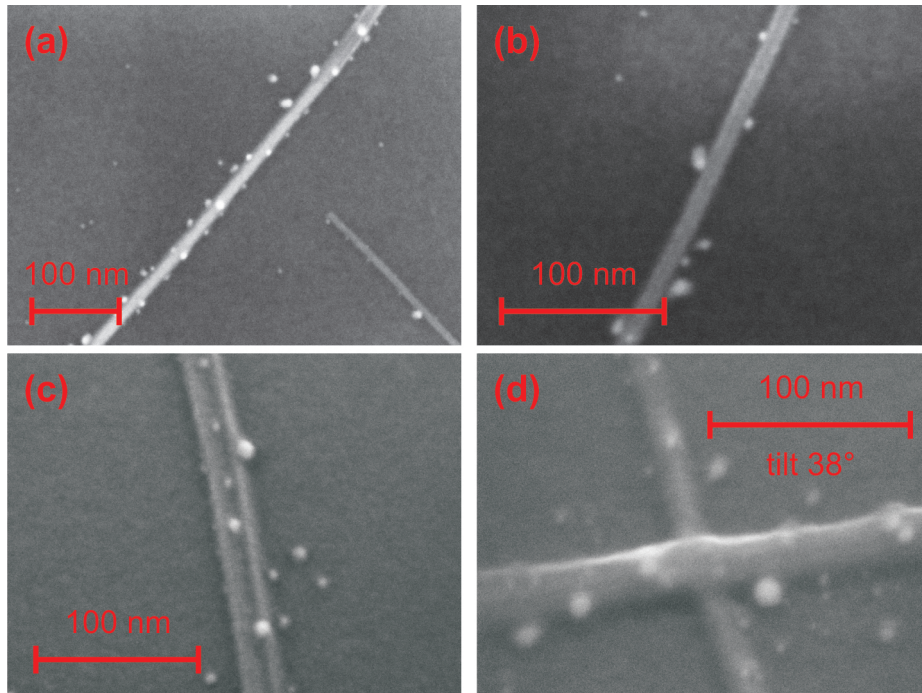


Figure 4.3.: SEM micrographs of representative V_2O_5 nanofibers. The width of the fibers are (a) 16 nm and 8 nm, (b) 12 nm, (c) 20 nm, and (d) 24 nm and 16 nm. The dots stem from the wet chemistry process used to synthesize/deposit the nanofibers, and they were not always observed (compare to figure 4.2).

AFM topography images were acquired after each GNR fabrication step in order to clarify whether there is any carbon left in the etched area which may contribute to the electrical transport of the GNR. Figure 4.4 shows AFM images of the regions of the GNRs before Ar IBE, after Ar IBE, and after removal of the V_2O_5 NFs by dilute HCl solution. Before and after IBE, there is not much difference in the step height between graphene and V_2O_5 NFs because both of them are etched during IBE. After removal of the V_2O_5 NFs, a height difference of ~ 1.2 nm is observed

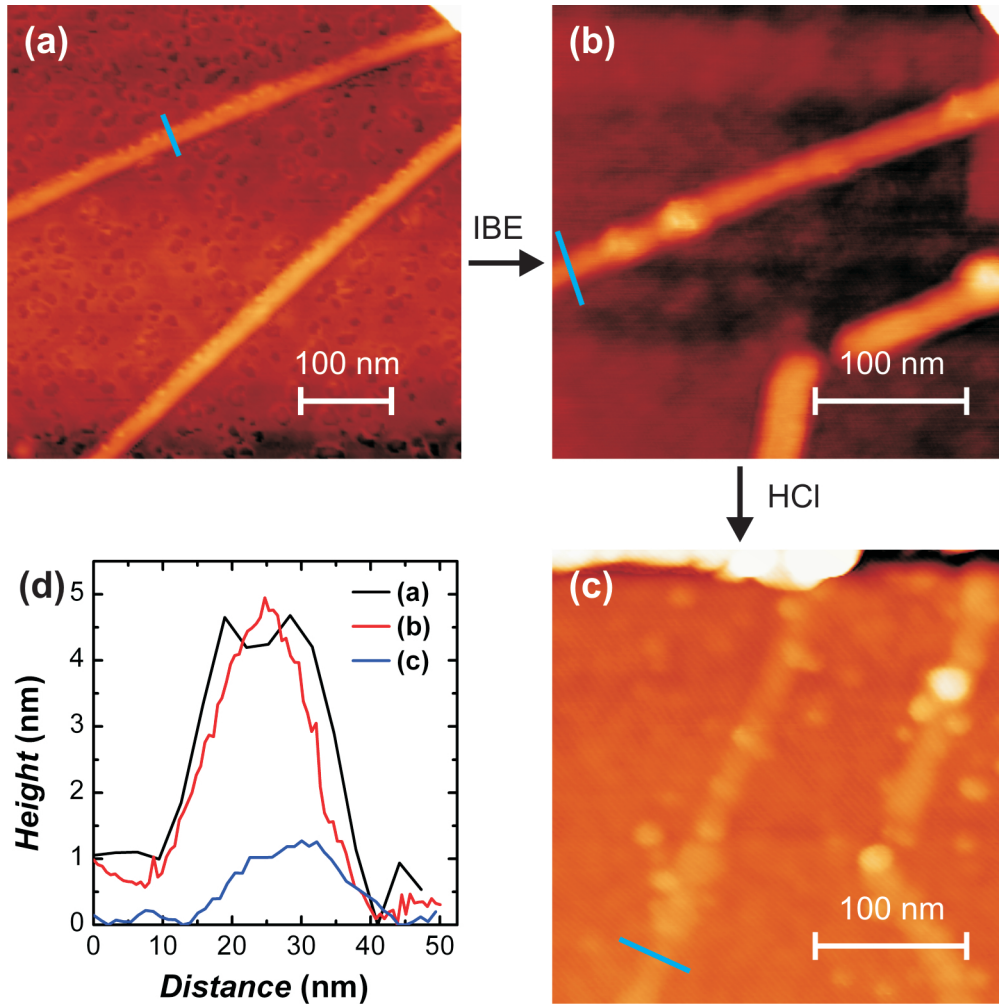


Figure 4.4.: High-resolution AFM scans of representative V_2O_5 NFs deposited on monolayer graphene, and the GNRs obtained after each fabrication step. (a) After deposition of V_2O_5 NFs. (b) After Ar IBE. (c) After removal of V_2O_5 NFs. Dots visible in this image are not carbon but stem from the HCl treatment (used to remove V_2O_5 NFs) as they are not observed before the treatment. (d) Height profiles taken along the same lines (marked by blue bars) after each fabrication step.

between GNRs and the surrounding area, which corresponds to the typical AFM thickness of graphene monolayers deposited on top of SiO_2 . This indicates that either there is no residual carbon left in the etched regions, or that if there is then it cannot be detected by high-resolution AFM and hence is unlikely to contribute to the electrical transport of the GNR devices. The faint contrast observed in some AFM phase images of the etched samples, between regions of the substrate which

were covered by graphene and those which were not, likely stems from the different surface treatments/compositions of these regions. While the unprotected regions are etched during the entire IBE process, graphene masks the underlying substrate from IBE until it is etched itself (which in the present case happens close to the end of etching). Correspondingly, a height difference (below 0.4 nm) between these regions is always observed even if graphene is fully etched away. In addition, the height profiles shown in figure 4.4d can be used to estimate the width of the GNRs. The width of the corresponding GNR does not change notably after the IBE or HCl treatment. On this basis, the width of the GNRs is estimated to be almost the same as the width of V_2O_5 NFs, namely 10-20 nm. Furthermore, the AFM scans reveal that the straight shape of the V_2O_5 NFs is not completely transferred to the GNRs, which may be due to an only partial protection of the graphene by the very thin NF mask. This assumption is supported by the fact that the Ar IBE dose had to be limited in order to keep the GNR on-resistance sufficiently low (see section 6.5).

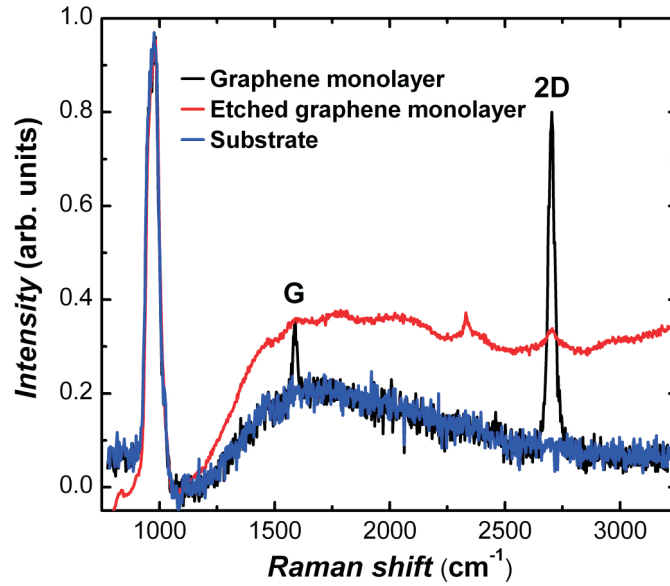


Figure 4.5.: Raman spectra acquired with $\lambda = 488$ nm from a graphene monolayer before etching (black), etched graphene monolayer (red), and the Si/SiO₂ substrate (blue). The peak in the region of ~ 1000 cm^{-1} originates from the Si substrate, and was used to normalize all three spectra.

Raman spectroscopy was also performed to characterize the graphene before and after IBE. For this purpose, a confocal Raman setup with a wavelength of 488 nm, a power of up to 2 mW, and a spot size corresponding approximately to the laser wavelength was used. Figure 4.5 shows Raman spectra recorded at a position

between source and drain electrodes of the device shown in figure 4.1d, before and after IBE. The position of the 2D peak at $\sim 2700\text{ cm}^{-1}$ and the ratio of the 2D peak height compared to the G peak height (at $\sim 1584\text{-}1587\text{ cm}^{-1}$) identify the sheet as a monolayer.[88] After etching, the graphene G peak and the 2D peak have almost completely vanished. The weak signal most probably stems from the protected graphene regions beneath the metal contacts. The D peak at $\sim 1350\text{ cm}^{-1}$, whose intensity is related to disorder in graphitic materials,[93] was not observed. In case of graphene the intensity of the D peak has been documented to increase with increasing disorder, while the G and 2D peak are still present. When the disorder increases further, the D peak starts to disappear again.[91] Hence, if there were any carbon left after IBE of the graphene monolayers, the size of sp^2 -bonded carbon islands would be less than 2 nm.[91]

4.3. CdSe nanowire mask

As described above using V_2O_5 NFs combined with ion etching for the fabrication of electrically conductive GNRs is feasible. However, the shape of the V_2O_5 NFs on the graphene monolayers is not completely transferred to the GNRs, and the V_2O_5 NFs are partially transparent for the Ar ions. Therefore, the fabrication method was modified by utilizing CdSe NWs as the etching mask in combination with reactive ion etching (RIE). CdSe NWs are thicker than the V_2O_5 NFs. The additional component of chemical oxygen etching in the RIE process helped to improve the graphene etching, allowing to keep duration and power of the etching process low. The electrical measurements in chapter 7 testify good transport properties of the GNRs obtained in this manner.

The first step of the GNR fabrication involves mechanical exfoliation of graphene on a Si/SiO₂ substrate, followed by the deposition of CdSe NWs (figure 4.7a). CdSe NWs were grown by the solution-liquid-solid method.[123] The CdSe NWs are several μm long, and their diameter (height) ranges between 10 and 35 nm (see AFM scans of representative CdSe NWs and corresponding height profiles in figure 4.6). A dispersion of CdSe NWs in chloroform was prepared by removing excess trioctylphosphine oxide (TOPO) via centrifugation (Eppendorf 5417C) for 10 min at 10,000 rpm and subsequent re-dispersion in the pure solvent, which was two times repeated. The resulting CdSe NW dispersion was drop-casted onto the graphene-coated Si/SiO₂ substrates placed on a hotplate at 50 °C. Afterwards, the substrates were rinsed with chloroform for 15 s in order to remove excess CdSe NWs and remaining TOPO. Subsequently, they were heated under argon atmosphere to 120 °C for 10 min, with the aim of improving the adhesion between the CdSe NWs and graphene. The location

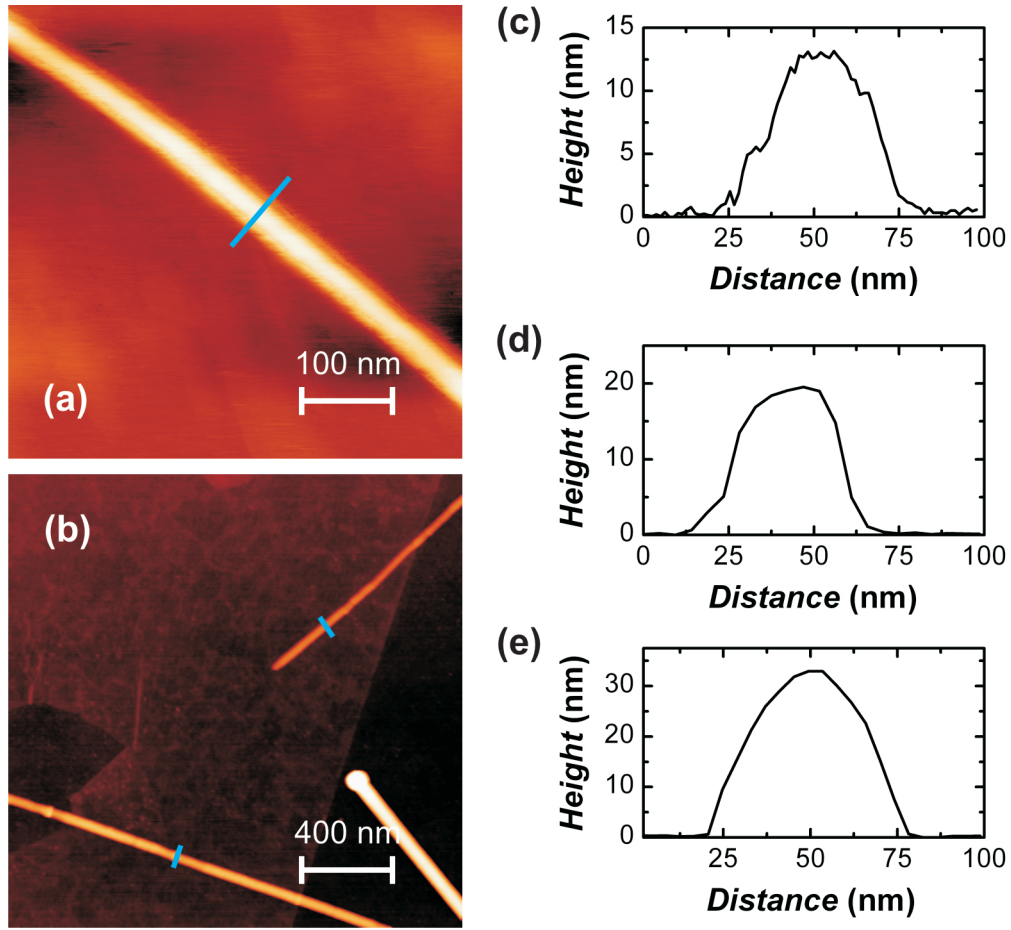


Figure 4.6.: (a), (b) AFM topography images of CdSe NWs partially covering graphene. NW heights were measured at the position of the blue bars. (c) The NW in (a) is 12.5 nm high. (d) Top bar in (b). The NW height is 20 nm. (e) Bottom bar in (b). The height of the NW is 33 nm.

and height of individual CdSe NWs was determined by AFM, while the presence of graphene monolayers was confirmed by confocal Raman microscopy. Subsequently, RIE (Leybold LE 301) was performed to etch away a few layers of graphene around individual NWs (figure 4.7b) (5 s, 100 sccm Ar, 11 sccm O₂, 0.05 mbar, 48 W). The CdSe NWs were then dissolved by dipping the substrates into a mixture of 20 ml of 30 % HCl + 1 ml of 69 % HNO₃ (aqua regia) for 3 s at room temperature, followed by rinsing with deionized (DI) water, dipping into an aqueous solution of sodium sulfide (1.2 g Na₂S + 2.5 ml H₂O) for 30 s at room temperature, and final rinsing with DI water.[124] This procedure was repeated two more times, followed by rinsing with isopropanol and blowing dry under a stream of argon. The metal markers have a layer of SiO₂ on top, protecting them from being etched by aqua

regia. Metal contacts were then defined by EBL and thermal evaporation of either 20 nm Ti + 20 nm Au or 2 nm Cr + 40 nm Pd (figure 4.7c). The exemplary AFM image in figure 4.7d testifies a regular structure and clean surface of the resulting GNRs. In contrast to the GNR fabrication method involving V_2O_5 NFs, there is no extended graphene beneath the contacts, but instead a direct transition from the metal contacts to the GNR.

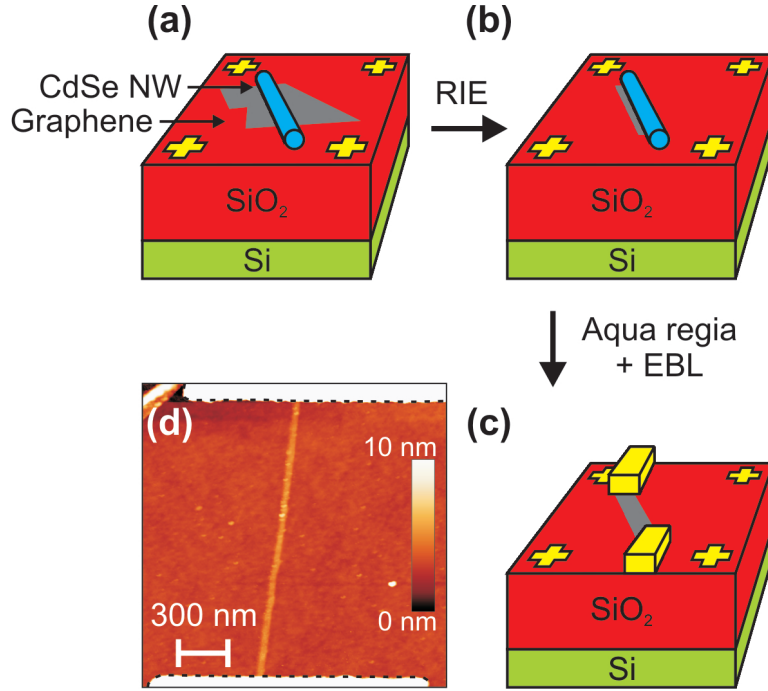


Figure 4.7.: Flowchart of the GNR device fabrication using CdSe NWs as etching mask. (a) Mechanical exfoliation of graphene onto a Si/SiO₂ substrate with markers, followed by deposition of CdSe NWs. (b) The NWs serve as etching mask during subsequent RIE. (c) After wet etching of the wires, the ribbons are provided with metal contacts. (d) AFM image of a 22 nm wide, contacted GNR. The distance between the contacts is 1.5 μm .

A scanning tunneling microscope (STM) operated at room temperature under ultra-high vacuum (10^{-10} mbar) was used to investigate the structural integrity of the GNRs after RIE. To this end, CdSe NWs were deposited on freshly cleaved HOPG. After RIE, the CdSe NWs were removed by dipping for 2 min in a mixture of 300 mg Br_2 and 20 ml methanol. Figure 4.8a shows two regions, where CdSe NWs were located. In these regions, the surface is very smooth, whereas the unprotected graphite surface is rough as a result of the RIE. The wide GNR (80 nm) is most

probably due to bundled CdSe NWs. The zoom in figure 4.8b and c reveals atomic resolution of a GNR (figure 4.8d). The Fourier transformation of the image in figure 4.8d, shown in figure 4.8e, displays the hexagonal lattice of graphite. In conclusion, the STM measurements testify the ability of the used CdSe NWs, to protect graphene during RIE.

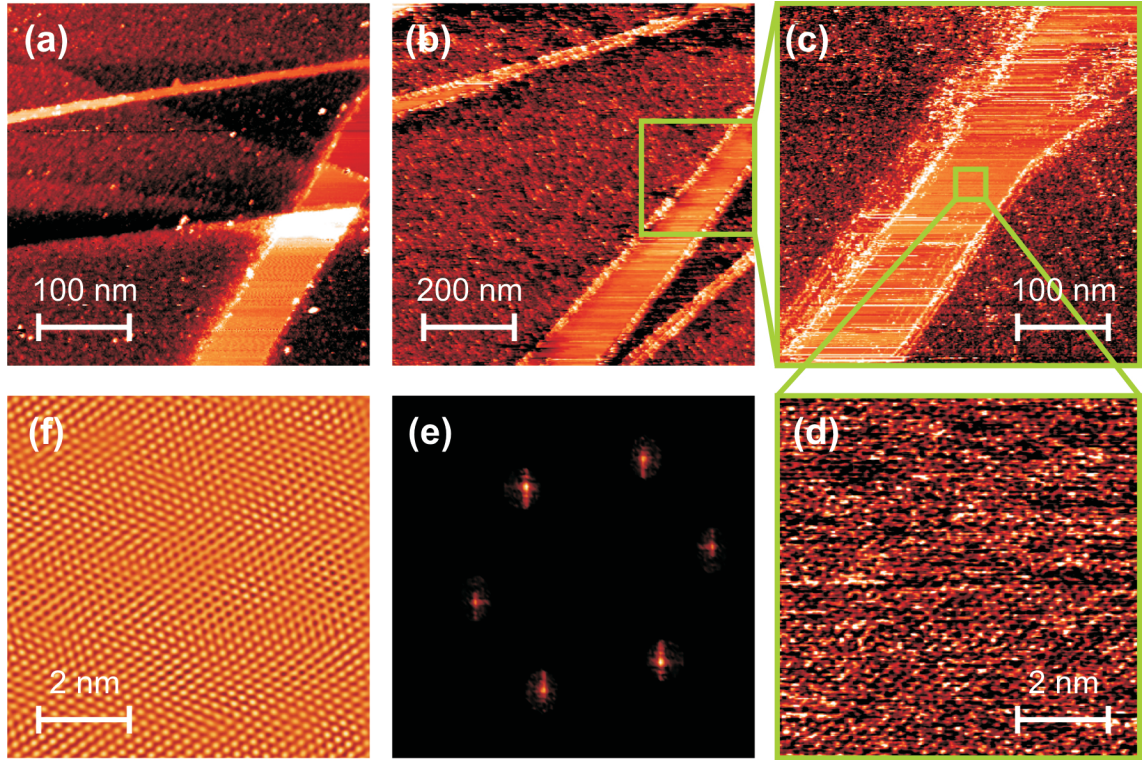


Figure 4.8.: STM images of GNRs created on HOPG recorded at room temperature under ultra-high vacuum (10^{-10} mbar). (a) Overview scan at one position. (b) Overview scan at a different position. (c) + (d) Zoom in at position (b). (e) Fourier transform of (d). (f) Fourier filtered image of (d). [Images taken by G. Rinke and S. Rauschenbach]

Figure 4.9 shows SEM images of 3 different, electrically contacted GNRs. The measured widths are 37 nm, 25 nm, and 20 nm, respectively. In an earlier fabrication step, the diameter (height) of the corresponding CdSe NWs was measured by AFM, which yielded height values of 37 nm, 26 nm, and 19 nm, respectively. This close agreement demonstrates that the width of a GNR is determined by the diameter of the corresponding CdSe NW. Measuring the width of a CdSe NW or a GNR device by AFM provides a significantly too large value due to the convolution of the imaged feature and AFM tip. Hence, we take either the SEM measured width

or, if not applicable, the AFM height of the corresponding CdSe NW etching mask as the GNR width.

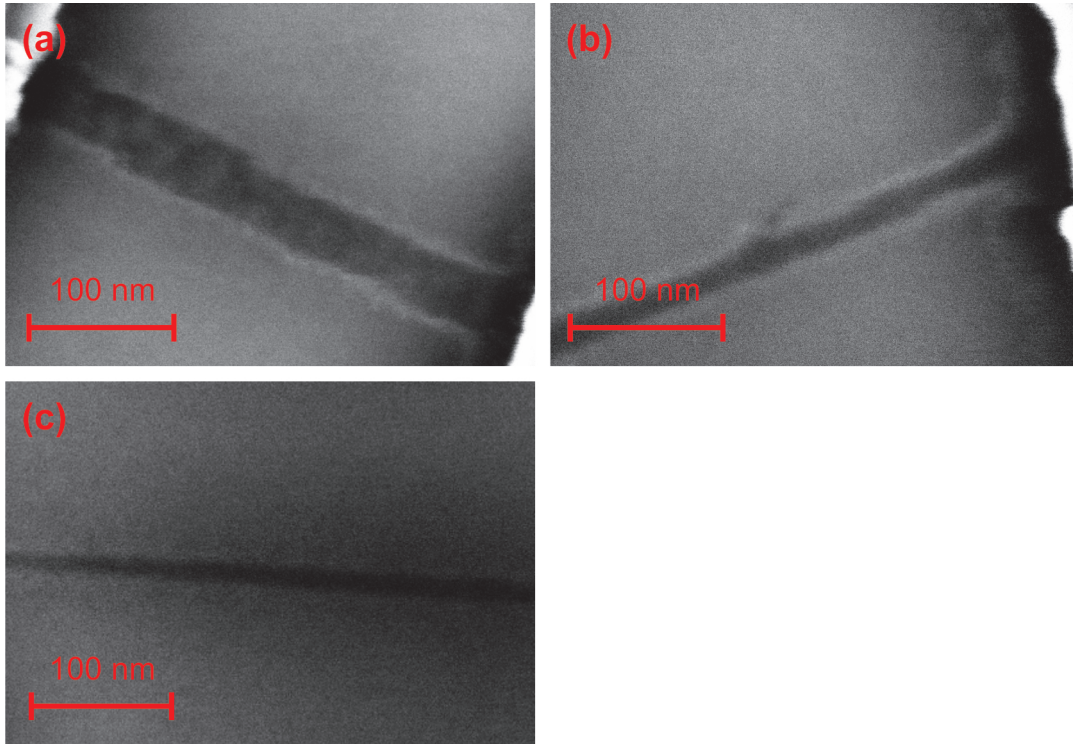


Figure 4.9.: SEM images of three representative GNRs, with a respective width of 37 nm (a), 25 nm (b), and 20 nm (c). [Images taken by P. Gehring]

5. Surface enhanced Raman spectroscopy of graphene nanoribbons

5.1. Graphene nanoribbons

Although the vibrational properties of graphene nanoribbons (GNRs) have been studied in detail by theory,[125, 126, 127] only few experimental studies on individual, narrow GNRs have been reported.[128, 129] Due to their small width, no Raman signal could be detected from the present GNRs. In references [113, 130, 131] this problem was overcome with the aid of arrays of closely spaced GNRs with equal width. Since the CdSe NWs are positioned randomly on the graphene monolayers, a different strategy had to be found. To enhance the Raman signal of single GNRs by the SERS effect (surface enhanced Raman spectroscopy), colloidal gold nanoparticles (Au NPs) were deposited on top of them. For carbon nanotubes it has been demonstrated that Au NPs can impart a sizable Raman enhancement.[132]

Toward assignment of the Raman signal to an individual GNR, the density of CdSe NWs was kept low during the fabrication process, resulting in spatially well-separated GNRs (see atomic force microscopy image in figure 5.1a). After removal of CdSe, the SiO₂ surface was modified by (3-aminopropyl)-triethoxysilane to attach Au NPs (10 μ l in 10 ml H₂O for 10 s + rinsing). Au NPs (20 nm diameter, Sigma-Aldrich) were deposited by immersing the substrate in a solution of Au NPs and H₂O for 1 h (1:5 in H₂O + rinsing). Subsequent atomic force microscope (AFM) measurements revealed a sizeable density of Au NPs in the vicinity of the GNRs (see figure 5.1b).

Raman spectra were acquired using circularly polarized light from a red laser (633 nm) or blue laser (488 nm, spotsize \sim wavelength, <7 mW) under ambient conditions. In the following, only results gained with 488 nm wavelength will be presented due to the better signal intensity. The backscattered light is dispersed in a monochromator (600 lines/mm grating, resolution ± 3 cm⁻¹ for 488 nm) and de-

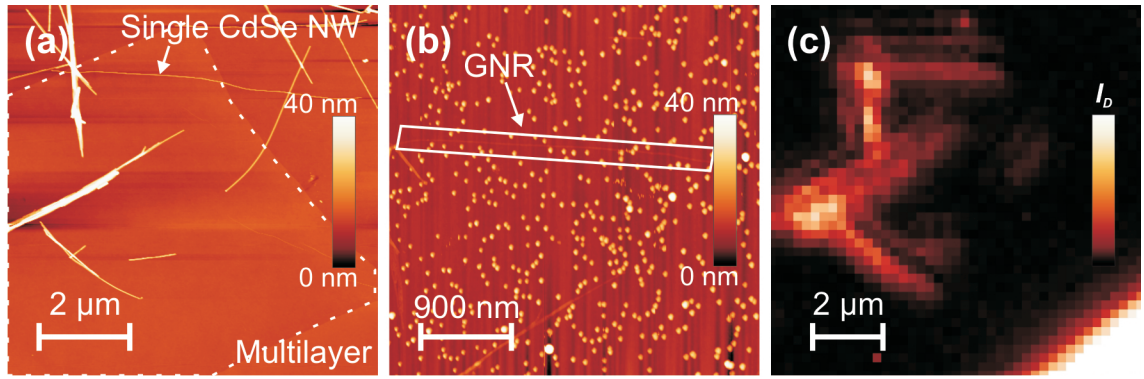


Figure 5.1.: (a) AFM image of CdSe NWs (partially bundled) on a graphene monolayer (highlighted by white dashed line). At the bottom right a multilayer is attached. (b) Same position after RIE, CdSe NW removal and Au NP deposition. (c) Raman map of the region in (a) showing the D peak signal intensity after background subtraction (488 nm, 250 nm step size, 60 s accumulation time per spectrum, <7 mW).

tected with a charge coupled device. Owing to the low light reflection by the GNRs, it is not possible to position the laser exactly on the GNR of interest. Therefore, Raman maps of the region of interest were acquired by raster-scanning (lateral step size of ~ 250 nm) the sample through the laser spot, while recording a Raman spectrum for each position. In the map shown in figure 5.1c, the Raman D peak intensity (maximum value in the range of 1330 to 1390 cm^{-1}) after background subtraction (1390 to 1410 cm^{-1}) is plotted.

Figure 5.2 shows the Raman spectrum of a ~ 21 nm wide and 2.7 μm long GNR. It displays the characteristic signatures of graphene Raman spectra, namely, the defect-induced D peak (1356 ± 3 cm^{-1}), the G peak (1589 ± 3 cm^{-1}), the 2D peak (2701 ± 3 cm^{-1}), and the defect-induced D' peak (1625 - 1628 cm^{-1}). In contrast to defect-free bulk graphene, which does not exhibit D and D' peaks, we could observe these peaks, since the edges act as defects by breaking the translational symmetry of the lattice.[88, 93, 98, 133] In contrast to reference [130], where a rather large value of 50 cm^{-1} for the full width at half maximum (FWHM) was found for the 2D peak due to averaging over several 30 nm wide GNRs, a value below 40 cm^{-1} is obtained for the present 21 nm wide individual GNR. The other peaks in figure 5.2 originate from the substrate.

Figure 5.3 shows the Raman spectrum of another, ~ 13 nm wide and 4 μm long GNR (marked by the box in figure 5.1b). Despite its smaller width, the D and 2D

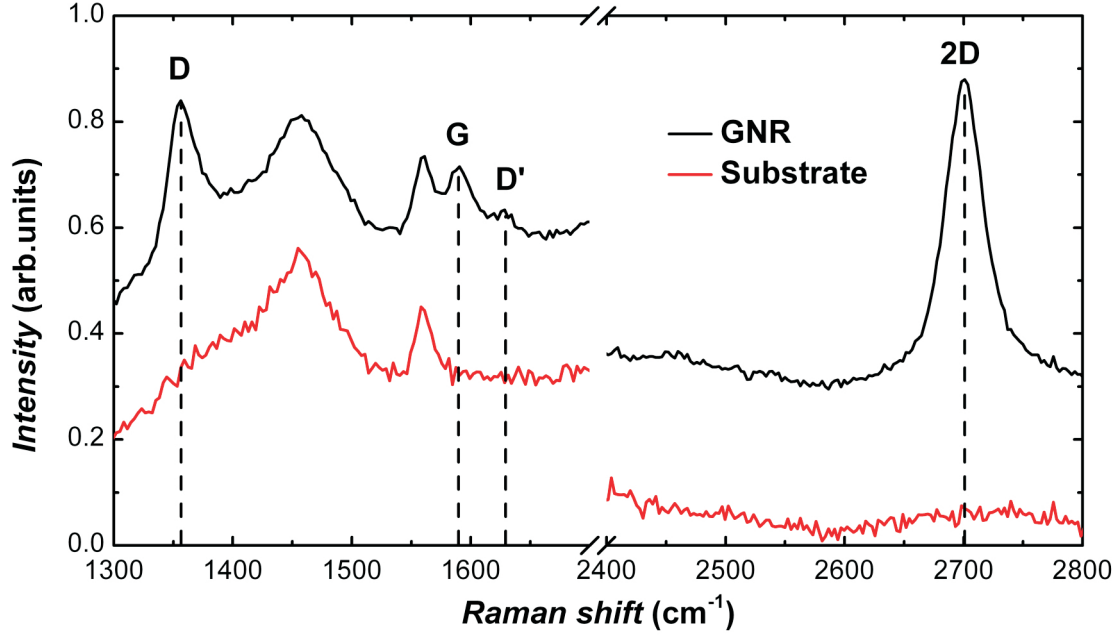


Figure 5.2.: Raman spectrum of a ~ 21 nm wide and $2.7 \mu\text{m}$ long GNR (black), recorded with 488 nm wavelength. For comparison, the spectrum of the bare Si/SiO₂ substrate is shown (red).

peaks are still observed, although the G peak is absent. The observation of the D and 2D peaks for an only ~ 13 nm wide GNR indicates the presence of a narrow inactive edge region (below 5 nm) (see section 4.1). Due to the SERS effect (different configurations of Au NPs can lead to a different enhancement factor), it is difficult to compare the absolute intensities of the graphene-related peaks of the ~ 21 nm wide GNR in figure 5.2 and the ~ 13 nm wide GNR in figure 5.3. Nonetheless, the ratio of the 2D and D peak intensities of the different GNRs can be compared. The D peak intensity depends only on the edge-region of the GNR, whereas the 2D signal stems from the bulk. For the narrower GNR the I_{2D}/I_D -ratio is decreased by a factor of three. Since the ratio between the bulk area and the edge region is smaller for a narrower GNR, this explains the observed behavior.

However, neither a breathing-like mode (BLM) in the low wavenumber region (below 400 cm^{-1}), nor a splitting of the G band, nor any other novel feature could be found in the Raman spectra of the GNRs.[113, 129] Nonetheless, the Raman measurements attest the present GNRs a good structural quality.

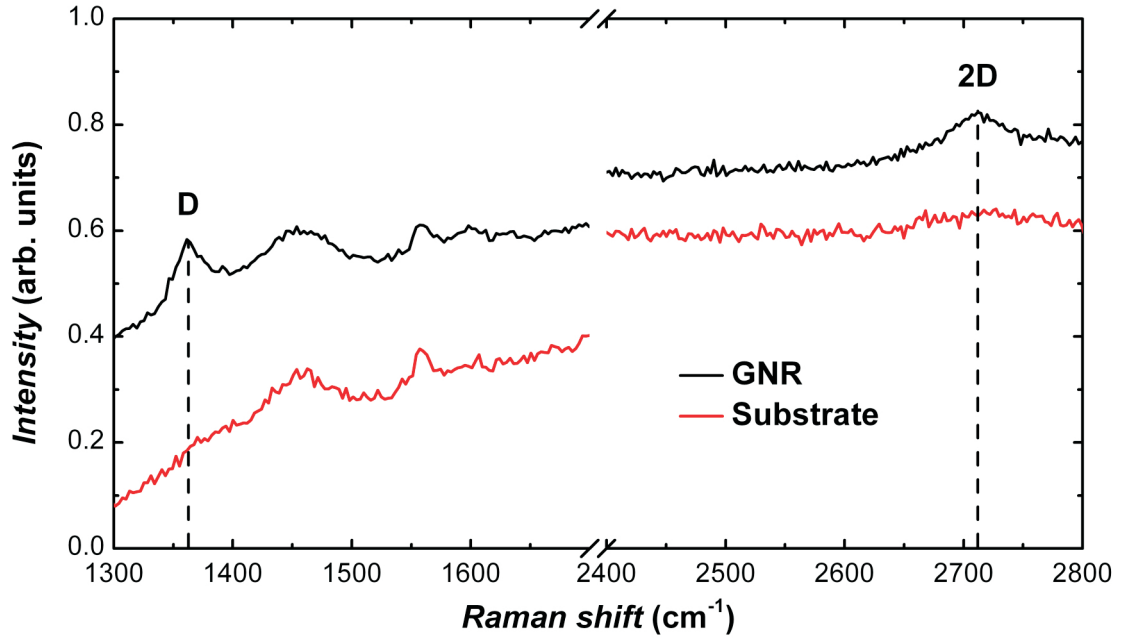


Figure 5.3.: Raman spectrum of a ~ 13 nm wide and $4 \mu\text{m}$ long GNR (black), recorded with the blue laser ($\lambda = 488$ nm). For comparison the spectrum of the bare substrate is displayed (red).

5.2. Mechanism of surface enhancement

As explained in section 2.4, two mechanisms are attributed to the Raman enhancement, namely the electromagnetic mechanism (EM) and the chemical (charge transfer) mechanism (CM). In order to gain a better understanding of the enhancement of graphene's Raman bands, the influence of the excitation wavelength, the kind of metal, the NP size, their shape and the inter-particle distance has been studied previously.[134, 135] In references [134, 135] the Raman enhancement was mainly attributed to the EM, whereas in reference [136] a notable contribution of the CM was found. So far, the possibility to vary the Fermi level in graphene was only used to study the Raman enhancement of molecules deposited on graphene, where the graphene imparted a chemical enhancement of the molecule's Raman signal.[137] In this thesis, the variation of the Fermi level in graphene was exploited to investigate the enhancement of graphene Raman bands by metal NPs. A possible signature of the CM could be an asymmetry between the Raman peak intensities in the electron and hole regime, since the resonance condition (see section 2.4) is expected to depend on the Fermi level difference between graphene and the metal NPs.

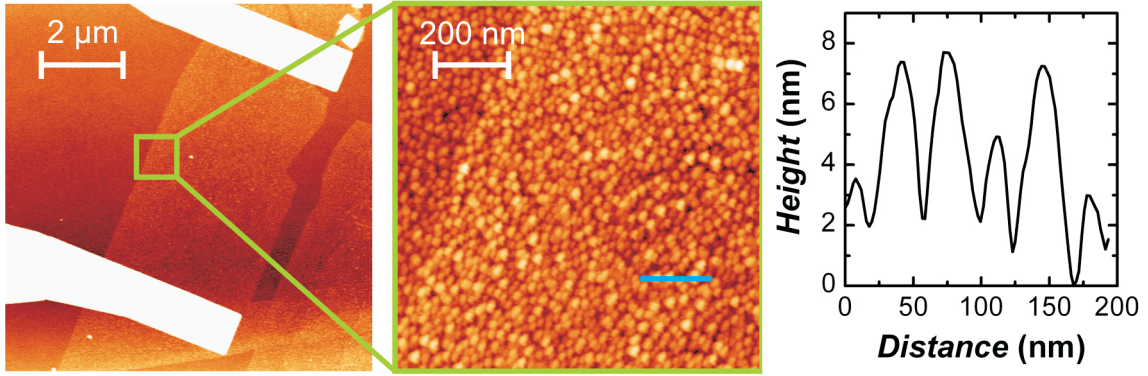


Figure 5.4.: Left: AFM image of a contacted graphene sheet with Ag NPs on top. Center: Zoom of the left edge of the graphene sheet. Right: Height profile along the blue line in the center panel.

Densely arranged silver nanoparticles (Ag NPs) were created on graphene by thermal evaporation of 1 nm Ag. The NPs form due to surface diffusion.[135] Figure 5.4 shows AFM topography images of a thus obtained graphene device covered by Ag NPs with a height of up to 8 nm.

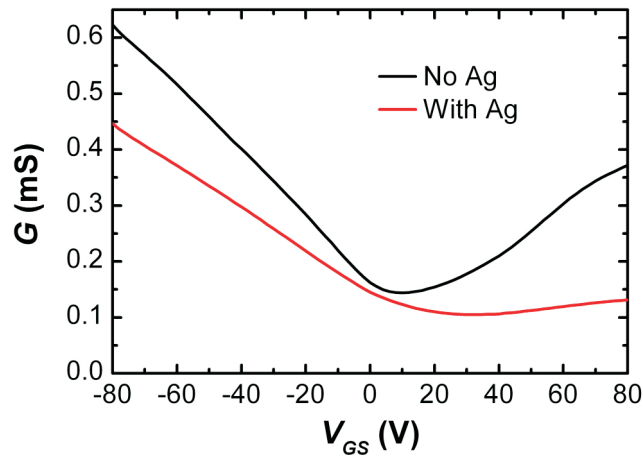


Figure 5.5.: Transfer curves (conductance G vs. gate-source voltage V_{GS}) of pristine graphene (black) and the Ag NP-decorated graphene presented in figure 5.4 (red), recorded under ambient conditions.

The graphene devices contacted by 5 nm Ti and 30 nm AuPd electrodes in conventional field-effect transistor (FET) configuration were electrically characterized using the doped silicon substrate as a back gate. Figure 5.5 shows the transfer curves (conductance G vs. gate-source voltage V_{GS}) of pristine graphene and the

Ag NP-decorated graphene (see figure 5.4). The Dirac point for the pristine device is at $V_{GS} = +10$ V, while the Dirac point for the Ag NP-decorated graphene device has increased to $V_{GS} = +32$ V. A p-doping of graphene by Ag NPs was observed for all devices. The nominal thickness of the evaporated silver film had to be limited to 1 nm, in order to keep the charge neutrality point of graphene below $V_{GS} = +80$ V, and hence to enable Raman measurements for both types of charge carriers. Higher gate-source voltages can destroy the SiO_2 gate insulator. Additionally, the Ag NPs increased the electron-hole asymmetry.[138] In reference [62] it was found, that doping of graphene by molecules suppresses conductance via carriers of the opposite polarity of the dopant. This can be explained by a misalignment of the charge neutrality points of the graphene below the electrodes and the graphene channel. As a consequence, asymmetric injection of carriers occurs from the former region into the corresponding electron and hole states of the channel.

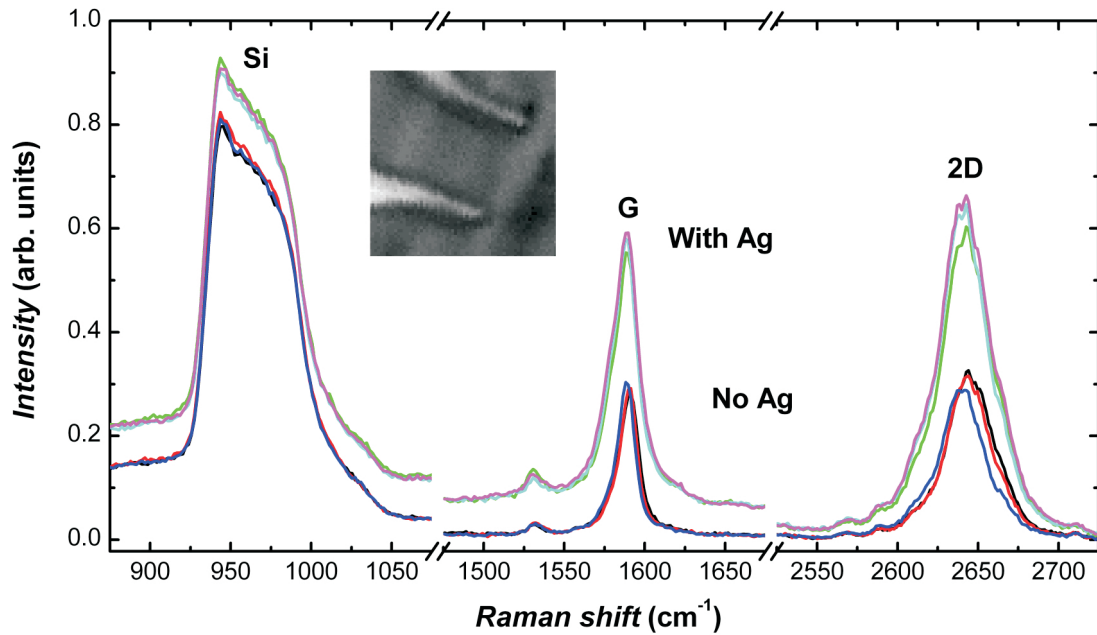


Figure 5.6.: Raman spectra of three pristine graphene devices (lower curves) and three devices with Ag NPs on top (upper curves), recorded under ambient conditions. All Raman spectra are normalized to the Si peak around 960 cm^{-1} . Insert: Reflection image of a graphene device, which was used to position the laser spot at the measurement position.

Raman spectra ($\lambda = 633\text{ nm}$, spotsize \sim wavelength, 600 lines/mm grating, $\pm 1.6\text{ cm}^{-1}$ resolution for 633 nm) acquired under ambient conditions at the center region of large graphene devices without and with Ag NPs are presented in fig-

ure 5.6. The laser intensity was limited to below 0.2 mW in order to avoid changes in the morphology of the Ag NP films. A good signal-to-noise ratio was obtained by collecting each spectrum for 30 s. All spectra are normalized to the Si peak around 960 cm^{-1} . An optical reflection image helps to position the laser spot at the desired position on a sheet. In the center of the graphene sheets, far away from the edges, the intensity of the Raman signals is spatially homogeneous. The G peak ($\sim 1590\text{ cm}^{-1}$) intensity and the 2D peak ($\sim 2640\text{ cm}^{-1}$) intensity of the graphene devices with Ag NPs are enhanced by a factor of 2 compared to the pristine devices. In reference [135] a larger enhancement factor was attained by depositing more Ag, which was not possible in this study as explained before. Measurements with $\lambda = 488\text{ nm}$ yielded an enhancement factor of 1.5. Following measurements were only performed with 633 nm wavelength due to the higher enhancement factor and, because due to the lower photon energy of the 633 nm light, the resonance condition described in section 2.4 should be easier to fulfill.

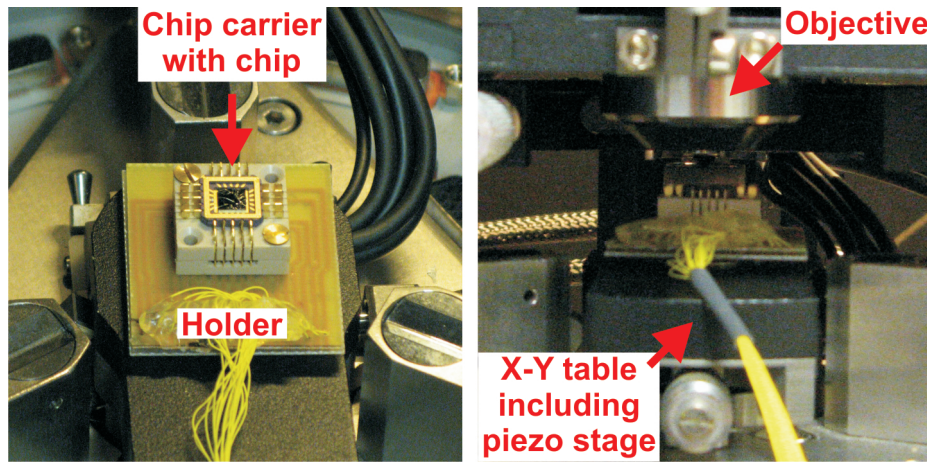


Figure 5.7.: Chip carrier holder, which is thin enough to be mounted on the piezo stage of the Raman setup.

A holder was constructed, which is thin enough to allow placing of bonded graphene devices in the Raman setup and moving of the examined graphene sheet into the focus of the laser spot (see figure 5.7). This allowed to measure electrical transport and Raman properties simultaneously. By fitting the G peak and 2D peak in the obtained spectra, by a Lorentzian, the peak position, the full width at half maximum (FWHM) and the peak height were determined.[139] However, only the electron regime could be fully probed in pristine graphene devices, similar to the measurements in reference [90]. It is not possible with the present setup to measure in vacuum and at low temperatures, which would provide access to the hole regime

for a back-gated device.[140] Therefore, a solid polymer electrolyte layer (LiClO_4 + polyethylene oxide) in combination with a silver wire was used as a topgate, similar to the procedure reported in references [139, 141]. No difference in the carrier density of Ag NP-covered graphene regions compared to uncovered regions is expected, as it was shown in reference [141] that the topgate action extends below the metal contacts up to $2\text{ }\mu\text{m}$ away from the contact edge.

Figure 5.8a shows the transfer curve of the pristine graphene device in figure 5.5, recorded with the topgate. The topgate voltage range had to be limited to $\pm 0.5\text{ V}$ to avoid irreversible changes of the device conductance, in particular electrochemical reactions that would generate a considerable topgate current. Figure 5.8b and c show the V_{TG} dependence of the position and FWHM of the G peak. The stiffening of the G peak is due to energy renormalization of the G phonon frequency upon doping.[90, 140] The decrease in linewidth can be explained by Pauli blocking of the decay channel of G phonons into electron-hole pairs, when the Fermi level is shifted away from the Dirac point by a value larger than half of the phonon energy.[90, 140] The non-linear dependence of the 2D peak position is in accordance with predictions by density functional theory.[139] For the observed I_{2D}/I_G ratio decrease with increasing doping,[139] no explanation has been established yet. Overall, the results presented in figure 5.8a-e reproduce well the findings reported in the literature. As explained above, the intensity of the graphene Raman peaks might reveal a contribution of the CM in Ag NP-decorated devices. For reference, the G peak intensity of the pristine graphene device is plotted in figure 5.8f, showing a symmetrical behavior similar to the I_{2D}/I_G ratio.

Figure 5.9 displays the same kind of measurements for the graphene device covered with Ag NPs (see figure 5.4). Like in figure 5.5, there appears a pronounced electron-hole asymmetry in the conductance (panel a). An asymmetry between the hole and the electron regime occurs in the Raman characteristics as well (panel b-f). At first sight, the different G peak intensity in the electron and hole doping regimes may be interpreted as a signature of the CM. However, considering the pronounced electron-hole asymmetry in (a) the conductance, (b) the position of the G band, and (c) the FWHM of the G band, it is more reasonable to assume that the electron-hole asymmetry in the G peak intensity has the same origin as the one in the transport, rather than to result from chemical enhancement. This assertion is supported by the fact that some pristine graphene devices showed a more pronounced electron-hole asymmetry than the device in figure 5.8, not only with respect to the conductance but also the Raman characteristics.

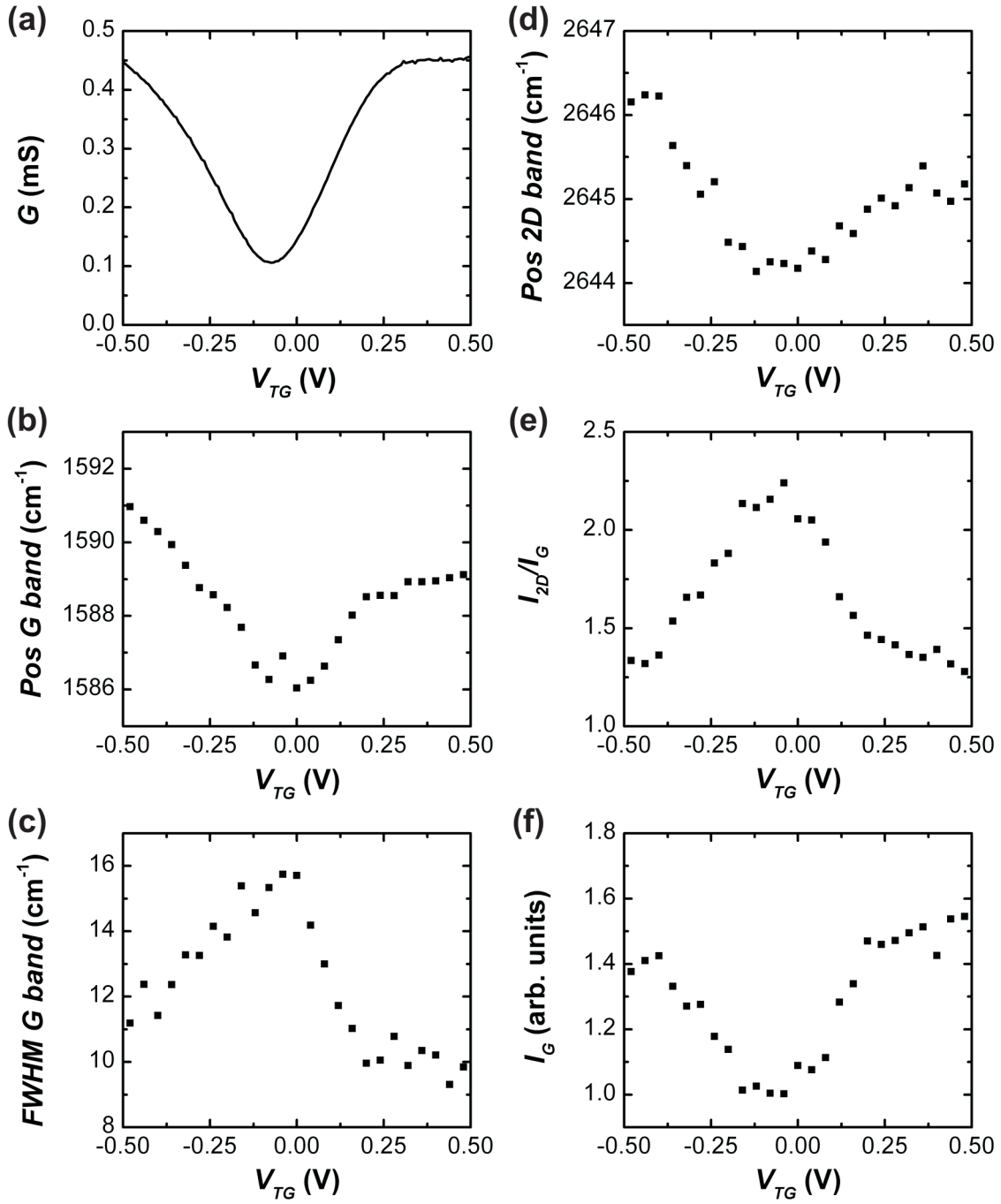


Figure 5.8.: Transport and Raman measurements of the pristine graphene device in figure 5.5, recorded with a solid polymer electrolyte gate. (a) Transfer curve. (b) Position of the G band (Pos G) and (c) its FWHM vs. V_{TG} . (d) Position of the 2D peak vs. V_{TG} . (e) Ratio of the 2D peak and the G peak intensities vs. V_{TG} . (f) Peak intensity of the G band normalized to the intensity at the charge neutrality point vs. V_{TG} .

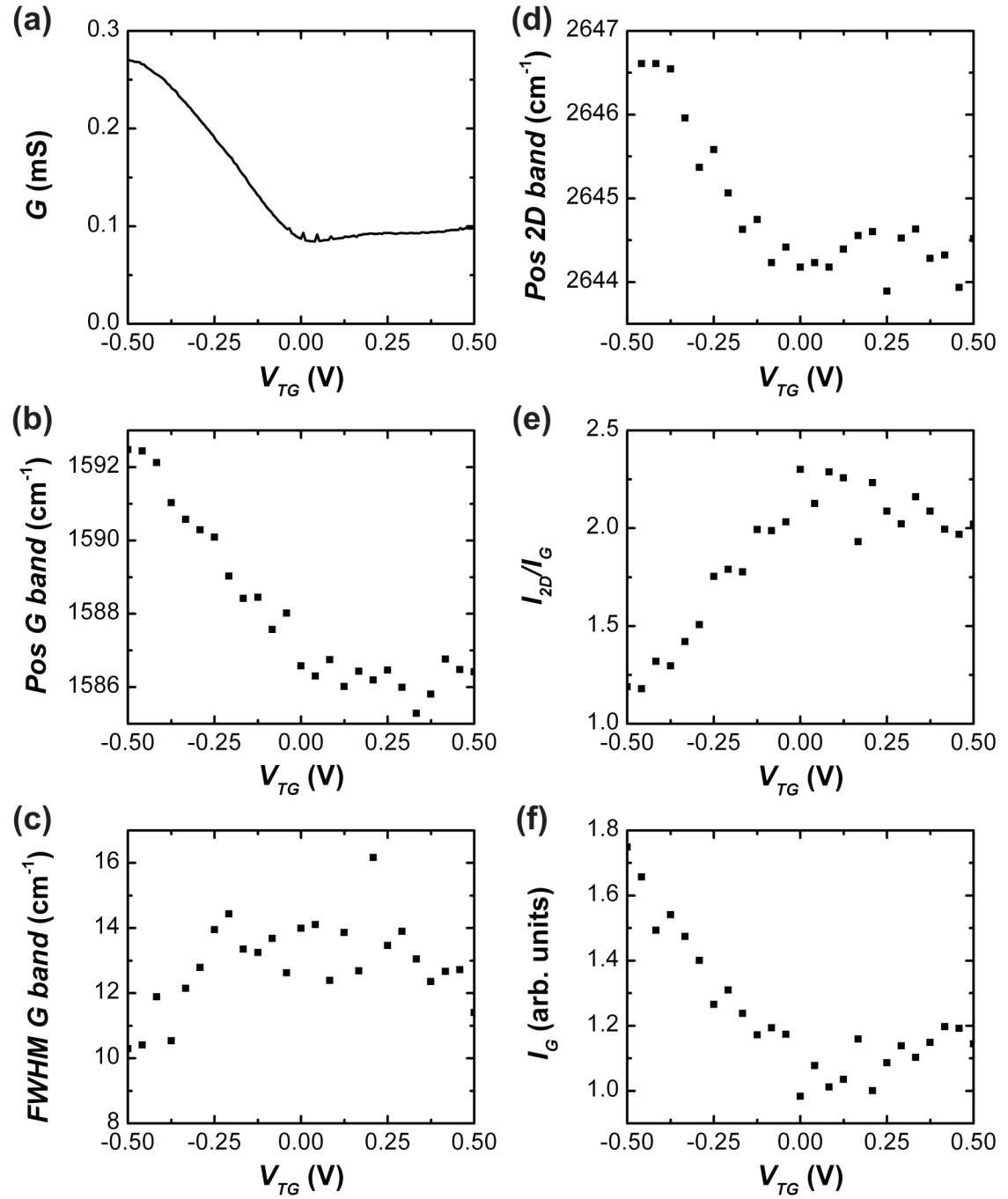


Figure 5.9.: Electrical transport and Raman data of the Ag NP-decorated graphene device, presented in figures 5.4 and 5.5, with a polymer electrolyte topgate.

6. Graphene nanoribbon memory cell

Thus far, memory devices based on graphene have been realized via nanoelectromechanical breaking and switching of graphene under high vacuum conditions, which results in a very low off-current.[142, 143, 144] However, the mechanism operative in such memory devices has not yet been clarified. The situation is further complicated by the fact that on the one hand cyclable conductance switching has been reported in devices solely consisting of electrodes on SiO_2 interrupted by nanogaps,[145] while on the other hand switching was observed also in suspended graphene.[146] By comparison, in the present thesis a graphene nanoribbon (GNR) memory cell based on a non-destructive storage mechanism is demonstrated.

The GNR memory devices were fabricated by Ar ion-beam etching (IBE) of graphene monolayers using V_2O_5 nanofibers (NFs) deposited from aqueous solution as etching mask (see section 4.2). In addition to the source and drain contacts at the NF ends, in all devices control electrodes were attached to the bare graphene and a NF on SiO_2 . The resulting contact configuration is exemplified in the inset of figure 6.1b. In order to etch the unprotected graphene, the samples were briefly (3 s) exposed to an Ar IBE, followed by removal of remaining parts of the V_2O_5 NFs by dilute HCl solution (see figure 6.1a). The last step was optional, as the device operation proved to be independent of the presence of residual V_2O_5 . A negligible electrical conductivity of the unprotected graphene ($>100 \text{ G}\Omega$) could be confirmed with the help of control electrode C_1 . The control electrode C_2 was used to determine the resistance change of the V_2O_5 NF upon etching, whereupon an increase from $100 \text{ M}\Omega$ to insulating ($>100 \text{ G}\Omega$) was found. Accordingly, after etching finite resistance was detectable only between the S and D electrodes (always $<50 \text{ M}\Omega$).

6.1. Electrical characterization of the graphene nanoribbons

The transfer curve (drain current I_D vs. gate-source voltage V_{GS}) of a representative GNR memory device, acquired under ambient conditions, is depicted in figure 6.1b. It exhibits a pronounced hysteresis, with an on/off ratio of 5 (points L and N_L) in

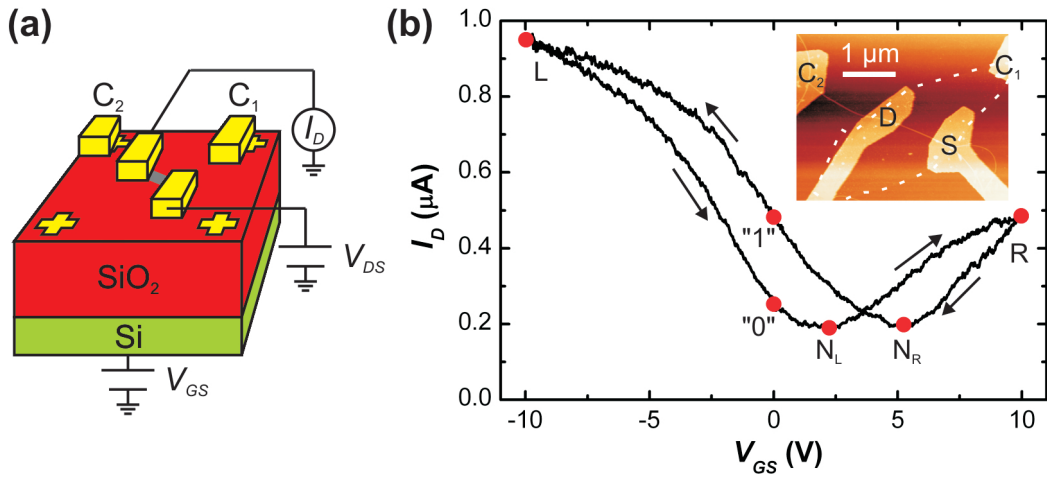


Figure 6.1.: (a) Schematic depiction of a contacted GNR in conventional field-effect transistor configuration. (b) Transfer curve of an exemplary GNR memory device recorded under ambient conditions at a drain-source voltage $V_{DS} = 1$ V. The gate sweep direction is indicated by the arrows. The left and right turning points of the sweep are denoted by L and R, respectively, and the current minima along the corresponding sweeps by N_L and N_R . The total sweep time is 9 min. Inset: AFM topography image of a GNR memory device before Ar IBE. The GNR is contacted by source (S) and drain (D) electrodes. Control electrodes C_1 and C_2 serve to test the resistance of the monolayer graphene (highlighted by white dashed line) and the V_2O_5 NF after etching, respectively.[147]

the full voltage range, and 2 at $V_{GS} = 0$ V (points "0" and "1"). The hysteresis allows selection of a gate voltage at which the GNR assumes two different conductance states depending on the sweep direction.[148, 149, 150] In order to eliminate static power dissipation in the input stage, these two states (marked by "0" and "1" in figure 6.1b) are chosen at $V_{GS} = 0$ V.

While a higher on/off ratio can be obtained by longer etching, this also increases the on resistance and thus slows the device operation (see section 6.5). In addition, the on/off ratio of fabricated devices was found to increase upon cooling, a well known behavior of GNRs.[65, 66] Figure 6.2 shows the evolution of the transfer curve of another GNR device as the temperature is decreased. The on/off ratio in the gate voltage range $|V_{GS}| < 40$ V is 22 under ambient conditions, 187 at 164 K, and >1000 at 2 K.

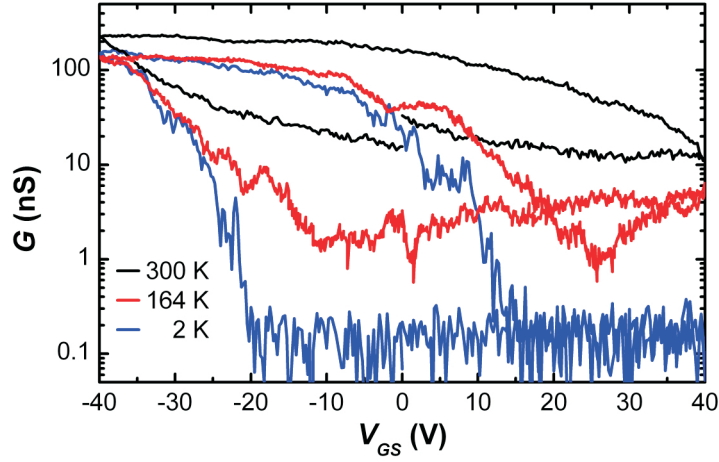


Figure 6.2.: Transfer curve (i.e., conductance G vs. gate-source voltage V_{GS}) of another GNR device, acquired under ambient conditions (black), $T = 164$ K (red), and $T = 2$ K (blue).[147]

6.2. Memory effect

A static pulse response measurement of the device in figure 6.1 is presented in figure 6.3. Triggering was done using a bipolar pulse-wave signal with a period of 3.5 min and a duty cycle of 10 % which ensures stable and well-distinguished "0"

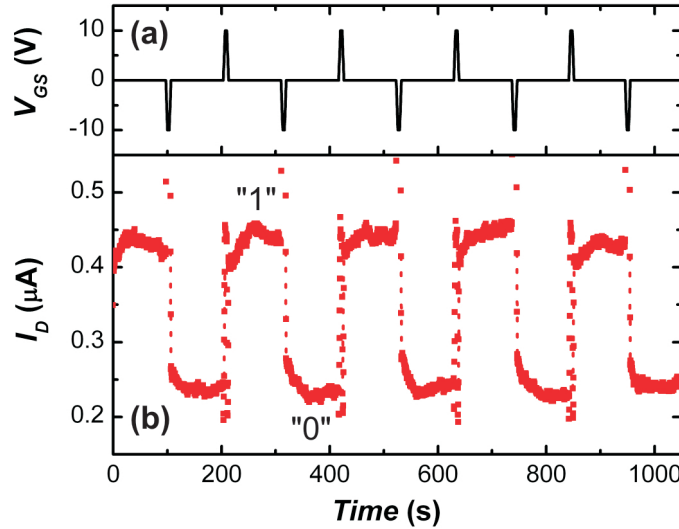


Figure 6.3.: Memory effect. (a) Switching of the GNR device in figure 6.1 by a trigger signal with an amplitude 10 V and a duty cycle of 10 %. (b) Drain current measured under ambient conditions at $V_{DS} = 1$ V.[147]

and "1" states are reached. At such a low clock rate, the "1"/"0" ratio observed in figure 6.1 is preserved. When the device is in the "0" state, a positive pulse moves the operating point as $"0" \rightarrow N_L \rightarrow R \rightarrow N_R \rightarrow "1"$ (figure 6.1), i.e., the device flips its state and remains in the new ("1") state even after the gate voltage is reset. Since the currents in the "0" and "1" states are between the currents at the point R and the charge neutrality points N_L and N_R , both a current overshoot and undershoot occur during the pulse. Similarly, a negative gate pulse moves the operating point as $"1" \rightarrow L \rightarrow "0"$ which restores the "0" state of the memory. In this case, only a current overshoot (at point L) is detected during the negative pulse.

6.3. Dynamic pulse response measurements

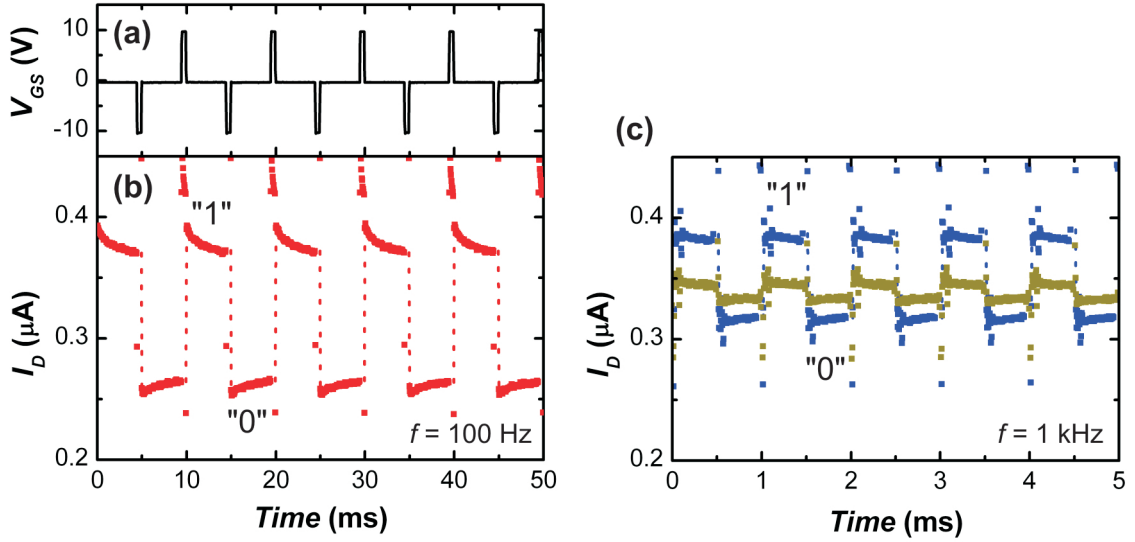


Figure 6.4.: Digital waveforms gained from the device of figure 6.1 under ambient conditions. (a) Trigger signal with a frequency $f = 100$ Hz and a duty cycle of 10 %. (b), (c) I_D at $V_{DS} = 1$ V recorded with an input signal frequency of $f = 100$ Hz (panel b) and $f = 1$ kHz (panel c). At 1 kHz, two different duty cycles were used: 10 % (blue; pulse duration of $50 \mu s$) and 0.1 % (yellow; pulse duration of 500 ns).[147]

Corresponding dynamic pulse response measurements at two different clock rates of the input signal are shown in figure 6.4. The device was triggered with a bipolar pulswave signal with frequencies of up to 1 kHz. At the latter frequency, the difference between the currents in the "0" and "1" state is reduced due to the shorter pulse duration.[151] This effect is more pronounced for extremely small duty cycles,

such as 0.1 % in figure 6.4c. In this case, the pulse duration is only 500 ns at 1 kHz, resulting in a difference between the "0" and "1" currents of only 5 %. Compared to the pulse durations in the range of 1 to 10 ms reported for carbon nanotube (CNT) memories with a SiO₂ gate dielectric the present devices can be switched approximately three orders of magnitude faster.[149, 152, 153] The highest operating clock frequency was found to be ~ 5 kHz (at a duty cycle of 10 %), which is not limited by the device itself but rather by the bandwidth of the current sense amplifier used to measure the drain current. The obtained high clock rate, which exceeds that reported for other CNT and graphene memory devices by several orders of magnitude,[142, 153] demonstrates that it is not only possible to trigger the device with very short pulses, but also that the device has a very short transition time (< 1 ms). Such clock rates are not available for other CNT or graphene memory devices, for which transition times are not explicitly given. Even faster and more stable charging/discharging may be achievable with different gate dielectrics,[153] or by an improved etching process which reduces the on-resistance of the GNRs.

6.4. Origin of hysteresis

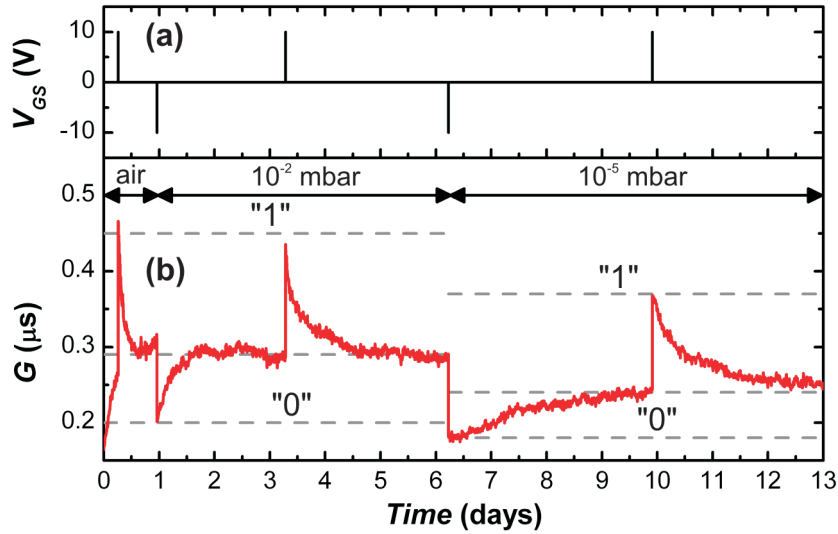


Figure 6.5.: Data retention in the un-powered memory device of figure 6.1. (a) Trigger signal. (b) Conductance acquired under ambient conditions and two different pressure regimes.[147]

The atomic force microscopy and Raman data in section 4.2 evidence that the Ar IBE etching of graphene does not leave sufficient residual carbon to influence device operation. This hints toward charge trapping by water molecules around the

GNR as origin of the hysteresis.[148, 154, 155, 156, 157] This assertion is further supported by the retention time measurements shown in figure 6.5. In contrast to non-volatile CNT memory devices,[148, 149, 150] the GNR memory cell was found to be volatile under ambient conditions. The "0" and "1" state slowly drifted to an intermediate conductance over ~ 6 hours, as apparent from figure 6.5. This drift was observed both in powered ($V_{DS} = 1$ V constantly applied) and unpowered ($V_{DS} = 1$ V only applied for data acquisition) devices and could be significantly reduced by placing the samples in vacuum. The traps were found to discharge over approximately 1 day at a pressure of $\sim 10^{-2}$ mbar and >3 days at 10^{-5} mbar. One further gate sweep proved sufficient to charge the traps and restore the states. The appreciable volatility under ambient suggests a sizeable interaction between water molecules and functional groups on the SiO_2 (e.g., silanol groups), or hydroxyl groups located at the GNR edges.[155, 157, 158]

The importance of surface water gains further support from the device behavior at low temperatures (100 K), where no discharging was observed over prolonged periods of time (>2 days; see figure 6.6), most likely because the surface water is frozen.

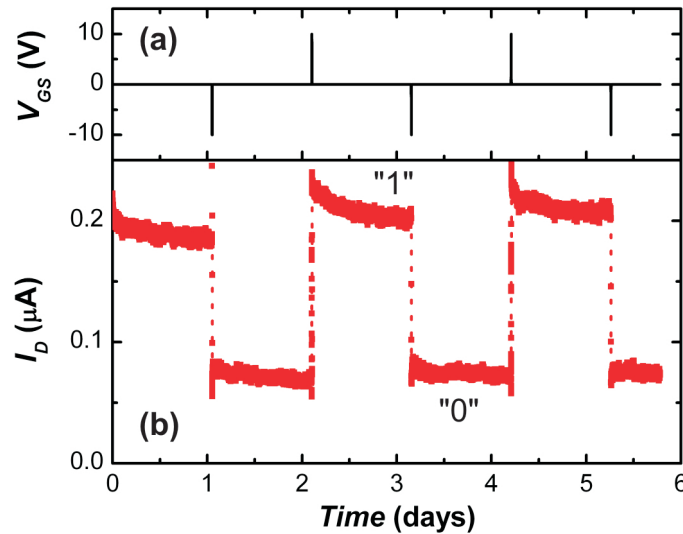


Figure 6.6.: Data retention in a different GNR memory device at $T = 100$ K. (a) Trigger signal. (b) The measured drain current. Data is read every 10 s at the drain voltage $V_{DS} = 1$ V.[147]

The influence of water molecules was also confirmed by sample annealing. Figure 6.7 shows a transfer curve of a GNR before and after annealing. Before annealing, the GNR exhibited strong hysteretic behavior. After annealing in vacuum

($\sim 10^{-6}$ mbar) at 160 °C for 2 hours, the sample was transported in air and placed in a measurement setup under vacuum ($\sim 10^{-5}$ mbar). The subsequently recorded transfer curve revealed less hysteresis than before annealing, underscoring the influence of water molecules.[154, 155] However, the hysteresis could not be completely eliminated by annealing, as this would require freely suspended GNRs.[154]

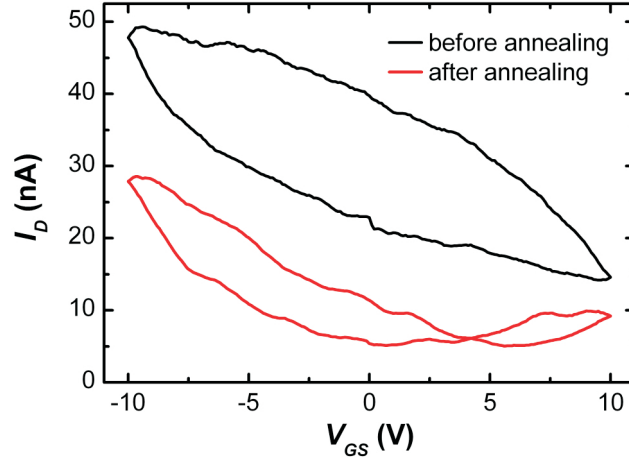


Figure 6.7.: Transfer curve of a GNR before (black) and after (red) vacuum annealing (10^{-6} mbar, 160 °C, 2 hours).[147]

It is noteworthy that the stored data could be retained during the same period of time even if the device was powered by $V_{DS} = 1$ V, demonstrating its good durability and stability. The device could also be operated for many hours at various clock rates (< 10 kHz) and temperatures without any degradation or failure, yielding an endurance of $> 10^7$ cycles. These characteristics render the GNR devices interesting for application as static random access memory or non-volatile flash memory cells.

6.5. Influence of etching time on hysteresis and device operation

Non-etched graphene samples were found to exhibit a small or no hysteresis at all in the gate-source voltage range of the trigger signal ($|V_{GS}| < 10$ V). Figure 6.8 shows the transfer curves $I_D(V_{GS})$ of two different samples under ambient conditions. The sample in figure 6.8a shows a behavior typical for all the investigated samples, i.e., it exhibits sizeable hysteretic behavior only in a very large gate voltage range,[159] while the hysteresis decreases, when the gate-source voltage range is reduced to that

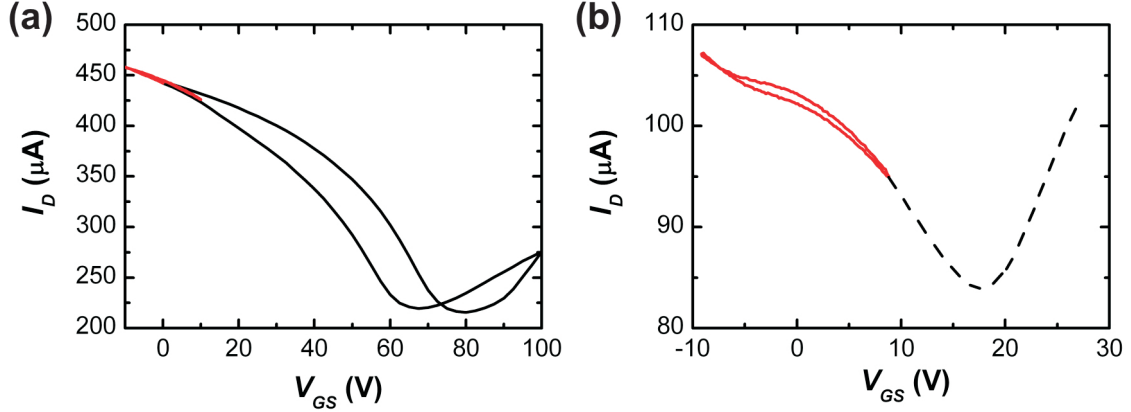


Figure 6.8.: Transfer curves of two different unetched graphene samples recorded under ambient conditions at a drain-source voltage $V_{DS} = 1$ V. In sample (a) two different gate voltage ranges were used: $0 \text{ V} < V_{GS} < 100 \text{ V}$ (black) and $|V_{GS}| < 10 \text{ V}$ (red). The curves were recorded in the static mode under the same conditions as the transfer curve shown in figure 6.1. In sample (b) the transfer curve was recorded in the dynamic mode under the same conditions as the measurements shown in figure 6.4b ($f = 100 \text{ Hz}$). The gate voltage range is $|V_{GS}| < 10 \text{ V}$. The dashed line indicates the position of the Dirac point.[147]

of the trigger signal. The sample in figure 6.8b displayed the most pronounced hysteresis of all investigated samples in this gate-source voltage range. However, the "1"/"0" ratio at $V_{GS} = 0 \text{ V}$ is only 1.01, which renders the memory states essentially indistinguishable.

IBE resulted in the appearance of a pronounced hysteresis in the transfer curve in a voltage range of the trigger signal and an increase in the "1"/"0" ratio at $V_{GS} = 0 \text{ V}$. For the present samples, the very thin V_2O_5 NF masks are not capable of entirely protecting the underlying graphene from the ion beam, such that the etching time had to be limited in order to keep the on resistance sufficiently low ($\sim \text{M}\Omega$) to clock the devices in the lower radio-frequency range ($\sim \text{kHz}$). The best results have been attained for short etching times ($\sim 3 \text{ s}$), yielding GNRs with a resistance of $\sim 1 \text{ M}\Omega$ (for a typical GNR length $\sim 1 \mu\text{m}$) and an "1"/"0" ratio of ~ 2 at $V_{GS} = 0 \text{ V}$, as described before. Moderate etching times ($\sim 5 \text{ s}$) increased the on-resistance ($\sim 50 \text{ M}\Omega$) and slowed the device operation. However, this also improved the on/off ratio, probably because longer etching made the GNRs narrower. Finally, long etching times ($> 5 \text{ s}$) resulted in non-conductive GNRs.

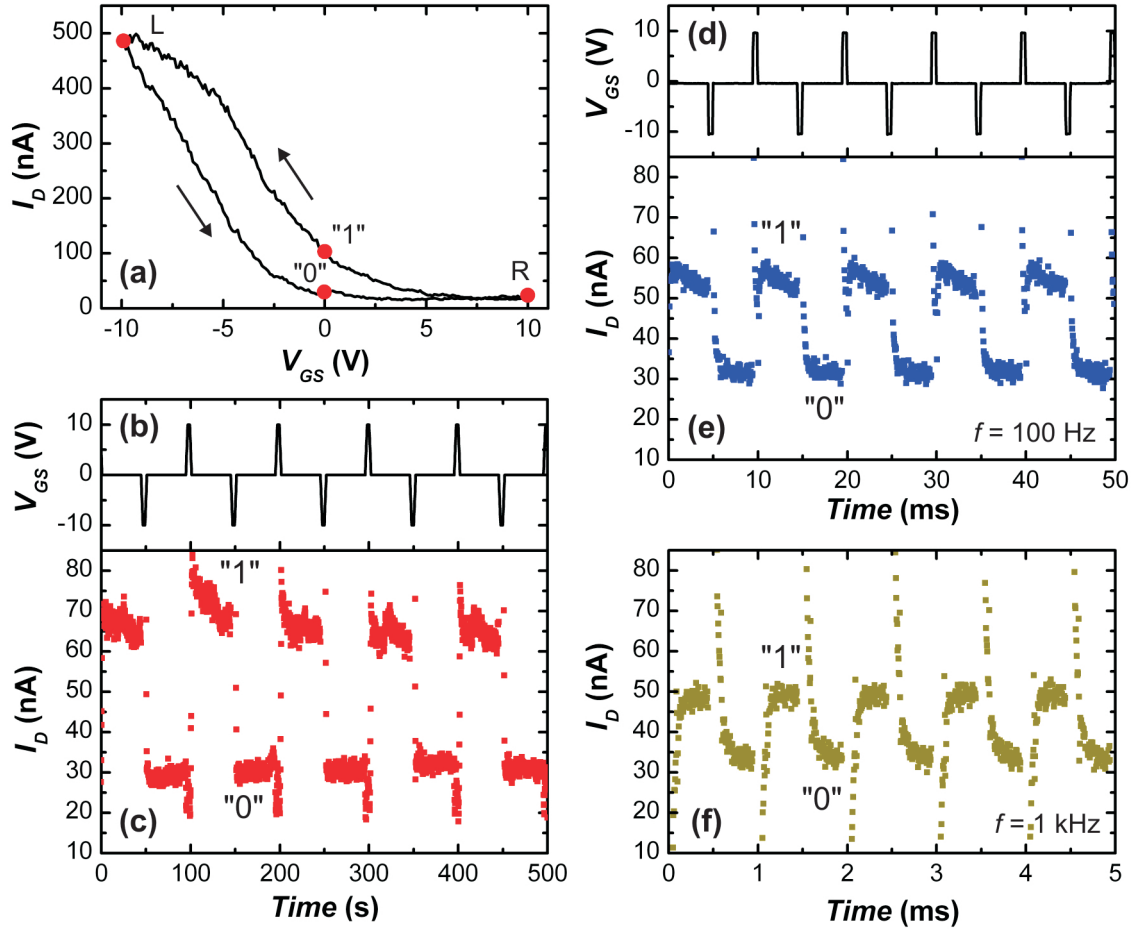


Figure 6.9.: Operation of a GNR memory device etched for 5 s. The device was measured under ambient conditions at a drain-source voltage $V_{DS} = 4$ V. (a) Transfer curve of the device. The gate sweep direction is indicated by the arrows. The left and right turning points of the sweep are denoted by L and R. (b) Switching of the device in a static pulse response mode by a trigger signal with an amplitude 10 V and a duty cycle of 10 %. (c) Drain current in a static pulse response mode. (d) Switching of the device operated in a dynamic pulse response mode by a trigger signal at a frequency $f = 100$ Hz and a duty cycle of 10 %. (e), (f) Digital waveforms for I_D recorded with an input signal frequency of $f = 100$ Hz (panel e) and $f = 1$ kHz (panel f).[147]

The operation of a representative memory device etched for 5 s is demonstrated in figure 6.9. All measurements were performed under ambient conditions. Due to the larger resistance compared to devices etched for 3 s, this device exhibits lower on- and off-current levels. Although the bias (V_{DS}) did not influence the "1"/"0"

ratio at $V_{GS} = 0$ V, the device was biased with $V_{DS} = 4$ V (instead of 1 V used before) in order to increase the absolute difference between "0" and "1" currents and make them distinguishable even at a frequency $f = 1$ kHz. The transfer curve of the device, depicted in figure 6.9a, displays a pronounced hysteresis, with an on/off ratio in the full voltage range of 33.4 (points L and R), and 3.9 at $V_{GS} = 0$ V (points "0" and "1"). Corresponding static pulse response measurements are presented in figure 6.9b and c. Triggering was done using a bipolar pulse-wave signal with a period of 100 s and a duty cycle of 10 %. In this case, the "1"/"0" ratio at $V_{GS} = 0$ V is reduced to 2.3 due to a reduction in the "1" current in the pulsed mode of operation. Dynamic pulse response measurements at two different clock rates of the input signal are shown in figure 6.9d, e and f. The device was triggered with a bipolar pulse-wave signal with frequencies of up to 1 kHz. At the latter frequency, the difference between the currents in the "0" and "1" state is reduced owing to the shorter pulse duration.[151]

7. Spatially resolved photocurrents in graphene nanoribbon devices

Recently, the optoelectronic properties of pristine or patterned graphene have received strong attention.[160] For example, due to its linear dispersion relation and the Pauli blocking principle, graphene possesses wavelength-independent ultrafast saturable absorption, which has motivated the exploration of graphene as a component of mode-locked lasers.[161] The high charge carrier mobility in graphene in combination with a short photocarrier lifetime make it interesting as an ultrafast photodetector, which displays zero dark current as no bias needs to be applied.[162, 163]

On the more fundamental side, the mechanism of photocurrent generation at the graphene/metal interface has attracted attention.[164, 165, 166, 167, 168] The pioneering scanning photocurrent microscopy (SPCM) experiments on graphene transistors have been interpreted based upon the presence of local built-in electric fields at the metal contacts.[164] Moreover, the spatially resolved photocurrent images have revealed that the photoresponse at the graphene edges switches at a different gate-source voltage than the main sheet. This behavior has been explained by an altered coupling of the gate to the edges and the presence of localized edge states. Furthermore, photocurrent spots distributed over the graphene sheet have been attributed to electron-hole puddles.[81, 164] A photocurrent response has also been detected at the interface between mono- and bilayer graphene.[169] The determined polarity of the photocurrent signal while varying the Fermi level has identified the photo-thermoelectric Seebeck effect as the origin of photocurrent generation for this specific device configuration, whereas a sign with opposite polarity would be expected for the built-in electric field mechanism.[169] Further studies have addressed photocurrent generation in graphene p-n junctions obtained through chemical or electrostatic doping.[170, 171] The processes limiting the speed of graphene-based photodetectors have been evaluated using an optical correlation pump-probe technique with ultrashort laser pulses.[172, 173] An intrinsic response time of ~ 2 ps corresponding to a bandwidth of ~ 500 GHz has been observed/found, which is limited by three major factors, namely the relaxation of the photoexcited carriers via emission of phonons, their recombination and the transit time out of the excitation area.

In order to improve the performance of graphene photodetectors by converting light more efficiently into an electrical signal, several approaches have been followed. By combining graphene with plasmonic nanostructures, the responsivity could be increased from ~ 1 mA/W up to several 10 mA/W, due to efficient field concentration in the area of photocurrent generation.[174, 175] Additionally, wavelength and polarization selectivity have been achieved through nanostructures of different geometries.[174, 175] One possibility to increase the optical field by approximately a factor of 20 is to integrate graphene with a Fabry-Pérot microcavity, where the field enhancement occurs only at the design wavelength.[176] Since the photon lifetime in the cavity is in the fs range, no increase in the response time of the graphene photodetector can be expected.

With regard to GNRs, although their dark electrical properties have been experimentally investigated to some extent,[65, 66, 83, 84, 114, 120, 177] their optoelectronic behavior has thus far been addressed only by theory.[178] In this thesis, SPCM is used to study the spatially resolved photocurrent response of individual graphene nanoribbons (GNRs) of high structural quality. In contrast to extended graphene sheets, in these experiments the entire width of the conducting channel (GNR width ~ 10 to 20 nm) is illuminated by the laser spot (~ 500 nm diameter), such that potential complications due to inhomogeneous temperature and/or electric field gradients over the channel width are avoided.

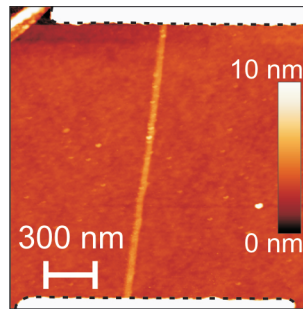


Figure 7.1.: AFM image of a 22 nm wide, electrically contacted GNR. The distance between the contacts is $1.5 \mu\text{m}$.

The GNRs used in the SPCM measurements were fabricated using CdSe nanowires (NWs) as etching mask (see section 4.3). As shown in figure 4.9 in the GNR fabrication chapter, the width of the GNRs agrees well with the diameter of the corresponding NWs. In most cases, metal contacts were defined after completely dissolving the CdSe NWs by wet etching. The exemplary atomic force microscope (AFM) image in figure 7.1 testifies a regular structure and clean surface of the resulting GNRs.

7.1. Electrical characterization of the graphene nanoribbons

7.1.1. CdSe nanowire etching mask removed

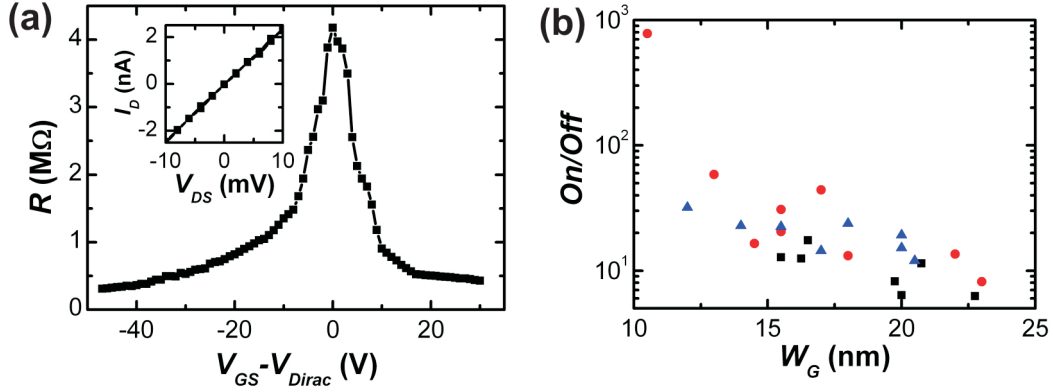


Figure 7.2.: Electrical characterization of GNR devices under ambient conditions. (a) Electrical resistance as a function of V_{GS} for the device shown in figure 7.1 ($V_{Dirac} = +10$ V in this case). Inset: I_D vs. V_{DS} curve at the Dirac point. (b) On/off ratio plotted against ribbon width. The on conductance is measured in the p-type regime at $V_{GS} - V_{Dirac} = -30$ V. In total 24 GNR devices on three different chips (designated by black squares, red circles, and blue triangles, respectively) were evaluated.

The devices were electrically characterized under ambient conditions. In general, the I_D vs. V_{DS} curves showed a linear dependence, as exemplified by the inset in figure 7.2a for the GNR in figure 7.1. From the transfer curves revealing ambipolar behavior, an on/off ratio was determined by dividing the resistance at the Dirac point by the resistance determined well within the p-type regime (at $V_{GS} - V_{Dirac} = -30$ V).[179] For the present device with $V_{Dirac} = +10$ V, an on/off ratio of 14 is obtained. Figure 7.2b shows the dependence of the on/off ratio on the ribbon width, W_G , for in total 24 different GNR devices. With decreasing width, the on/off ratio increases, reaching almost 3 orders of magnitude for a ~ 10 nm wide GNR. This trend is consistent with the opening of a transport gap E_{gap} (see section 2.2), which is inversely proportional to W_G , $E_{gap} \sim \frac{1}{W_G}$. [65, 66, 120] The obtained on-resistance values and on/off ratios agree well with previous reports on GNRs with comparable widths.[120, 179, 180] However, further characteristics like an exponentially increasing $R \cdot W_G$ vs. L_G relationship (L_G is the GNR length), suggestive of an edge effect through a strong localization transport regime,[179] could not be observed. This

may be due to the fact, that the present transport setup does not allow heating in vacuum to remove extrinsic dopants, as has been done in reference [179].

7.1.2. CdSe nanowire left on top

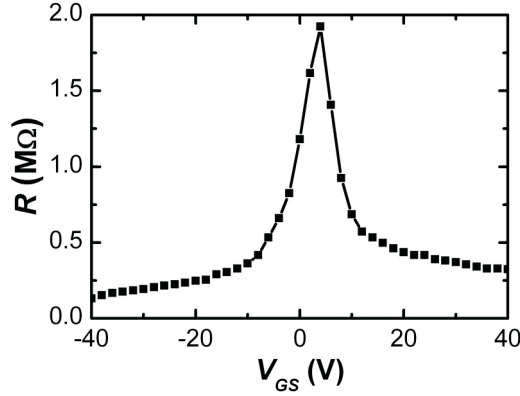


Figure 7.3.: Transfer curve of a GNR (~ 20 nm width) with CdSe NW etching mask remaining on top (ambient conditions).

To determine the influence of the wet chemical removal of the CdSe NW, GNR devices with CdSe NWs remaining on top were electrically characterized. To this end, CdSe NWs were deposited onto graphene, and then contacts defined by e-beam lithography and thermal evaporation (2 nm Cr + 55 nm Pd). Subsequently, reactive ion etching was used to etch unprotected graphene, whereupon the contacts act as a protective mask. Upon application of a drain-source bias to the completed devices, current flows from the metal contacts through the graphene into the GNR. The CdSe NWs do not contribute to the transport as they are non-conductive (as confirmed with the aid of control electrodes). Figure 7.3 shows the transfer curve of a 20 nm wide GNR device prepared in this manner. The Dirac point occurs at $V_{GS} = +4$ V, close to the value of +10 V for the device described above (figure 7.1). For some devices with removed CdSe NW the Dirac point was close to 0 V, testifying that no appreciable doping is introduced by the wet chemistry. The on/off ratio of 11 is comparable to that of devices with the CdSe NW removed. Likewise, the on-resistance of devices with CdSe remaining on top is similar to the ones with CdSe NW removed. It is hence concluded that no additional scattering is introduced by the CdSe NW removal, i.e., the electrical transport properties of the GNR devices are undisturbed. This behavior is distinguished from other cases like exposure to the e-beam resist hydrogensilsequioxane, whereby additional scattering or doping

is introduced.[118] For all data presented in the following sections, the CdSe NW etching mask was removed.

7.2. Photocurrent measurements

The spatially resolved photoresponse of the GNRs was measured using a confocal microscope operated in air. The employed set-up is schematically depicted in figure 7.4a. In the experiments, unbiased devices were raster-scanned (lateral step size of ~ 60 nm) through the approximately 500 nm wide laser spot (linearly polarized light with $\lambda = 633$ nm and a power of $240 \mu\text{W}$ was used to ensure a good signal-to-noise ratio), while recording the electrical current for each position. In all photocurrent measurements, no drain-source voltage was applied (except the control measurements in figure 7.8). The possibility to rotate the sample and hence the GNR axis relatively to the plane of the incoming light was realized by the construction of a rotatable sample holder (see figure 7.4b).

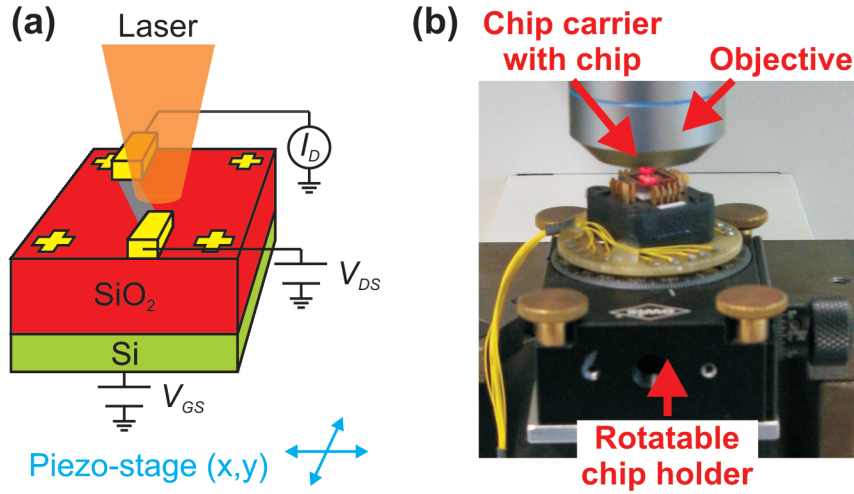


Figure 7.4.: (a) Schematic illustration of the scanning photocurrent microscopy setup (SPCM). (b) Picture of the rotatable chip holder.

An optical reflection image of the device in figure 7.1 is displayed in figure 7.5a, where due to the low reflection intensity of the GNR only the electrodes can be discerned. As illustrated by figure 7.5b, in the p-type regime (gate-source voltage $V_{GS} - V_{Dirac} = -36$ V, $V_{DS} = 0$ V) a positive photocurrent of ~ 2 nA is detected at the source contact, while a negative current of similar magnitude occurs at the drain contact. Upon transition from the p-type to the n-type regime (i.e., by applying a

positive gate-source voltage), the photocurrent at the source contact changes sign from positive to negative, while a positive current emerges at the drain contact, as apparent from figure 7.5c. Such sign reversal of the photocurrent signals upon gating is well-documented for graphene.[164, 165, 166, 167] It is noteworthy that in all GNR devices no difference could be observed between parallel and perpendicular polarization direction of the incident laser light with respect to the long axis of the GNR. This finding is in contrast to the report of Shi et al.,[181] and most likely due to the fact that the latter work involved nanogap electrodes as plasmonic antenna.

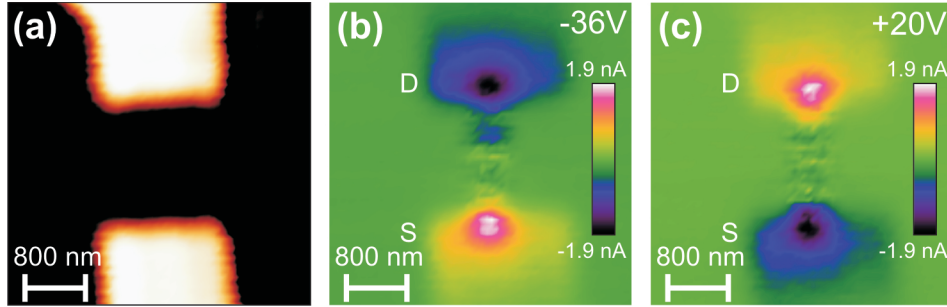


Figure 7.5.: SPCM measurements on the device in figure 7.1 (step size of the laser spot ~ 62 nm). (a) Optical reflection image recorded during the photocurrent measurement, revealing the two metal contacts. (b) SPCM image in the p-type regime of the device ($V_{GS} - V_{Dirac} = -36$ V, $V_{DS} = 0$ V). The two photocurrent peaks are respectively denoted as S and D, according to their nearby electrodes. (c) SPCM image recorded in the n-type regime at $V_{GS} - V_{Dirac} = +20$ V.

7.2.1. Built-in electric field model

The photocurrent generation in extended graphene has been attributed to the presence of local built-in electric fields which separate photoexcited electron-hole pairs. [164, 165, 166, 167, 168] Such fields are typically present at the electrical contacts, and their magnitude depends on the difference in the work functions of the contact metal and the graphene (see section 2.5). To evaluate whether this mechanism can explain the photocurrent generation at the GNR/metal junction, we compare the corresponding local photocurrent signals detected from GNRs with different dimensions. In order to exclude the influence of different charge carrier concentrations in the devices, the comparison is made at high carrier densities in the p- or n-type regime. The photocurrent caused by the built-in field is given by $I_{Photo} = W_G \cdot e \cdot n^* \cdot \xi$, where e is the elementary charge, n^* the photoinduced carrier density, and ξ the built-in field.[103, 182] It is noteworthy that the light power

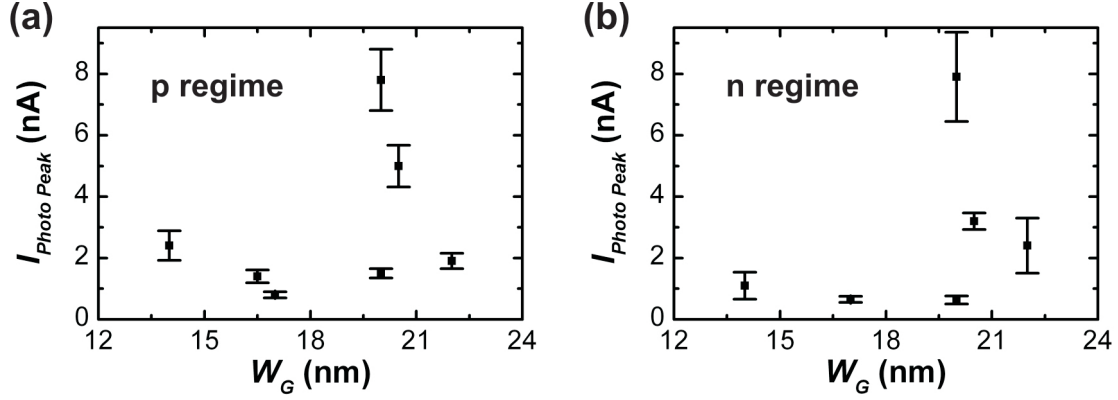


Figure 7.6.: Photocurrent detected close to the metal contact in dependence of the GNR width. The gate voltage was adjusted to $V_{GS} \sim -30$ V for the p-type regime (a), and $V_{GS} \sim +30$ V in case of the n-type regime (b). Error bars correspond to the standard deviation determined by averaging over several measurements.

per area should be constant over the GNR width W_G , as the latter is much smaller compared to the approximately 500 nm wide laser spot. For both gating regimes, the measured photocurrent as a function of W_G (see figure 7.6) displays a pronounced scatter rather than a linear dependence. This observation is incompatible with the built-in field mechanism, although it may be argued that work function differences between the GNR devices could have a profound influence. However, this scenario is unlikely considering the fact that even GNRs with the same width and on/off ratio exhibit notably different photocurrents, as apparent from table A.1 (see appendix - photocurrent data of GNRs).

This conclusion remains valid also when partial recombination of the excited carriers is taken into account. Up to this point, it was assumed that all electron-hole pairs get separated. In the following, we consider the effect of the recombination of excited charge carriers by including the mobility μ of each measured device.[182] The carrier transit time in the built-in field region and hence the number of recombining electron-hole pairs should rise with decreasing carrier mobility of the GNRs.[172] This dependency can be described by the equation $I_{\text{Photo}} = W_G \cdot e \cdot n^* \cdot \xi \cdot \mu$. [182] The mobility for each device can be obtained by fitting the transport data away from the Dirac point, for the hole and electron regime separately, by the equation

$$R = R_C + \frac{L_G}{W_G} \cdot \frac{1}{e \cdot \mu \cdot \sqrt{n_0^2 + n^2}},$$

where R_C is the contact resistance, L_G the channel length, and n_0 the density of

carriers at the Dirac point.[183] The gate-dependent carrier density n is calculated with the following expression for the capacitance, which includes fringing effects:[184]

$$C_{ox} = \epsilon_{ox}\epsilon_0 \left(\frac{1}{t_{ox}} + \frac{\pi}{W_G \cdot \ln[6 \cdot (\frac{t_{ox}}{W_G} + 1)]} \right).$$

Thus obtained values of $I_{Photo}/(W_G \cdot \mu)$ still are not constant (see table A.1).

7.2.2. Photo-thermoelectric Seebeck effect

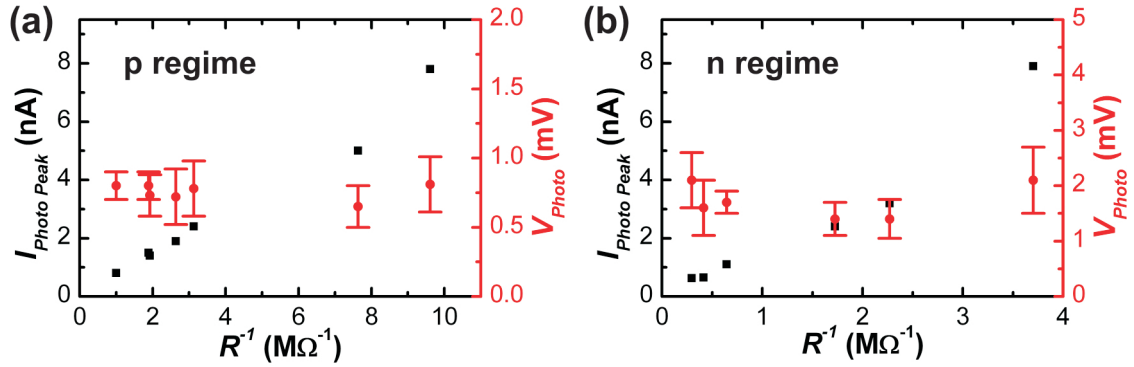


Figure 7.7.: Photocurrent (black squares) and calculated photovoltage values (red circles) in dependence of the inverse of the measured Ohmic resistance of several GNR devices for the p-type regime (a) and the n-type regime (b). Error bars correspond to the standard deviation determined by averaging over several measurements.

In contrast to the plot of I_{Photo} vs. W_G , a linear dependency exists between I_{Photo} and the inverse resistance of the GNRs (see figure 7.7). The photocurrent rises linearly with the inverse resistance, with an overall increase by a factor of approximately 10 in both regimes. It turns out that very similar photovoltage values are obtained by multiplying the (dark) electrical resistance at a fixed gate-source voltage $R(V_{GS})$ with the photocurrent peak magnitude $I_{Photo}(V_{GS})$ under the same condition, as evident from the corresponding plots in figure 7.7.

Figure 7.8a presents I_D vs. V_{DS} curves acquired at $V_{GS} = +30$ V of the device in figure 7.1. The laser was fixed at one position while the current was measured. The black curve was obtained with the laser spot kept at the source contact (S), representing the position of maximal photocurrent generation. Compared to the red curve (recorded with laser turned off), the black curve is shifted to the right. For

the laser spot located at the drain contact, the curve (green symbols) was obtained, which is shifted to the left with respect to the curves recorded in the dark. It follows that the slope of the line is independent of whether the device is illuminated or not. This finding justifies the photovoltage calculation by multiplication of the dark electrical resistance at a specific gate-source voltage with the photocurrent peak magnitude at this gate-source voltage: $V_{Photo}(V_{GS}) = I_{Photo}(V_{GS}) \cdot R(V_{GS})$. The small differences (less than 5 %) between the slopes are attributed to a slight drift of the charge neutrality point with time (see section 6.4). In order to reduce the influence of such effects, the results of several photocurrent measurements on the same device were averaged. On this basis, error bars in figures 7.6 and 7.7 were calculated.

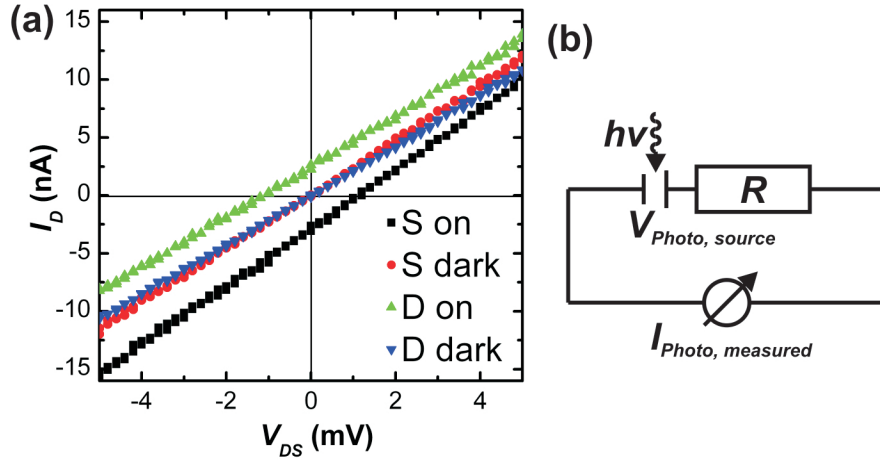


Figure 7.8.: (a) I_D vs. V_{DS} curves recorded at $V_{GS} = +30$ V applied to the device presented in figure 7.1. S: source contact, D: drain contact, on: device illuminated, dark: laser off. (b) Equivalent circuit model to account for the data in (a) and figure 7.7.

Alternatively, the photovoltage may be directly determined as the absolute value of V_{DS} of the intersection of the curves under illumination (S on and D on) with the I_D -axis in figure 7.8a. Unfortunately, these kind of measurements could not be performed, as they would be extremely time-consuming with the current setup.

The observation of an almost constant photovoltage close to the contacts points toward the photo-thermoelectric Seebeck effect as the dominant mechanism responsible for the photocurrent generation (see equivalent circuit in figure 7.8b). This mechanism has been invoked as an alternative to the built-in electric field to explain the photocurrent generation at the graphene/metal or graphene monolayer/bilayer interface, or graphene p-n junctions (see section 2.5).[166, 168, 169, 171] A tempera-

ture difference ΔT between the two graphene/metal interfaces, due to locally heating by the laser spot, produces a thermoelectric voltage $V_{Photo} = (S_G - S_{Metal}) \cdot \Delta T$, where S_G and S_{Metal} are the Seebeck coefficients of the GNR and contact metal, respectively. As a consequence, a thermoelectrically-induced photocurrent is generated whose magnitude scales inversely with the GNR device resistance $I_{Photo} = V_{Photo}/R$.

The Seebeck coefficient S_G can be estimated from the Mott relation:[106, 107]

$$S = -\frac{\pi^2 k_B^2 T}{3e} \cdot \frac{1}{\sigma} \cdot \frac{d\sigma}{dV_{GS}} \cdot \frac{dV_{GS}}{dE}.$$

As the two-probe resistance R and dR/dV_{GS} both depend on the contact resistance of the devices, we derive the magnitude of the latter by fitting $R(V_{GS})$ for holes and electrons separately, and subtract it from R . [183] In this manner, one obtains respective values of $S \approx +30 \mu\text{V/K}$ and $S \approx -40 \mu\text{V/K}$ for the p- and n-type regime of the device in figure 7.1. The finding of a larger Seebeck coefficient in the n- vs. p-type regime is in accord with previous reports, and is explainable by the electron-hole asymmetry introduced by contact doping.[106, 138] The present S values are slightly smaller than the $\sim 50 \mu\text{V/K}$ reported for graphene, which could be explained by the better gate coupling in the GNR devices.[106] The measured photovoltages of 0.76 mV in the p-type and 1.7 mV in the n-type regime yield a respective temperature difference ΔT of ~ 30 K and ~ 40 K between the illuminated region at the GNR/metal interface and the surrounding. The notable difference between the two gating regimes is at least partly due to neglecting S_{Metal} . Interestingly, the above ΔT range significantly exceeds that of $\Delta T \approx 0.1\text{-}1$ K obtained for graphene using comparable laser wavelengths and a power of $40 \mu\text{W}$. [169, 171] This difference cannot be fully accounted for by the higher laser power of $240 \mu\text{W}$ used in the present experiments, thus suggesting a reduced heat transport capability of the GNRs in comparison to graphene.[184] Consequently, heat dissipation is dominated by the SiO_2 substrate and/or the metal contacts rather than the GNR itself.[184] This hypothesis is supported by comparison with Raman spectroscopy studies on GNRs. Prolonged irradiation ($\lambda = 633$ nm, 300 kW/cm^2 intensity) causes photoinduced changes, similar to the effect of thermal heating to 100°C in air.[131] Hence, a few tens of Kelvin seem to be reasonable for our setup (120 kW/cm^2). However, it should be emphasized that even if photocurrent generation in GNRs is predominantly via the photo-thermoelectric mechanism, the situation may be different for extended sheets of graphene, in which heat dissipation is more effective.

8. Edge functionalization of graphene

Graphene as an atomically thin sheet requires doping schemes that are non-intrusive and preserve the pristine lattice, rather than direct incorporation of dopant species into the basal plane, which can severely limit mobility.[45] The edge chemistry of GNRs and geometry is predicted to govern the electronic and magnetic properties, which may be exploited to improve the performance of corresponding devices.[51]

8.1. Functionalization by bromine

The attachment of bromine atoms was tested as a means to saturate the edges of GNRs.[185] Theory predicts that halogen molecules bind preferentially to zigzag edges (figure 8.1a), and thereby enhance the magnetic order, magnetic anisotropy, crossover temperature, as well as spin correlation length in GNRs.[51]

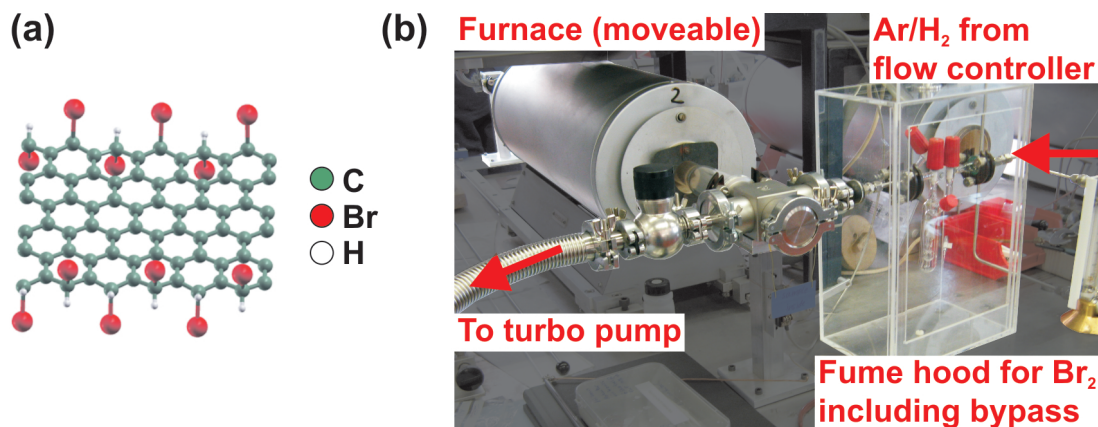


Figure 8.1.: (a) Scheme showing Br atoms at GNR edges. Adapted from reference [185]. (b) Tube furnace used for reacting GNRs with Br₂ vapor.

For the graphene edge functionalization experiments, a tube furnace system was built-up (see figure 8.1b), wherein reactive agents can be supplied from the gas phase.

A clean environment allowing to remove adsorbates from graphene samples prior to the reaction is realized by the possibility to evacuate to low pressures (10^{-6} mbar), subsequent purging with Ar and H₂ and final heating up to 1000 °C.

8.2. Graphite step edges exposed to Br₂

Figure 8.2 shows a scanning electron microscopy (SEM) image of highly oriented pyrolytic graphite (HOPG) heated to 850 °C in forming gas (90 % Ar/10 % H₂), followed by exposure to Br₂ vapor during the 45 min cooling down from 850 °C to 300 °C. To this end, 1 ml Br₂ was filled into a glass storage vessel under Ar atmosphere. During the Br₂ vapor exposure, the bypass valve is closed and Ar gas flows through the vessel into the oven. Samples treated in this way exhibited a clear structure change of the naturally occurring step edges. After heating the same sample again to 850 °C in forming gas, the 50-80 nm wide seams at the edges had disappeared. It could not be clarified, whether a covalent reaction or just intercalation of Br₂ took place at the edges.

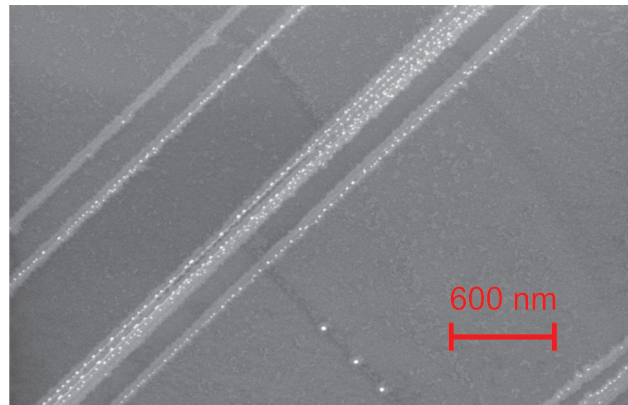


Figure 8.2.: SEM image of HOPG exposed to Br₂ vapor for 45 min during cooling down from 850 °C to 300 °C. [Image taken by R. Preuss]

8.3. Electrical and Raman characterization of Br₂-treated graphene

Graphene monolayers on Si/SiO₂ substrates were exposed to Br₂ vapor at low temperature (≤ 300 °C), under which condition no change of the HOPG edges occurred, as concluded from SEM inspection. Transport measurements at ambient conditions

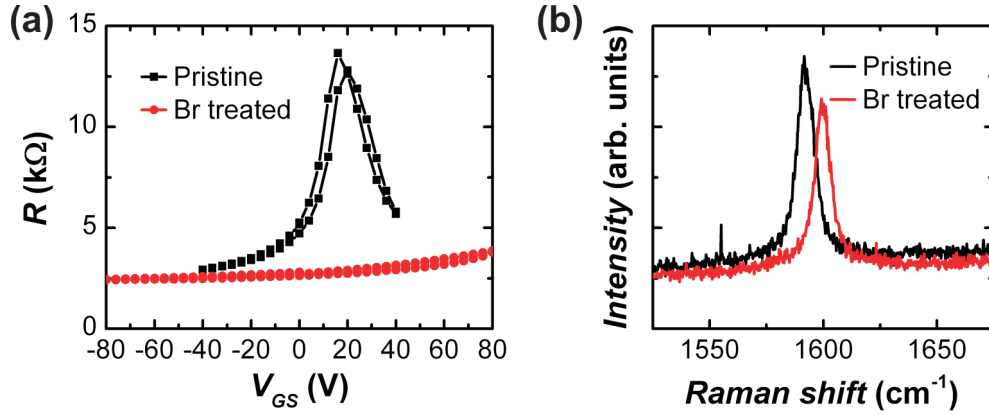


Figure 8.3.: (a) Transfer curve and (b) Raman G-line of a graphene monolayer before (black) and after Br_2 -treatment (red), both recorded under ambient condition. [Raman measurement performed by N. Scheuschner]

showed a pronounced shift of the Dirac point toward positive gate-source voltages (above $V_{GS} = 80$ V), evidencing hole-doping (see figure 8.3a). Confocal Raman spectroscopy ($\lambda = 633$ nm) provided further evidence for p-doping by the up-shift of the G peak (figure 8.3b), as apparent from comparison with the gate-induced doping measurements in section 5.2. The D-line was only detectable at the edges (see section 2.3), proving the absence of covalent binding of Br atoms to the bulk graphene. In references [186, 187] the p-doping has been attributed to the adsorption of Br_2 molecules on both sides of the graphene monolayer, leading to electron transfer from graphene to the Br_2 acceptor molecules. For the present samples, no additional change between the edge and the bulk region, except the well-known D peak at half frequency of the 2D peak at the edges, could be detected by confocal Raman microscopy. Hence, a microscopic technique offering atomic resolution was needed to explore the edges.

8.4. Scanning tunneling microscopy of Br_2 -treated graphite edges

Scanning tunneling microscopy (STM) operated under ultra-high vacuum (UHV, 10^{-10} mbar) on HOPG substrates exposed to Br_2 vapor under conditions which do not lead to significant swelling (seam formation) at the edges, could not provide edge images with atomic resolution. Only at the terrace center atomic resolution was achievable.

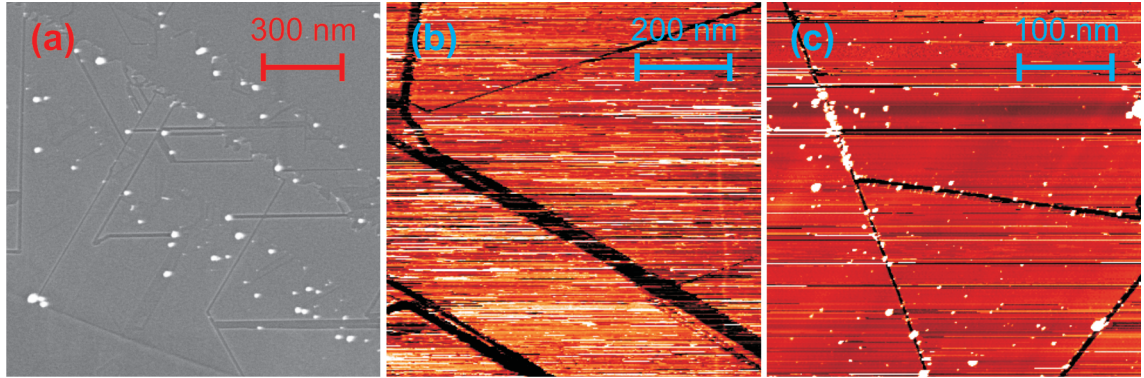


Figure 8.4.: (a) SEM image showing zigzag and armchair edges of nanoparticle etched trenches in HOPG. (b) + (c) STM images recorded at $T = 40$ K under UHV (10^{-10} mbar). [Images taken by R. Preuss, G. Rinke and S. Rauschenbach]

Even lower STM resolution was achieved for oriented graphene edges (zigzag, armchair), obtained by anisotropic etching of HOPG with cobalt nanoparticles (NPs) (10 nm diameter, Strem Chemicals) for 30 min at 850 °C and 1 atm using a flow of 100 sccm forming gas (see figure 8.4).[115, 116] The STM tip picked up contaminations (presumably from the Co NPs). In order to reduce this problems, two approaches were pursued. Firstly, the Co NPs were removed by wet chemical etchants (e.g., diluted HNO_3 , HCl or FeCl_3). This step, however, was not succesful, since residues remained on the HOPG surface. Secondly, the transfer of the Br-treated HOPG sample from the furnace to the STM chamber was conducted under Ar atmosphere, in order to avoid that adsorbates from ambient air would first attach to the Co NPs and then to the tip during the STM scan. However, also in this case no improvement was achieved.

8.5. Transmission electron microscopy of graphene exposed to Br_2

Due to the problems with the STM imaging, transmission electron microscopy (TEM) was used as an alternative microscopy method. For this purpose, samples were prepared by exposing chemical vapor deposition-grown graphene (partially multilayered) on TEM grids (purchased from Graphene Supermarket, USA) to Br_2 vapor. Initially, the grids were cleaned in forming gas at 300 °C for 15 min. During the cooling down the samples were exposed to the Br_2 vapor from 150 °C to 100 °C for 5 min. Atomic resolution could be obtained only far away from the edges at the

center of the sheets (see figure 8.5). While the electron beam itself did not damage the sample at the center, the edges are much more sensitive against the energy impact and can hence not be atomically resolved.[188, 189] Neither adsorption of Br₂ molecules, nor sp³-bonded defects could be detected at the center of the sheets.

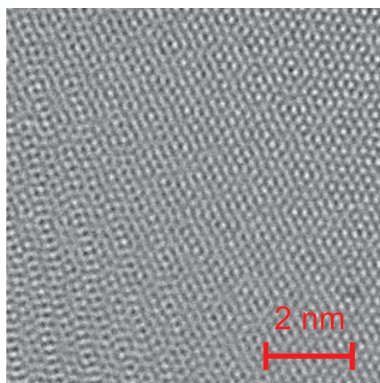


Figure 8.5.: TEM image of the center of a graphene sheet after heating to 300 °C in forming gas, and subsequent exposure to Br₂ vapor during cooling down from 150 °C to 100 °C for 5 min. [Image taken by S. Kurasch]

9. Low temperature transport through graphene nanoribbon quantum dots

This thesis envisioned to demonstrate the effect of chemical edge functionalization of GNRs through changes in the transport properties of graphene nanoribbon quantum dots (GNR QDs). Additionally, recent reports of the Kondo effect at 2 K in GNRs prepared by unzipping carbon nanotubes (CNTs) and mechanical exfoliation motivated a closer examination of GNR QDs at low temperatures.[190, 191] Up to now, reports of magnetic field dependent measurements are missing in the literature, which would allow distinction of Kondo-mediated from other transport mechanisms. The Kondo effect and the conditions to observe it in QDs will be explained in section 9.3. The Kondo effect has already been observed in sp^2 -hybridized carbon nanomaterials such as CNTs at temperatures of up to several Kelvin.[192, 193] Recently, observation of the Kondo effect was claimed in a controversial publication on defective graphene, with Kondo temperatures of up to 90 K.[194, 195, 196]

9.1. Single-electron charging behavior

The low-temperature ($T = 1.4$ K) transport properties of GNR QDs, GNR devices prepared with CdSe NWs as etching mask (see section 4.3) were investigated in a cryostat, that allows applying magnetic fields of up to $B = 12$ T. Figure 9.1 shows the measured drain current I_D in dependence of the gate-source voltage V_{GS} and drain-source voltage V_{DS} of an approximately 20 nm wide and 1.4 μm long GNR. The color code displays current on a logarithmic scale, with the blue area representing the region of suppressed current in the V_{GS} - V_{DS} plane. The occurrence of suppressed current for a limited V_{GS} and V_{DS} range is similar to the behavior of a semiconductor whose Fermi level is located in the bandgap. Such bandgap-like feature is expected for a long GNR, as will be explained below.

By contrast, a series of well distinguishable Coulomb diamonds (CDs) could be observed around the charge neutrality point for GNRs of reduced lengths (see fig-

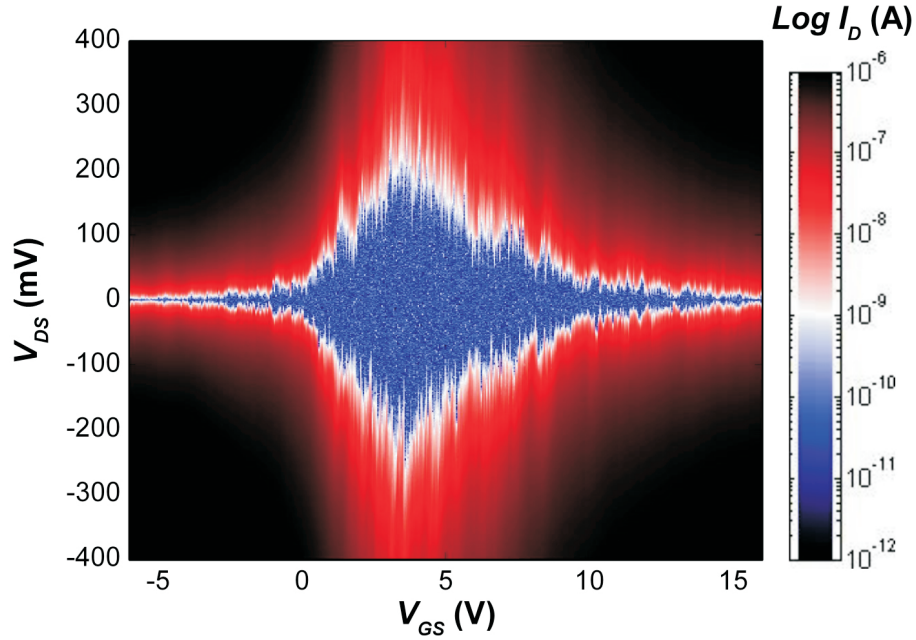


Figure 9.1.: Drain current I_D (on a logarithmic scale) of a ~ 20 nm wide and $1.4 \mu\text{m}$ long GNR as a function of V_{GS} and V_{DS} ($T = 4.2$ K).

ure 9.2a for a ~ 27 nm wide, but only ~ 90 nm long GNR device), which comprise individual QDs.[87, 197] The schematic in figure 9.2b shows a QD, which is coupled by tunnel junctions to metallic electrodes (source and drain), and is capacitively coupled to the gate electrode, which allows to tune the potential on the island.[198] The emergence of CDs can be explained by the energy diagram in figure 9.2c. Current flow is suppressed, when no QD energy level is within the bias window, which is called the Coulomb blockade (CB) effect. Current flow is allowed, when a QD charge state (adjustable by V_{GS}) is within the V_{DS} window. Moreover, CDs are observable only for temperatures lower than the energy required for adding an electron to the island. For the GNR device in figure 9.2a, the size of the CDs is not a periodic function of V_{GS} . Their width in V_{GS} direction (ΔV_{GS}), as well as their height in V_{DS} direction (ΔV_{DS}) varies. The largest charging energies ($E_C = \Delta V_{DS}$) are detected around the Dirac point. Measurements on several GNRs showed, that the maximum charging energy increases with decreasing GNR width, similar to the on/off ratio in GNR devices at room temperature (see section 7.1).[83, 84]

A simple model based on CB in disordered systems is able to explain the observed transport through GNRs by the formation of several QDs along the GNR (see section 2.2). In this model, the drain-source gap is given as $E_C = E_{gap}(W_G) = \frac{\alpha}{W_G} e^{-\beta W_G}$ ($\alpha = 2$ eV nm, $\beta = 0.026$ nm $^{-1}$).[85, 86] A short GNR device most likely consists

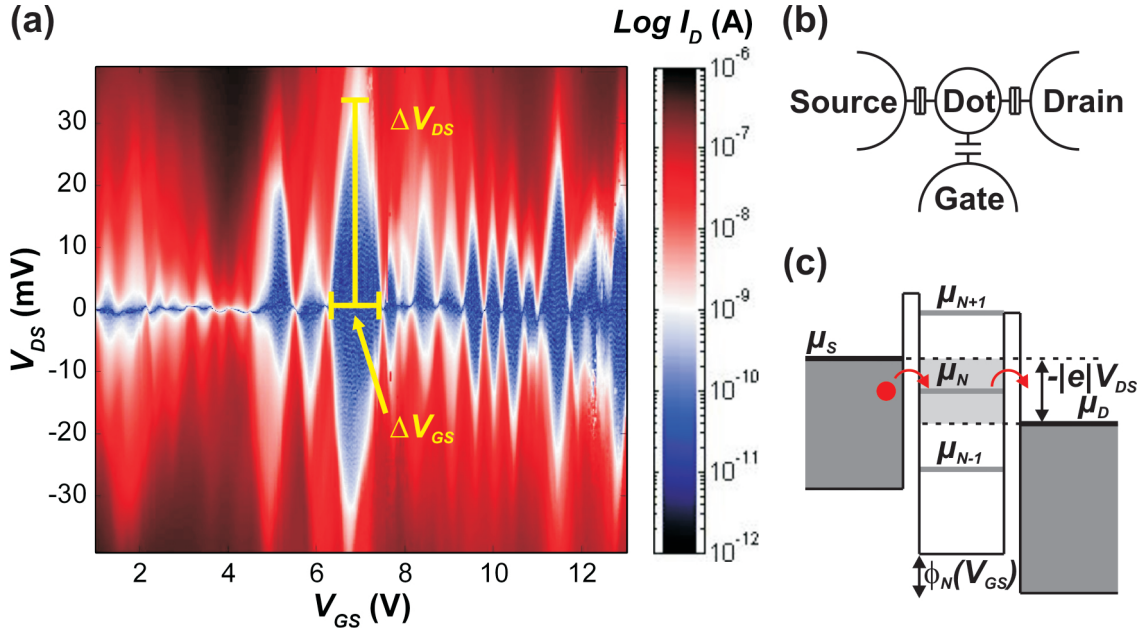


Figure 9.2.: (a) Coulomb diamonds in a ~ 27 nm wide and ~ 90 nm long GNR at $T = 1.4$ K. (b) Sketch of a quantum dot. The QD is coupled by tunnel junctions to metallic electrodes (source and drain), while it is coupled only capacitively to the gate electrode. (c) Illustration of the energy levels in a QD for the situation of current flow.

of only a few QDs or even a single QD, enabling the observation of individual CDs (figure 9.2a). The maximum charging energy of ~ 35 meV for the GNR device in figure 9.2a agrees well with the theoretical values of ~ 37 meV obtained by implementing the width of ~ 27 nm into the above formula.

Transport studies under high magnetic field ($B = 12$ T) applied perpendicular to the graphene plane revealed CDs of reduced size (see figure 9.3a and b). Specifically, the magnetic field was found to compress the CDs (ΔV_{DS} , ΔV_{GS} are smaller), accompanied by an increase in conductance.[197, 199, 200, 201, 202]. This evolution of the CDs with magnetic field is attributable to a convergence of the QD energy levels towards the zero-energy Landau level of graphene.[199]

9.2. Excited states

Lines running parallel to the CD boundaries were observed in direct measurements of the differential conductance dI_D/dV_{DS} using the lock-in technique with a frequency of 1013 Hz and an amplitude in the range of 50-200 μ V (see figure 9.4a). These

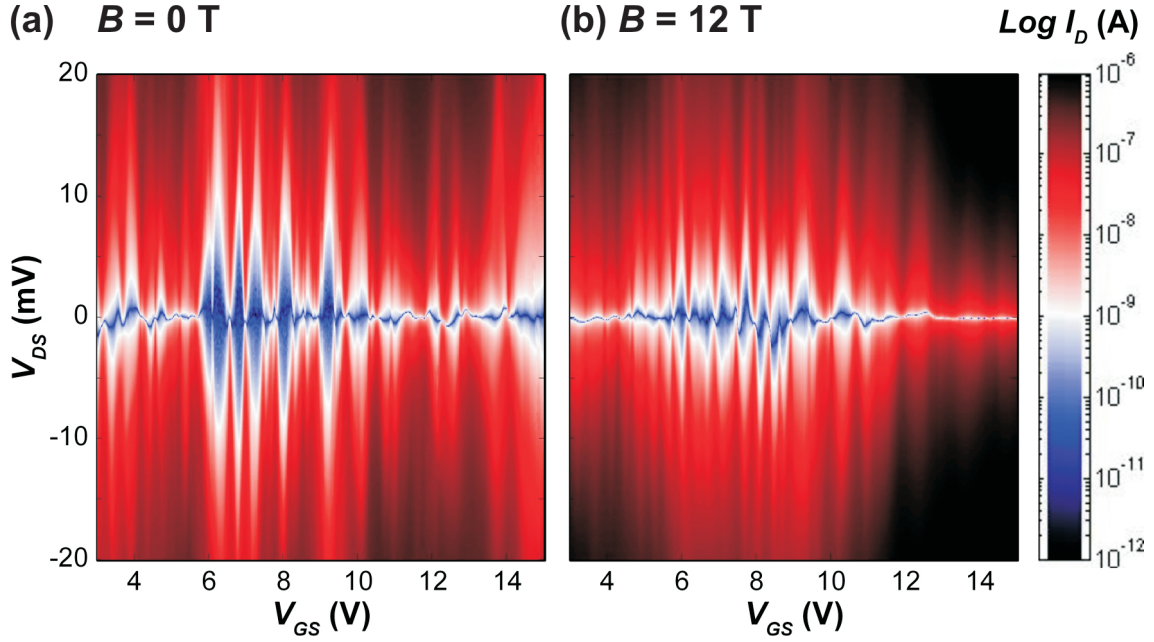


Figure 9.3.: Evolution of Coulomb diamonds with magnetic field in a ~ 28 nm wide and ~ 90 nm long GNR at $T = 1.4$ K. (a) $B = 0$ T, (b) $B = 12$ T.

lines arise from tunneling through excited states of the QD (figure 9.4b).[198] The vertical distance of the lines is a measure for the spacing of quantum confinement energy levels inside the QD. For the present GNRs, excitation energies of the order of several meVs (5-10 meV for the device in figure 9.4a) were derived from the plots.[83, 190, 191, 203, 204, 205]

9.3. Possible Kondo features

In metallic systems, where magnetic moments from impurities couple anti-ferromagnetically to the conduction electrons, spin-flip scattering gives rise to the Kondo effect, comprising an increase in resistivity with decreasing temperature.[206] The maximum temperature up to which this effect occurs is called the Kondo temperature. When a QD is more strongly coupled to the electrodes, current flows not only by sequential resonant tunneling, but also via higher order processes like the Kondo effect or other co-tunneling processes.[198] Figure 9.5a schematically depicts the lowest order co-tunneling process underlying the Kondo effect.[207] A QD with at least one unpaired electron behaves as a magnetic impurity. In this case, electrons are transmitted through a spin-degenerate state of the QD while suffering a spin-flip (represented by red arrows).[207, 208] This enhances the conductance at

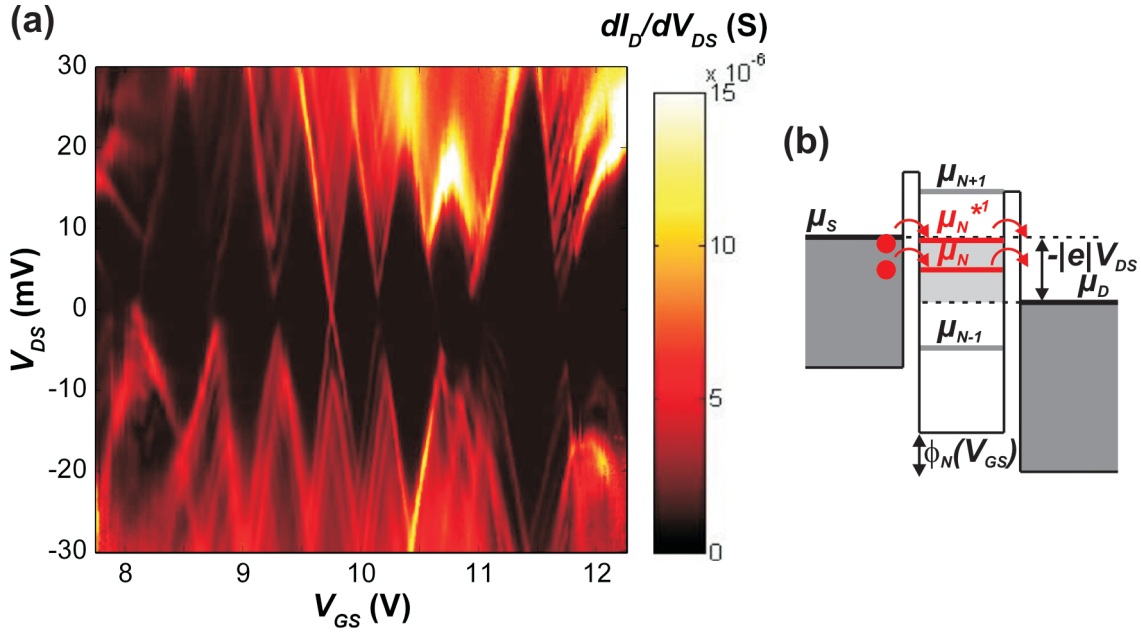


Figure 9.4.: (a) Direct measurement of differential conductance dI_D/dV_{DS} for the device in figure 9.2 measured at $T = 1.4$ K. (b) Energy level scheme of a QD, where current can flow not only via the ground state, but also through an excited state.

zero drain-source voltage, since an additional transport channel becomes available. In general, the observation of the Kondo effect in a QD requires:

- Low temperature: (a) thermal energy must be lower than the charging energy: $k_B T < \frac{e^2}{C}$, C is the capacitance of the QD; (b) lower than the Kondo temperature $T < T_K$. While T cannot be further reduced for the present setup, fulfillment of condition (a) is confirmed by the observation of CDs.
- Tunnel contacts: The electron tunneling rate onto and off the dot, Γ , is a measure for the coupling of the QD to the electrodes. On the one hand tunnel contacts are required for the formation of a QD, while on the other hand sufficient coupling (large Γ) is required to ensure a sizeable T_K ($\Gamma > k_B T_K$). Good coupling leads to smeared CDs, as observed in figure 9.6.
- Small dots: The mean spacing Δ between excited QD sets an upper limit for the coupling Γ . Δ is larger for smaller dots. For the present GNRs, Δ is in the range of several meV (see figure 9.4).

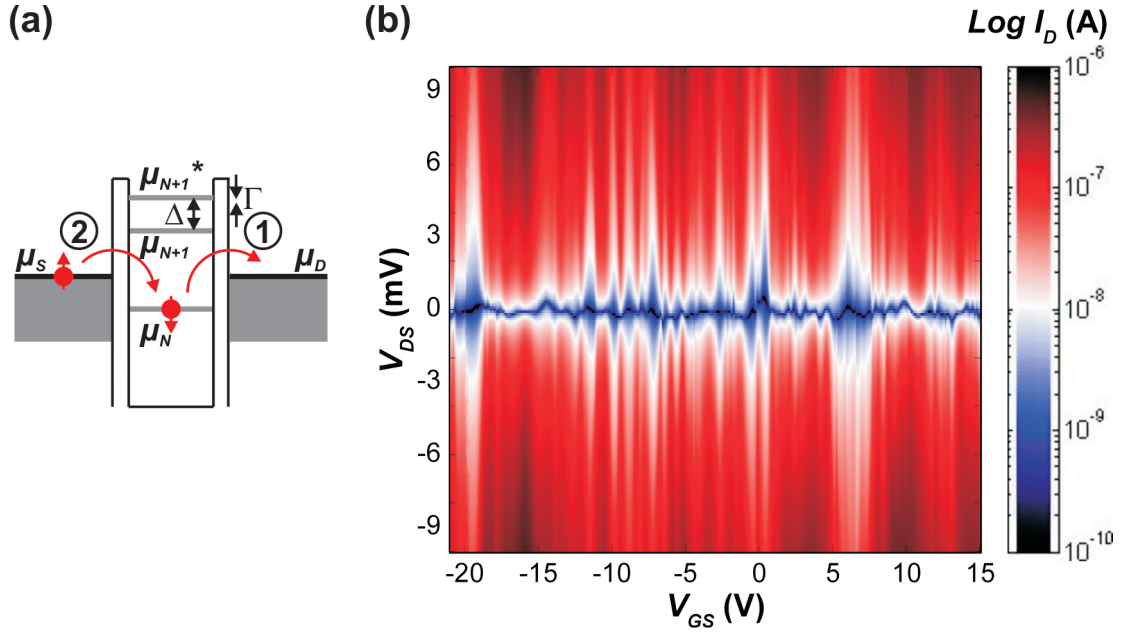


Figure 9.5.: (a) Lowest order co-tunneling process contributing to the Kondo effect. (b) Coulomb diamonds in a ~ 29 nm wide and ~ 35 nm long GNR at $T = 1.4$ K. The scale is different compared to figures 9.1 and 9.2.

Figure 9.5b displays transport data gained from a very short GNR. The distance between the electrodes was decreased below 40 nm. The overall current level was higher compared to longer GNR devices (figures 9.1 and 9.2). Figure 9.6a shows the differential conductance of the same device. The CDs are partially smeared. The observed resistance of the order of $\frac{e^2}{h}$ indicates a good coupling of the metal electrodes.[87, 209] Of particular interest is the conductance increase at $V_{DS} = 0$ mV (e.g. CD at $\sim V_{GS} = 1.1$ V, as marked by the blue arrow in figure 9.6a). This feature could in principle be a signature of the Kondo effect. However, by applying low magnetic fields (up to 3 T) the zero-bias line did not split into two lines that move symmetrically away from $V_{DS} = 0$, as would be expected for the Kondo effect due to Zeeman splitting (see figure 9.6b and c).[208]

In the above experiments, the non-conductive CdSe nanowire was left on top of the GNR, i.e., the electrical contacts were deposited before graphene etching. Hence, the metal electrode is connected through the extended graphene to the GNR (see section 7.1.2). As the graphene between the metal electrode and the GNR is gated, this might decrease the coupling of the GNR QD to the metal electrodes.[208] Therefore, a different contact configuration was implemented by removing the CdSe before contact deposition, allowing for a direct contact between the metal electrodes and

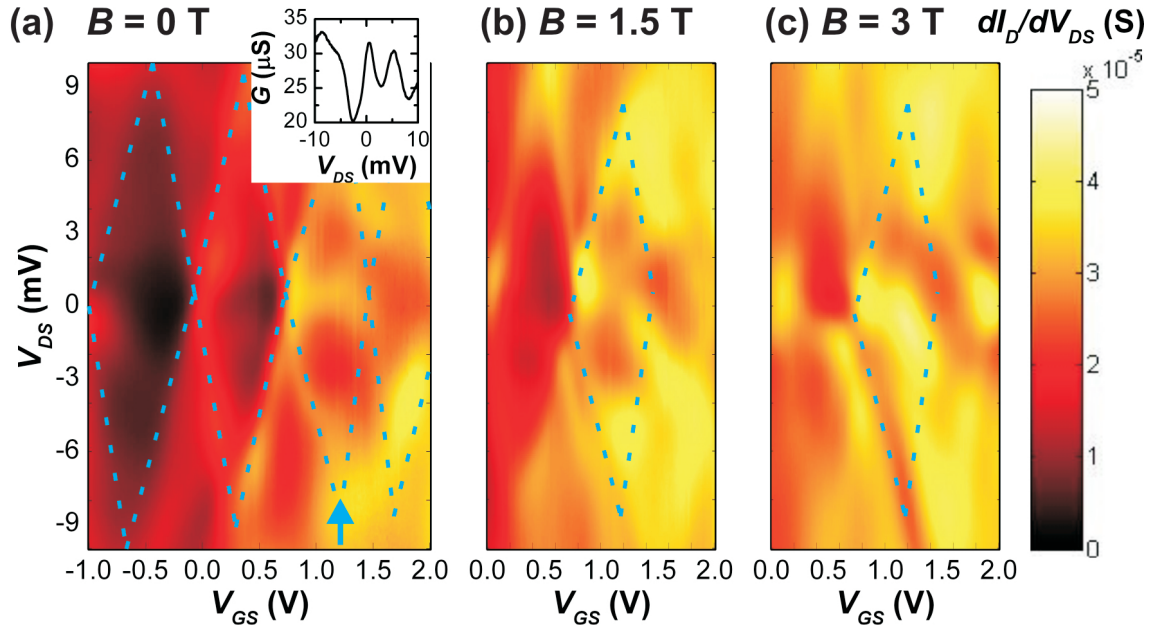


Figure 9.6.: B-field dependent transport measurements of the same device as in figure 9.5. (a) CDs at $B = 0$ T. Inset: G vs. V_{DS} at $V_{GS} = 1.1$ V. (b) $B = 1.5$ T. (c) $B = 3.0$ T.

the GNR. However, devices prepared in this manner still showed the same behavior (in total, 17 GNR devices with varying width and length were characterized). Hence, the observed conductance increase at $V_{DS} = 0$ mV cannot originate from the Kondo effect. The conductance increase around zero bias might instead be explained by co-tunneling without a spin-flip, interference effects, or Fano resonances associated with the presence of several transport channels in the constriction.[83, 209]

9.4. Functionalization of graphene nanoribbons

As already mentioned in chapter 8, the chemical termination of the edges of GNRs can modify the physical properties of GNRs. The following sections present two different functionalization approaches, which were expected to exert an influence on the transport properties of GNR QDs at low temperatures. In both cases, the functionalization was performed directly before loading the sample into the cryostat.

9.4.1. Gas phase approach: Hydrogenation

Room temperature ferromagnetic behavior has been reported for partially hydrogenated epitaxial graphene.[67] The observed ferromagnetism can be explained by

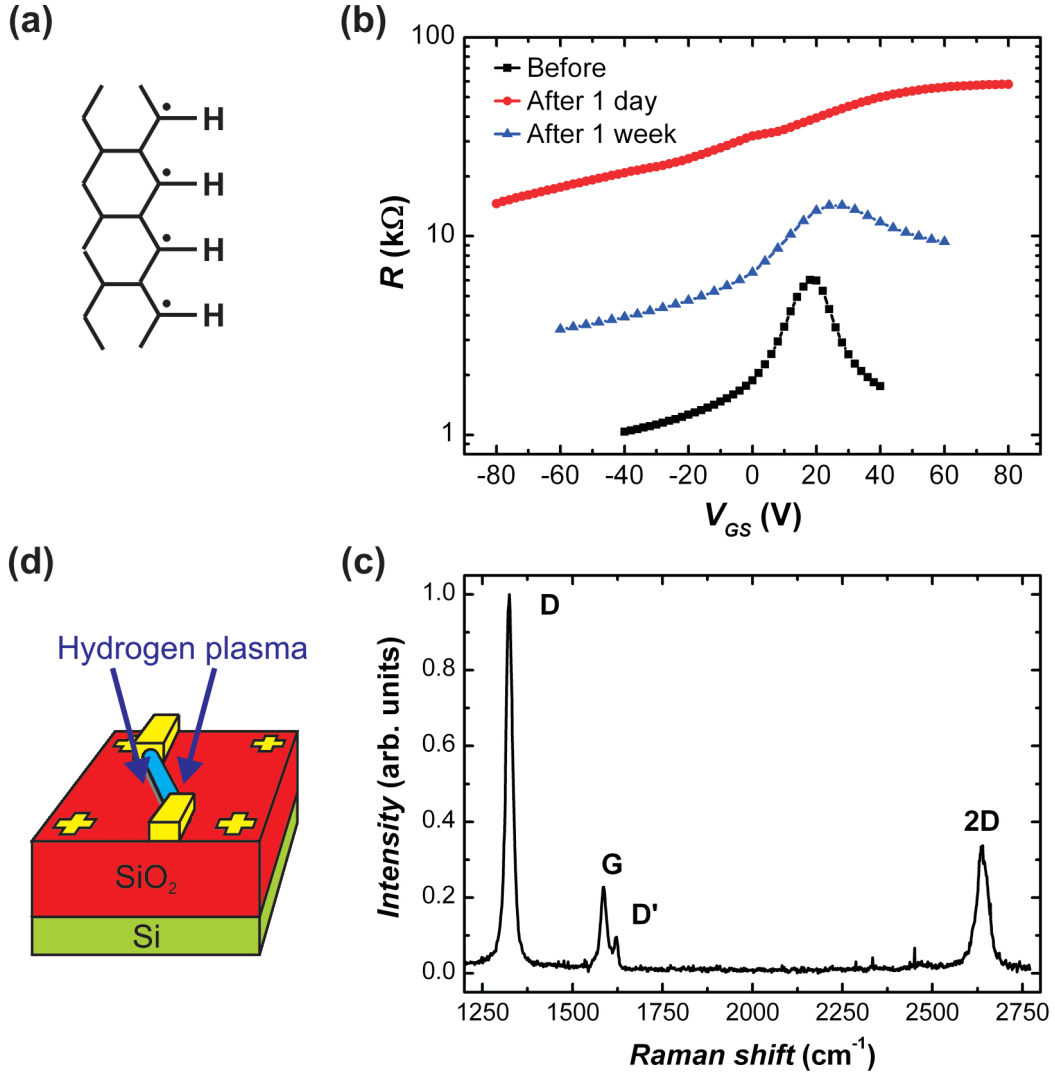


Figure 9.7.: (a) Scheme of a hydrogen-terminated GNR zigzag edge with unpaired electrons. (b) Electrical resistance (on a logarithmic scale) as a function of V_{GS} for a graphene device before hydrogen plasma treatment (black), directly after the treatment (red), and after one week (blue), recorded under ambient condition. (c) Raman spectrum of the same graphene monolayer, taken with 633 nm laser wavelength one week after the hydrogen plasma treatment. (d) Hydrogen plasma was performed on GNR devices with CdSe NW left on top.

unpaired electrons created by (partial) hydrogenation. Hydrogen termination of GNRs has been predicted to be useful for spintronics applications.[68, 69, 70, 71] In this thesis, a hydrogen plasma source (FEMTO plasma, Diener electronic) was used

to functionalize GNR edges with hydrogen atoms (see figure 9.7a). Graphene devices were used to determine the optimal parameters of the plasma (power, pressure, time, position of the sample in the plasma chamber). The sample was placed several centimeters away from the plasma discharge zone in order to minimize damage by energetic ions. A 3 s hydrogen plasma with ~ 45 W power (the plasma does not ignite for lower power levels) and 0.4 mbar pressure was found to leave graphene electrically conductive (see figure 9.7b). Such treatment resulted in heavy p-doping (the position of the Dirac point was higher than $V_{GS} = 80$ V) and a resistance increase by one to two orders of magnitude (from the $k\Omega$ range to several 10 $k\Omega$ s). The strong p-doping has been attributed to adsorbed water in reference [45]. After a few days, the graphene was found to be only slightly p-doped and the resistance had decreased to a constant value (10 $k\Omega$ range), 3-5 times larger than before the plasma treatment. This change may be due to the removal of physisorbed hydrogen molecules (whereas covalently bonded hydrogen atoms remain on the graphene). Raman spectra acquired at this stage display a pronounced D- (1323 cm^{-1}) and D'-line (1621 cm^{-1}), in addition to the G- (1586 cm^{-1}) and 2D-line (2640 cm^{-1}) observed in pristine graphene (see figure 9.7c and section 2.3).

It follows that the hydrogen plasma treatment partially breaks the sp^2 -configuration of the hexagonal graphene lattice under formation of C-H sp^3 bonds.[45] The occurrence of a chemical reaction on the plane strongly suggests that hydrogen treatment etches away originally present edge groups, most probably oxygen-containing functional groups created during the fabrication of the GNRs. According to theory, it is energetically more favourable that carbon edge atoms get bonded to one or two hydrogen atoms before graphene turns into graphane in the bulk.[210] It is advantageous to leave the CdSe nanowire etching mask on top for the hydrogen treatment of GNR devices, as this allows to restrict the reaction to the GNR edges (see figure 9.7d).

The hydrogen plasma treatment left the GNR devices intact. The resistance level was similar to pristine devices and the position of the Dirac point in general was slightly (by several Volts) downshifted, but still in the positive gate-source voltage range. CDs and excited states were similarly observable like for untreated GNRs (see figure 9.8). Measurements under external magnetic B-field showed, that the position and size of CDs depend on the magnetic field. The changes were similar for either positive or negative magnetic fields. No hysteretic behavior was observed. It is concluded, that hydrogen plasma does not introduce a significant spin density, at least for the present hydrogenation conditions.

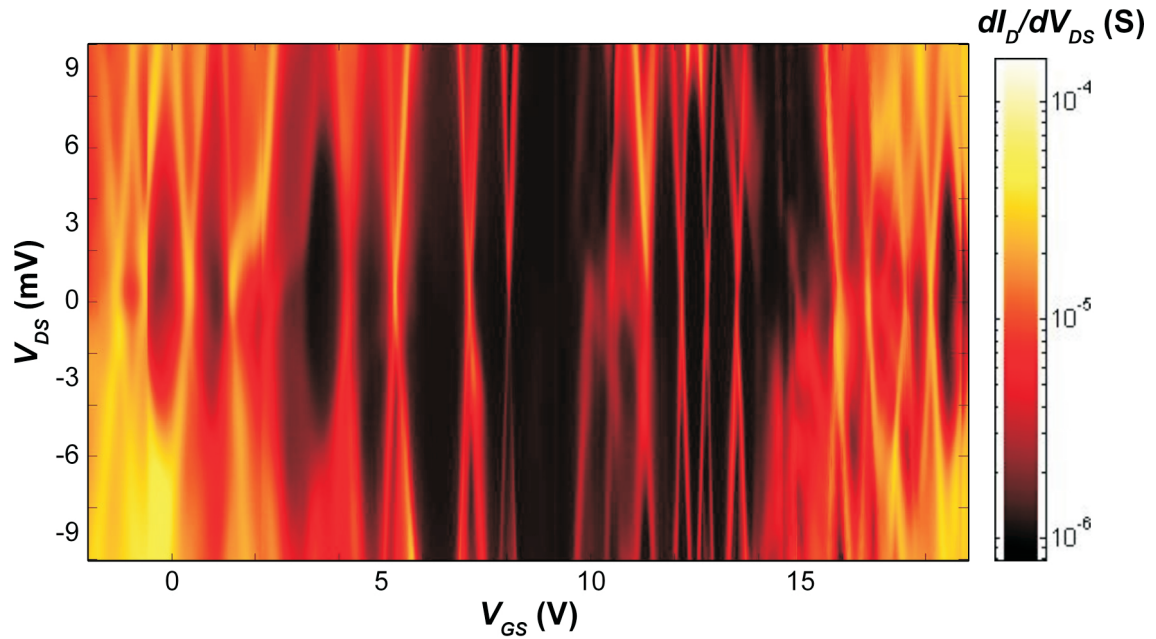


Figure 9.8.: Differential conductance dI_D/dV_{DS} (on a logarithmic scale) for the device in figure 9.5 after hydrogen plasma treatment. The measurement was carried out at $T = 1.4$ K.

9.4.2. Liquid-phase approach: Cobalt ions

As a liquid phase approach for edge functionalization of the GNRs, binding of cobalt (II) ions was attempted. A recent theory study has suggested that Co atoms can be used to engineer the magnetic behavior of the edges of GNRs.[211] In the experiment, a chip with contacted GNRs was immersed in an aqueous solution of 100 mM cobalt acetate (Sigma-Aldrich) for 10 min, followed by rinsing with deionized water and blowing dry. This step was performed with both, CdSe NW left on top or CdSe

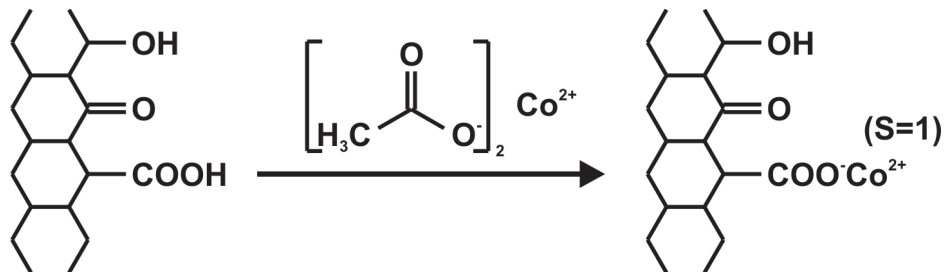


Figure 9.9.: Envisioned edge functionalization via attachment of Co^{2+} ions to carboxylic acid groups at the edge of a GNR.

removed. The envisioned formation of a COOCo group with spin 1 at the edge is schematically illustrated in figure 9.9.

GNRs immersed in Co acetate solution did not show any additional features compared to pristine GNR devices. The resistance level was similar and the position of the Dirac point was in the positive gate-source voltage range. Depending on the GNR dimensions, more or less pronounced CDs were observed (see figure 9.10). Hence, it is concluded, that if a reaction takes place at the GNR edges, the influence of the functional group on the transport properties is negligible.

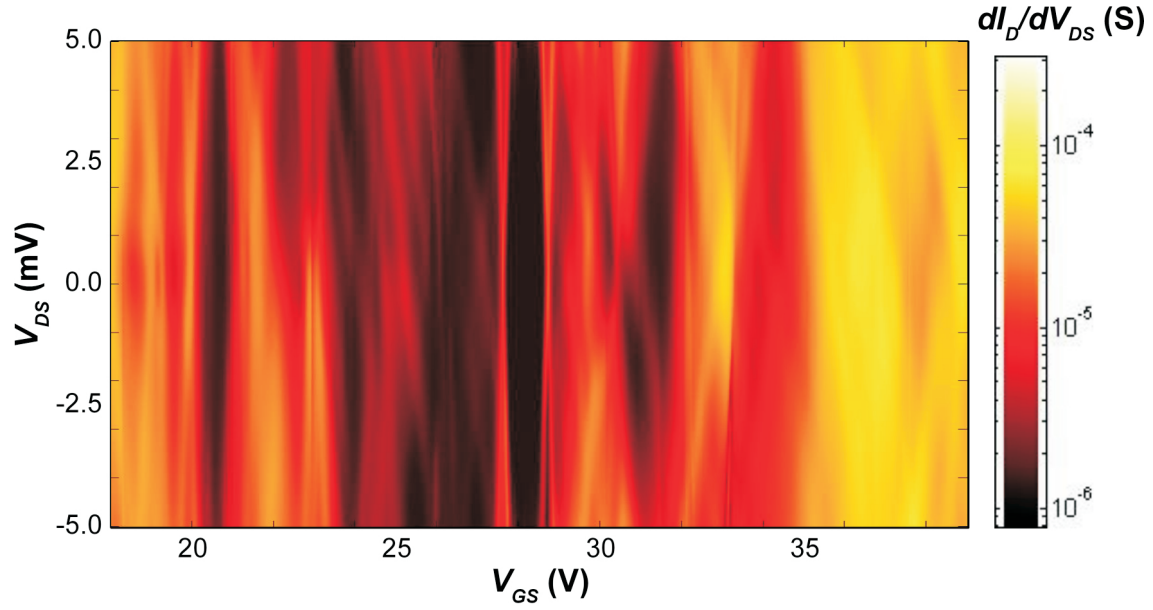


Figure 9.10.: Differential conductance dI_D/dV_{DS} (on a logarithmic scale) of a ~ 29 nm wide and ~ 30 nm long GNR after immersion in an aqueous solution of cobalt acetate. The measurement was performed at $T = 1.4$ K.

10. Summary and outlook

This thesis focused on the fabrication and (opto)electronic properties of graphene nanoribbons (GNRs). The investigated GNRs were prepared by a top-down approach using V_2O_5 nanofibers (NFs) or CdSe nanowires (NWs) as etching mask. The latter type of mask provided access to narrow GNRs of good structural quality, as highlighted by a range of different techniques, most prominently scanning electron microscopy (SEM), transmission electron microscopy (TEM), atomic force microscopy (AFM), scanning tunneling microscopy (STM), as well as Raman spectroscopy. Moreover, electrical transport measurements as a function of temperature revealed that the GNRs comprise a transport gap whose size scales inversely with the ribbon width.

Surface enhanced Raman spectroscopy (SERS) on individual, narrow GNRs (width below 20 nm) was enabled through the attachment of gold nanoparticles. Thus obtained SERS spectra displayed the characteristic features of graphene, including edge-related peaks. On this basis, it could be concluded that the GNRs comprise an electrically inactive edge region with a width below 5 nm. However, no novel features like the theoretically predicted GNR-specific breathing mode could be observed. In complementary experiments, the gate-dependent Raman response of silver nanoparticle-decorated graphene was studied with the aim of unraveling the mechanism underlying the SERS enhancement. The corresponding transfer curves exhibited electron-hole asymmetry similar to graphene modified by the deposition of donor or acceptor molecules.[62] A similar asymmetry could be observed in the Raman spectra, pointing toward the dominance of the electromagnetic vs. chemical enhancement mechanism. It would be interesting to more thoroughly study its origin, in particular to clarify whether it arises from a different electron and hole mobility.[212] This task could be addressed by Hall measurements on such devices.

Furthermore, fast and durable GNR-based memory cells could be realized based upon the hysteresis in the transfer curves of the devices. The hysteresis was found to originate from charge trapping by water molecules in the surrounding of the GNRs and presumably also Si-OH groups on the Si/SiO₂ substrate, in close correspondence to carbon nanotube (CNT) memory devices. Dynamic pulse response measurements demonstrated reliable switching between two conductivity states for

clock frequencies of up to 1 kHz and pulse durations as short as 500 ns for $>10^7$ cycles, outperforming CNT-based memory devices by approximately three orders of magnitude in terms of speed and stability. These characteristics render the GNR devices prospective for application as static random access memories or nonvolatile flash memory cells. The retention time may be further improved through appropriate device encapsulation and the use of non-volatile, specifically tailored charge traps instead of surface water. Even very fast memories with clock frequencies that outperform conventional dynamic random access memories may be accessible by GNRs with lower resistance.

Scanning photocurrent microscopy on GNRs showed pronounced signals in proximity of the metal contacts, with a magnitude linearly proportional to the electrical conductance of the nanoribbons. This behavior was attributed to strong local heating of the GNRs by the laser spot, which leads to the generation of a local voltage source by the photo-thermoelectric Seebeck effect. It was concluded that the heat transport capacity of the GNRs is significantly smaller compared to graphene sheets, a finding which is of relevant for the development of graphene-based optoelectronic devices wherein the geometrical design plays an important role. For future investigations, it would be of interest to bring materials with a high Seebeck coefficient (e.g., a topological insulator like Bi_2Se_3) in contact with graphene or GNRs, which should result in particularly strong photovoltage generation.

Furthermore, it was attempted to chemically functionalize graphene edges with halogen atoms via a gas phase approach. While pronounced doping could be clearly observed after exposure of the samples to bromine vapor at elevated temperature, it was not possible to prove the covalent attachment of bromine atoms to the edges. The principal feasibility of graphene edge functionalization has very recently been documented by TEM images of sulfur atoms linked to the edge of GNRs.[213] It should be emphasized that the successful functionalization in this case could only be achieved due to protective environment provided by the interior of a CNT, which enabled the controlled transformation of chemically substituted fullerenes into nanoribbons. Such conditions are very difficult to attain if the GNRs are necessarily exposed to ambient during e-beam lithography, and accordingly the realization of edge-functionalized GNR devices remains a great future challenge.

Finally, in low temperature transport experiments on 20-30 nm wide GNRs with a small length below 100 nm, well-defined single electron charging behavior could be observed. Specifically, the observation of very regular Coulomb diamonds in some of the devices indicated the presence of only a single quantum dot. The charging energy of the dots was determined to be of the order of a few tens of

meV. Signatures of tunneling through excited states of the quantum dots could also be resolved. Moreover, for GNR devices exhibiting a sizable electronic coupling of the metal contacts, an increased conductance feature around zero source-drain bias emerged. However, upon application of a magnetic field this feature smeared out, but did not show Zeeman splitting as would be expected for the Kondo effect. In addition, only little changes in the transport behavior were observed after treatment of the GNRs by either hydrogen plasma or the (assumed) attachment of cobalt ions to their edges. Future strategies to observe the Kondo effect in GNR devices could involve (i) measurement at further decreased temperature, (ii) better control over the edge structure and crystallographic orientation of the GNRs, in order to minimize the influence of localized edge states, or (iii) use of substrates that introduce less disorder like boron nitride sheets.[24, 204, 214, 215]

A. Appendix: Photocurrent data of graphene nanoribbons

Sample	W_G (nm)	L_G (μm)	On/off ratio	State	I_{Photo} (nA)	R (k Ω)	V_{Photo} (mV)	$I_{Photo}/(W_G \cdot \mu)$ (Jm $^{-3}$)
Ti/Au 1	22	1.5	12	P	1.9	380	0.72	10.5
				N	2.4	580	1.4	21.8
Ti/Au 2	16.5	1.7	16	P	1.4	520	0.73	84.8
				N	-	-	-	-
Ti/Au 3	20	1.65	11	P	1.5	530	0.83	22.7
				N	0.63	3350	2.1	13.7
Ti/Au 4	17	1.85	11	P	0.8	1000	0.8	13.8
				N	0.65	2400	1.6	10.0
Cr/Pd 1	20.5	3.15	13	P	5	130	0.65	8.41
				N	3.2	440	1.4	6.79
Cr/Pd 2	14	1.4	20	P	2.4	320	0.78	34.3
				N	1.1	1550	1.7	23.1
Cr/Pd 3	20	1.4	14	P	7.8	105	0.81	39.0
				N	7.9	270	2.1	39.5

Table A.1.: Photocurrent, resistance, and calculated photovoltage values for a series of GNRs contacted either by 20 nm Ti + 20 nm Au or 2 nm Cr + 40 nm Pd. Measurements were performed at $V_{GS} = -30$ V in the p-type regime, and at $V_{GS} = +30$ V in the n-type regime.

B. Appendix: Abbreviations

- AFM: atomic force microscope
- BLM: breathing-like mode
- CB: Coulomb blockade
- CCD: charge coupled device
- CD: Coulomb diamond
- CM: chemical mechanism
- CNT: carbon nanotube
- CT: charge transfer
- DI: deionized
- DR: double resonance
- EBL: electron-beam lithography
- EM: electromagnetic mechanism
- FET: field-effect transistor
- FWHM: full width at half maximum
- GNR: graphene nanoribbon
- HOPG: highly oriented pyrolytic graphite
- IBE: ion-beam etching
- NF: nanofiber
- NW: nanowire
- NP: nanoparticle

- QD: quantum dot
- RIE: reactive ion etching
- SE: secondary electron
- SEM: scanning electron microscope
- SERS: surface enhanced Raman spectroscopy
- SPCM: scanning photocurrent microscope
- SPR: surface plasmon resonance
- STM: scanning tunneling microscope
- TEM: transmission electron microscope
- TOPO: trioctylphosphine oxide
- UHV: ultra-high vacuum

C. Appendix: Publications

- E. U. Stützel, M. Burghard, K. Kern, F. Traversi, F. Nichele, and R. Sordan. A graphene nanoribbon memory cell. *Small*, 6(24):2822–2825, 2010. doi: 10.1002/smll.201000854.
- E. U. Stützel, T. Dufaux, A. Sagar, S. Rauschenbach, K. Balasubramanian, M. Burghard, and K. Kern. Spatially resolved photocurrents in graphene nanoribbons. *Applied Physics Letters*, 102(4):043106-1-5, 2013.
- C. Cervetti, A. Cornia, F. Luis, E. U. Stützel, S. Rauschenbach, M. Dressel, K. Kern, M. Burghard, and L. Bogani. Surface-dependent assembly and stimuli-driven reorganization in magnetic graphene hybrids. In preparation.

Bibliography

- [1] W. B. Shockley, J. Bardeen, and W. H. Brattain. The Nobel prize in physics 1956.
- [2] R. P. Feynman. There's plenty of room at the bottom. *Journal of Microelectromechanical Systems*, 1(1):60–66, 1992. doi: 10.1109/84.128057.
- [3] E. Ruska, G. Binnig, and H. Rohrer. The Nobel prize in physics 1986.
- [4] C. H. Townes, N. G. Basov, and A. M. Prokhorov. The Nobel prize in physics 1964.
- [5] G. E. Moore. Cramming more components onto integrated circuits (reprinted from electronics, 1965). *Proceedings of the IEEE*, 86(1):82–85, 1998. doi: 10.1109/jproc.1998.658762.
- [6] R. B. Laughlin, H. L. Störmer, and D. C. Tsui. The Nobel prize in physics 1998.
- [7] Z. I. Alferov, H. Krömer, and J. S. Kilby. The Nobel prize in physics 2000.
- [8] Bell Labs. *alcatel-lucent.com*.
- [9] A. K. Geim and K. S. Novoselov. The Nobel prize in physics 2010.
- [10] H. P. Boehm, A. Clauss, G. O. Fischer, and U. Hofmann. Dünnsche Kohlenstoff-Folien. *Zeitschrift für Naturforschung*, 17b:150–153, 1962.
- [11] K. S. Novoselov, A. K. Geim, S. V. Morozov, D. Jiang, Y. Zhang, S. V. Dubonos, I. V. Grigorieva, and A. A. Firsov. Electric field effect in atomically thin carbon films. *Science*, 306(5696):666–669, 2004. doi: 10.1126/science.1102896.
- [12] R. E. Peierls. Quelques proprietes typiques des corps solides. *Ann. Inst. Henri Poincare*, 5:177–222, 1935.
- [13] L. D. Landau. Zur Theorie der Phasenumwandlungen II. *Phys. Z. Sowjetunion*, 11:26–35, 1937.

- [14] L. D. Landau and E. M. Lifshitz. *Statistical physics, part I*. Pergamon, Oxford, 1980.
- [15] N. D. Mermin. Crystalline order in two dimensions. *Physical Review*, 176(1):250–254, 1968. doi: 10.1103/physrev.176.250.
- [16] J. C. Meyer, A. K. Geim, M. I. Katsnelson, K. S. Novoselov, T. J. Booth, and S. Roth. The structure of suspended graphene sheets. *Nature*, 446(7131):60–63, 2007. doi: 10.1038/nature05545.
- [17] A. K. Geim and K. S. Novoselov. The rise of graphene. *Nature Materials*, 6(3):183–191, 2007. doi: 10.1038/nmat1849.
- [18] A. H. Castro Neto, F. Guinea, N. M. R. Peres, K. S. Novoselov, and A. K. Geim. The electronic properties of graphene. *Reviews of Modern Physics*, 81(1):109–162, 2009. doi: 10.1103/revmodphys.81.109.
- [19] M. I. Katsnelson, K. S. Novoselov, and A. K. Geim. Chiral tunnelling and the Klein paradox in graphene. *Nature Physics*, 2(9):620–625, 2006. doi: 10.1038/nphys384.
- [20] N. Stander, B. Huard, and D. Goldhaber-Gordon. Evidence for Klein tunneling in graphene p-n junctions. *Physical Review Letters*, 102(2):026807–1–4, 2009. doi: 10.1103/physrevlett.102.026807.
- [21] A. H. Castro Neto and K. S. Novoselov. New directions in science and technology: two-dimensional crystals. *Reports on Progress in Physics*, 74(8):082501–1–9, 2011. doi: 10.1088/0034-4885/74/8/082501.
- [22] L. Britnell, R. V. Gorbachev, R. Jalil, B. D. Belle, F. Schedin, A. Mishchenko, T. Georgiou, M. I. Katsnelson, L. Eaves, S. V. Morozov, N. M. R. Peres, J. Leist, A. K. Geim, K. S. Novoselov, and L. A. Ponomarenko. Field-effect tunneling transistor based on vertical graphene heterostructures. *Science*, 335(6071):947–950, 2012. doi: 10.1126/science.1218461.
- [23] K. S. Novoselov, V. I. Fal’ko, L. Colombo, P. R. Gellert, M. G. Schwab, and K. Kim. A roadmap for graphene. *Nature*, 490(7419):192–200, 2012. doi: 10.1038/nature11458.
- [24] C. R. Dean, A. F. Young, I. Meric, C. Lee, L. Wang, S. Sorgenfrei, K. Watanabe, T. Taniguchi, P. Kim, K. L. Shepard, and J. Hone. Boron nitride substrates for high-quality graphene electronics. *Nature Nanotechnology*, 5(10):722–726, 2010. doi: 10.1038/nnano.2010.172.

-
- [25] K. Balasubramanian, E. J. H. Lee, R. T. Weitz, M. Burghard, and K. Kern. Carbon nanotube transistors - chemical functionalization and device characterization. *Physica Status Solidi A*, 205(3):633–646, 2008. doi: 10.1002/pssa.200723410.
- [26] K. I. Bolotin, K. J. Sikes, Z. Jiang, M. Klima, G. Fudenberg, J. Hone, P. Kim, and H. L. Störmer. Ultrahigh electron mobility in suspended graphene. *Solid State Communications*, 146(9-10):351–355, 2008. doi: 10.1016/j.ssc.2008.02.024.
- [27] X. Du, I. Skachko, A. Barker, and E. Y. Andrei. Approaching ballistic transport in suspended graphene. *Nature Nanotechnology*, 3(8):491–495, 2008. doi: 10.1038/nnano.2008.199.
- [28] X. Hong, A. Posadas, K. Zou, C. H. Ahn, and J. Zhu. High-mobility few-layer graphene field effect transistors fabricated on epitaxial ferroelectric gate oxides. *Physical Review Letters*, 102(13):136808–1–4, 2009. doi: 10.1103/physrevlett.102.136808.
- [29] F. Schwierz. Graphene transistors. *Nature Nanotechnology*, 5(7):487–496, 2010. doi: 10.1038/nnano.2010.89.
- [30] H. Wang, D. Nezich, J. Kong, and T. Palacios. Graphene frequency multipliers. *IEEE Electron Device Letters*, 30(5):547–549, 2009. doi: 10.1109/led.2009.2016443.
- [31] R. Sordan, F. Traversi, and V. Russo. Logic gates with a single graphene transistor. *Applied Physics Letters*, 94(7):073305–1–3, 2009. doi: 10.1063/1.3079663.
- [32] F. Traversi, V. Russo, and R. Sordan. Integrated complementary graphene inverter. *Applied Physics Letters*, 94(22):223312–1–3, 2009. doi: 10.1063/1.3148342.
- [33] N. Harada, K. Yagi, S. Sato, and N. Yokoyama. A polarity-controllable graphene inverter. *Applied Physics Letters*, 96(1):012102–1–3, 2010. doi: 10.1063/1.3280042.
- [34] L. G. Rizzi, M. Bianchi, A. Behnam, E. Carrion, E. Guerriero, L. Polloni, E. Pop, and R. Sordan. Cascading wafer-scale integrated graphene complementary inverters under ambient conditions. *Nano Letters*, 12(8):3948–3953, 2012. doi: 10.1021/nl301079r.

- [35] X. Wang, L. Zhi, and K. Müllen. Transparent, conductive graphene electrodes for dye-sensitized solar cells. *Nano Letters*, 8(1):323–327, 2008. doi: 10.1021/nl072838r.
- [36] N. Savage. Come into the light. *Nature*, 483(7389):S38–S39, 2012. doi: 10.1038/483S38a.
- [37] J. D. Meindl, Q. Chen, and J. A. Davis. Limits on silicon nanoelectronics for terascale integration. *Science*, 293(5537):2044–2049, 2001. doi: 10.1126/science.293.5537.2044.
- [38] C. Lee, X. Wei, J. W. Kysar, and J. Hone. Measurement of the elastic properties and intrinsic strength of monolayer graphene. *Science*, 321(5887):385–388, 2008. doi: 10.1126/science.1157996.
- [39] S. Bae, H. Kim, Y. Lee, X. Xu, J.-S. Park, Y. Zheng, J. Balakrishnan, T. Lei, H. R. Kim, Y. I. Song, Y.-J. Kim, K. S. Kim, B. Özyilmaz, J.-H. Ahn, B. H. Hong, and S. Iijima. Roll-to-roll production of 30-inch graphene films for transparent electrodes. *Nature Nanotechnology*, 5(8):574–578, 2010. doi: 10.1038/nnano.2010.132.
- [40] F. Schedin, A. K. Geim, S. V. Morozov, E. W. Hill, P. Blake, M. I. Katsnelson, and K. S. Novoselov. Detection of individual gas molecules adsorbed on graphene. *Nature Materials*, 6(9):652–655, 2007. doi: 10.1038/nmat1967.
- [41] Y. Shao, J. Wang, H. Wu, J. Liu, I. A. Aksay, and Y. Lin. Graphene based electrochemical sensors and biosensors: a review. *Electroanalysis*, 22(10):1027–1036, 2010. doi: 10.1002/elan.200900571.
- [42] C. Gomez-Navarro, R. T. Weitz, A. M. Bittner, M. Scolari, A. Mews, M. Burghard, and K. Kern. Electronic transport properties of individual chemically reduced graphene oxide sheets. *Nano Letters*, 7(11):3499–3503, 2007. doi: 10.1021/nl072090c.
- [43] C. Berger, Z. Song, X. Li, X. Wu, N. Brown, C. Naud, D. Mayou, T. Li, J. Hass, A. N. Marchenkov, E. H. Conrad, P. N. First, and W. A. de Heer. Electronic confinement and coherence in patterned epitaxial graphene. *Science*, 312(5777):1191–1196, 2006. doi: 10.1126/science.1125925.
- [44] K. S. Kim, Y. Zhao, H. Jang, S. Y. Lee, J. M. Kim, K. S. Kim, J.-H. Ahn, P. Kim, J.-Y. Choi, and B. H. Hong. Large-scale pattern growth of graphene films for stretchable transparent electrodes. *Nature*, 457(7230):706–710, 2009. doi: 10.1038/nature07719.

-
- [45] D. C. Elias, R. R. Nair, T. M. G. Mohiuddin, S. V. Morozov, P. Blake, M. P. Halsall, A. C. Ferrari, D. W. Boukhvalov, M. I. Katsnelson, A. K. Geim, and K. S. Novoselov. Control of graphene's properties by reversible hydrogenation: evidence for graphane. *Science*, 323(5914):610–613, 2009. doi: 10.1126/science.1167130.
- [46] J. B. Oostinga, H. B. Heersche, X. Liu, A. F. Morpurgo, and L. M. K. Vandersypen. Gate-induced insulating state in bilayer graphene devices. *Nature Materials*, 7(2):151–157, 2008. doi: 10.1038/nmat2082.
- [47] Y. Zhang, T.-T. Tang, C. Girit, Z. Hao, M. C. Martin, A. Zettl, M. F. Crommie, Y. R. Shen, and F. Wang. Direct observation of a widely tunable bandgap in bilayer graphene. *Nature*, 459(7248):820–823, 2009. doi: 10.1038/nature08105.
- [48] V. Barone, O. Hod, and G. E. Scuseria. Electronic structure and stability of semiconducting graphene nanoribbons. *Nano Letters*, 6(12):2748–2754, 2006. doi: 10.1021/nl0617033.
- [49] D. A. Areshkin, D. Gunlycke, and C. T. White. Ballistic transport in graphene nanostrips in the presence of disorder: importance of edge effects. *Nano Letters*, 7(1):204–210, 2007. doi: 10.1021/nl062132h.
- [50] J. Fernandez-Rossier and J. J. Palacios. Magnetism in graphene nanoislands. *Physical Review Letters*, 99(17):177204–1–4, 2007. doi: 10.1103/physrevlett.99.177204.
- [51] O. V. Yazyev and M. I. Katsnelson. Magnetic correlations at graphene edges: basis for novel spintronics devices. *Physical Review Letters*, 100(4):047209–1–4, 2008. doi: 10.1103/physrevlett.100.047209.
- [52] F. Cervantes-Sodi, G. Csanyi, S. Piscanec, and A. C. Ferrari. Edge-functionalized and substitutionally doped graphene nanoribbons: electronic and spin properties. *Physical Review B*, 77(16):165427–1–13, 2008. doi: 10.1103/physrevb.77.165427.
- [53] P. Koskinen, S. Malola, and H. Häkkinen. Self-passivating edge reconstructions of graphene. *Physical Review Letters*, 101(11):115502–1–4, 2008. doi: 10.1103/physrevlett.101.115502.
- [54] V. B. Shenoy, C. D. Reddy, A. Ramasubramaniam, and Y. W. Zhang. Edge-stress-induced warping of graphene sheets and nanoribbons. *Physical Review Letters*, 101(24):245501–1–4, 2008. doi: 10.1103/physrevlett.101.245501.

- [55] Z. F. Wang, Q. Li, H. Zheng, H. Ren, H. Su, Q. W. Shi, and J. Chen. Tuning the electronic structure of graphene nanoribbons through chemical edge modification: a theoretical study. *Physical Review B*, 75(11):113406–1–4, 2007. doi: 10.1103/physrevb.75.113406.
- [56] H. Zheng and W. Duley. First-principles study of edge chemical modifications in graphene nanodots. *Physical Review B*, 78(4):045421–1–5, 2008. doi: 10.1103/physrevb.78.045421.
- [57] B. Trauzettel, D. V. Bulaev, D. Loss, and G. Burkard. Spin qubits in graphene quantum dots. *Nature Physics*, 3(3):192–196, 2007. doi: 10.1038/nphys544.
- [58] D. W. Boukhvalov and M. I. Katsnelson. Chemical functionalization of graphene with defects. *Nano Letters*, 8(12):4373–4379, 2008. doi: 10.1021/nl802234n.
- [59] Y.-W. Son, M. L. Cohen, and S. G. Louie. Half-metallic graphene nanoribbons. *Nature*, 444(7117):347–349, 2006. doi: 10.1038/nature05180.
- [60] N. Tombros, C. Jozsa, M. Popinciuc, H. T. Jonkman, and B. J. van Wees. Electronic spin transport and spin precession in single graphene layers at room temperature. *Nature*, 448(7153):571–574, 2007. doi: 10.1038/nature06037.
- [61] W. Chen, S. Chen, D. C. Qi, X. Y. Gao, and A. T. S. Wee. Surface transfer p-type doping of epitaxial graphene. *Journal of the American Chemical Society*, 129(34):10418–10422, 2007. doi: 10.1021/ja071658g.
- [62] D. B. Farmer, R. Golizadeh-Mojarad, V. Perebeinos, Y.-M. Lin, G. S. Tulevski, J. C. Tsang, and P. Avouris. Chemical doping and electron-hole conduction asymmetry in graphene devices. *Nano Letters*, 9(1):388–392, 2009. doi: 10.1021/nl803214a.
- [63] K. Balasubramanian, T. Kurkina, A. Ahmad, M. Burghard, and K. Kern. Tuning the functional interface of carbon nanotubes by electrochemistry: toward nanoscale chemical sensors and biosensors. *Journal of Materials Research*, 27(2):391–402, 2012. doi: 10.1557/jmr.2011.410.
- [64] J. H. Chen, C. Jang, S. Adam, M. S. Fuhrer, E. D. Williams, and M. Ishigami. Charged-impurity scattering in graphene. *Nature Physics*, 4(5):377–381, 2008. doi: 10.1038/nphys935.
- [65] M. Y. Han, B. Özyilmaz, Y. Zhang, and P. Kim. Energy band-gap engineering of graphene nanoribbons. *Physical Review Letters*, 98(20):206805–1–4, 2007. doi: 10.1103/physrevlett.98.206805.

-
- [66] Z. Chen, Y.-M. Lin, M. J. Rooks, and P. Avouris. Graphene nano-ribbon electronics. *Physica E*, 40(2):228–232, 2007. doi: 10.1016/j.physe.2007.06.020.
- [67] L. Xie, X. Wang, J. Lu, Z. Ni, Z. Luo, H. Mao, R. Wang, Y. Wang, H. Huang, D. Qi, R. Liu, T. Yu, Z. Shen, T. Wu, H. Peng, B. Özyilmaz, K. Loh, A. T. S. Wee, Ariando, and W. Chen. Room temperature ferromagnetism in partially hydrogenated epitaxial graphene. *Applied Physics Letters*, 98(19):193113–1–3, 2011. doi: 10.1063/1.3589970.
- [68] G. Cantele, Y.-S. Lee, D. Ninno, and N. Marzari. Spin channels in functionalized graphene nanoribbons. *Nano Letters*, 9(10):3425–3429, 2009. doi: 10.1021/nl901557x.
- [69] S. Bhandary, O. Eriksson, B. Sanyal, and M. I. Katsnelson. Complex edge effects in zigzag graphene nanoribbons due to hydrogen loading. *Physical Review B*, 82(16):165405–1–7, 2010. doi: 10.1103/physrevb.82.165405.
- [70] X.-F. Li, L.-L. Wang, K.-Q. Chen, and Y. Luo. Strong current polarization and negative differential resistance in chiral graphene nanoribbons with reconstructed (2,1)-edges. *Applied Physics Letters*, 101(7):073101–1–5, 2012. doi: 10.1063/1.4745506.
- [71] X. H. Zheng, X. L. Wang, L. F. Huang, H. Hao, J. Lan, and Z. Zeng. Stabilizing the ground state in zigzag-edged graphene nanoribbons by dihydrogenation. *Physical Review B*, 86(8):081408–1–5, 2012. doi: 10.1103/physrevb.86.081408.
- [72] H. W. Kroto, J. R. Heath, S. C. O'Brien, R. F. Curl, and R. E. Smalley. C₆₀: Buckminsterfullerene. *Nature*, 318(6042):162–163, 1985. doi: 10.1038/318162a0.
- [73] S. Iijima and T. Ichihashi. Single-shell carbon nanotubes of 1-nm diameter. *Nature*, 363(6430):603–605, 1993. doi: 10.1038/363603a0.
- [74] D. S. Bethune, C. H. Kiang, M. S. Devries, G. Gorman, R. Savoy, J. Vazquez, and R. Beyers. Cobalt-catalysed growth of carbon nanotubes with single-atomic-layer walls. *Nature*, 363(6430):605–607, 1993. doi: 10.1038/363605a0.
- [75] H. Kataura, Y. Kumazawa, Y. Maniwa, I. Umez, S. Suzuki, Y. Ohtsuka, and Y. Achiba. Optical properties of single-wall carbon nanotubes. *Synthetic Metals*, 103(1-3):2555–2558, 1999. doi: 10.1016/S0379-6779(98)00278-1.
- [76] M. Fujita, K. Wakabayashi, K. Nakada, and K. Kusakabe. Peculiar localized state at zigzag graphite edge. *Journal of the Physical Society of Japan*, 65(7):1920–1923, 1996. doi: 10.1143/jpsj.65.1920.

- [77] K. Nakada, M. Fujita, G. Dresselhaus, and M. S. Dresselhaus. Edge state in graphene ribbons: nanometer size effect and edge shape dependence. *Physical Review B*, 54(24):17954–17961, 1996. doi: 10.1103/physrevb.54.17954.
- [78] P. R. Wallace. The band theory of graphite. *Physical Review*, 71(9):622–634, 1947. doi: 10.1103/physrev.71.622.
- [79] K. S. Novoselov, A. K. Geim, S. V. Morozov, D. Jiang, M. I. Katsnelson, I. V. Grigorieva, S. V. Dubonos, and A. A. Firsov. Two-dimensional gas of massless Dirac fermions in graphene. *Nature*, 438(7065):197–200, 2005. doi: 10.1038/nature04233.
- [80] Y. B. Zhang, Y. W. Tan, H. L. Störmer, and P. Kim. Experimental observation of the quantum Hall effect and Berry’s phase in graphene. *Nature*, 438(7065):201–204, 2005. doi: 10.1038/nature04235.
- [81] J. Martin, N. Akerman, G. Ulbricht, T. Lohmann, J. H. Smet, K. von Klitzing, and A. Yacoby. Observation of electron-hole puddles in graphene using a scanning single-electron transistor. *Nature Physics*, 4(2):144–148, 2008. doi: 10.1038/nphys781.
- [82] Y.-W. Son, M. L. Cohen, and S. G. Louie. Energy gaps in graphene nanoribbons. *Physical Review Letters*, 97(21):216803–1–4, 2006. doi: 10.1103/physrevlett.97.216803.
- [83] K. Todd, H.-T. Chou, S. Amasha, and D. Goldhaber-Gordon. Quantum dot behavior in graphene nanoconstrictions. *Nano Letters*, 9(1):416–421, 2009. doi: 10.1021/nl803291b.
- [84] C. Stampfer, J. Güttinger, S. Hellmüller, F. Molitor, K. Ensslin, and T. Ihn. Energy gaps in etched graphene nanoribbons. *Physical Review Letters*, 102(5):056403–1–4, 2009. doi: 10.1103/physrevlett.102.056403.
- [85] F. Sols, F. Guinea, and A. H. Castro Neto. Coulomb blockade in graphene nanoribbons. *Physical Review Letters*, 99(16):166803–1–4, 2007. doi: 10.1103/physrevlett.99.166803.
- [86] F. Molitor, C. Stampfer, J. Güttinger, A. Jacobsen, T. Ihn, and K. Ensslin. Energy and transport gaps in etched graphene nanoribbons. *Semiconductor Science and Technology*, 25(3):034002–1–7, 2010. doi: 10.1088/0268-1242/25/3/034002.

-
- [87] P. Gallagher, K. Todd, and D. Goldhaber-Gordon. Disorder-induced gap behavior in graphene nanoribbons. *Physical Review B*, 81(11):115409–1–8, 2010. doi: 10.1103/physrevb.81.115409.
- [88] A. C. Ferrari, J. C. Meyer, V. Scardaci, C. Casiraghi, M. Lazzeri, F. Mauri, S. Piscanec, D. Jiang, K. S. Novoselov, S. Roth, and A. K. Geim. Raman spectrum of graphene and graphene layers. *Physical Review Letters*, 97(18):187401–1–4, 2006. doi: 10.1103/physrevlett.97.187401.
- [89] D. Graf, F. Molitor, K. Ensslin, C. Stampfer, A. Jungen, C. Hierold, and L. Wirtz. Spatially resolved raman spectroscopy of single- and few-layer graphene. *Nano Letters*, 7(2):238–242, 2007. doi: 10.1021/nl061702a.
- [90] S. Pisana, M. Lazzeri, C. Casiraghi, K. S. Novoselov, A. K. Geim, A. C. Ferrari, and F. Mauri. Breakdown of the adiabatic Born-Oppenheimer approximation in graphene. *Nature Materials*, 6(3):198–201, 2007. doi: 10.1038/nmat1846.
- [91] A. C. Ferrari. Raman spectroscopy of graphene and graphite: disorder, electron-phonon coupling, doping and nonadiabatic effects. *Solid State Communications*, 143(1-2):47–57, 2007. doi: 10.1016/j.ssc.2007.03.052.
- [92] C. Stampfer, F. Molitor, D. Graf, K. Ensslin, A. Jungen, C. Hierold, and L. Wirtz. Raman imaging of doping domains in graphene on SiO₂. *Applied Physics Letters*, 91(24):241907–1–3, 2007. doi: 10.1063/1.2816262.
- [93] F. Tuinstra and J. L. Koenig. Raman spectrum of graphite. *Journal of Chemical Physics*, 53(3):1126–1130, 1970. doi: 10.1063/1.1674108.
- [94] L. M. Malard, M. A. Pimenta, G. Dresselhaus, and M. S. Dresselhaus. Raman spectroscopy in graphene. *Physics Reports*, 473(5-6):51–87, 2009. doi: 10.1016/j.physrep.2009.02.003.
- [95] M. Lazzeri, C. Attaccalite, L. Wirtz, and F. Mauri. Impact of the electron-electron correlation on phonon dispersion: failure of LDA and GGA DFT functionals in graphene and graphite. *Physical Review B*, 78(8):081406–1–4, 2008. doi: 10.1103/physrevb.78.081406.
- [96] A. C. Ferrari and J. Robertson. Interpretation of Raman spectra of disordered and amorphous carbon. *Physical Review B*, 61(20):14095–14107, 2000. doi: 10.1103/physrevb.61.14095.
- [97] C. Thomsen and S. Reich. Double resonant Raman scattering in graphite. *Physical Review Letters*, 85(24):5214–5217, 2000. doi: 10.1103/physrevlett.85.5214.

- [98] R. J. Nemanich and S. A. Solin. First- and second-order Raman scattering from finite-size crystals of graphite. *Physical Review B*, 20(2):392–401, 1979. doi: 10.1103/physrevb.20.392.
- [99] M. Fleischmann, P. J. Hendra, and A. J. McQuilla. Raman-spectra of pyridine adsorbed at a silver electrode. *Chemical Physics Letters*, 26(2):163–166, 1974. doi: 10.1016/0009-2614(74)85388-1.
- [100] D. L. Jeanmarie and R. P. Van Duyne. Surface raman spectroelectrochemistry: part I. heterocyclic, aromatic, and aliphatic amines adsorbed on the anodized silver electrode. *Journal of Electroanalytical Chemistry*, 84(1):1–20, 1977. doi: 10.1016/S0022-0728(77)80224-6.
- [101] M. G. Albrecht and J. A. Creighton. Anomalously intense Raman spectra of pyridine at a silver electrode. *Journal of the American Chemical Society*, 99(15):5215–5217, 1977. doi: 10.1021/ja00457a071.
- [102] R. R. Nair, P. Blake, A. N. Grigorenko, K. S. Novoselov, T. J. Booth, T. Stauber, N. M. R. Peres, and A. K. Geim. Fine structure constant defines visual transparency of graphene. *Science*, 320(5881):1308, 2008. doi: 10.1126/science.1156965.
- [103] S. M. Sze. *Physics of semiconductor devices*. Interscience, New York, 2nd edition, 1981.
- [104] G. Giovannetti, P. A. Khomyakov, G. Brocks, V. M. Karpan, J. van den Brink, and P. J. Kelly. Doping graphene with metal contacts. *Physical Review Letters*, 101(2):026803–1–4, 2008. doi: 10.1103/physrevlett.101.026803.
- [105] M. Cutler and N. F. Mott. Observation of Anderson localization in an electron gas. *Physical Review*, 181(3):1336–1340, 1969. doi: 10.1103/physrev.181.1336.
- [106] Y. M. Zuev, W. Chang, and P. Kim. Thermoelectric and magnetothermoelectric transport measurements of graphene. *Physical Review Letters*, 102(9):096807–1–4, 2009. doi: 10.1103/physrevlett.102.096807.
- [107] P. Wei, W. Bao, Y. Pu, C. N. Lau, and J. Shi. Anomalous thermoelectric transport of Dirac particles in graphene. *Physical Review Letters*, 102(16):166808–1–4, 2009. doi: 10.1103/physrevlett.102.166808.
- [108] G. Binnig, C. F. Quate, and C. Gerber. Atomic force microscope. *Physical Review Letters*, 56(9):930–933, 1986. doi: 10.1103/physrevlett.56.930.

-
- [109] I. Horcas, R. Fernandez, J. M. Gomez-Rodriguez, J. Colchero, J. Gomez-Herrero, and A. M. Baro. WSxM: a software for scanning probe microscopy and a tool for nanotechnology. *Review of Scientific Instruments*, 78(1):013705–1–8, 2007. doi: 10.1063/1.2432410.
- [110] M. von Ardenne. Patent: improvements in electron microscopes. 1937.
- [111] C. V. Raman. The Nobel prize in physics 1930.
- [112] M. Minsky. Memoir on inventing the confocal scanning microscope. *Scanning*, 10(4):128–138, 1988.
- [113] J. Cai, P. Ruffieux, R. Jaafar, M. Bieri, T. Braun, S. Blankenburg, M. Muoth, A. P. Seitsonen, M. Saleh, X. Feng, K. Müllen, and R. Fasel. Atomically precise bottom-up fabrication of graphene nanoribbons. *Nature*, 466(7305):470–473, 2010. doi: 10.1038/nature09211.
- [114] L. Jiao, X. Wang, G. Diankov, H. Wang, and H. Dai. Facile synthesis of high-quality graphene nanoribbons. *Nature Nanotechnology*, 5(5):321–325, 2010. doi: 10.1038/nnano.2010.54.
- [115] L. Ci, Z. Xu, L. Wang, W. Gao, F. Ding, K. F. Kelly, B. I. Yakobson, and P. M. Ajayan. Controlled nanocutting of graphene. *Nano Research*, 1(2):116–122, 2008. doi: 10.1007/s12274-008-8020-9.
- [116] L. C. Campos, V. R. Manfrinato, J. D. Sanchez-Yamagishi, J. Kong, and P. Jarillo-Herrero. Anisotropic etching and nanoribbon formation in single-layer graphene. *Nano Letters*, 9(7):2600–2604, 2009. doi: 10.1021/nl900811r.
- [117] P. Nemes-Incze, G. Magda, K. Kamaras, and L. P. Biro. Crystallographically selective nanopatterning of graphene on SiO₂. *Nano Research*, 3(2):110–116, 2010. doi: 10.1007/s12274-010-1015-3.
- [118] Y.-M. Lin, V. Perebeinos, Z. Chen, and P. Avouris. Electrical observation of subband formation in graphene nanoribbons. *Physical Review B*, 78(16):161409–1–4, 2008. doi: 10.1103/physrevb.78.161409.
- [119] R. Sordan, M. Burghard, and K. Kern. Removable template route to metallic nanowires and nanogaps. *Applied Physics Letters*, 79(13):2073–2075, 2001. doi: 10.1063/1.1405813.
- [120] J. Bai, X. Duan, and Y. Huang. Rational fabrication of graphene nanoribbons using a nanowire etch mask. *Nano Letters*, 9(5):2083–2087, 2009. doi: 10.1021/nl900531n.

- [121] A. Fasoli, A. Colli, A. Lombardo, and A. C. Ferrari. Fabrication of graphene nanoribbons via nanowire lithography. *Physica Status Solidi B*, 246(11-12, SI):2514–2517, 2009. doi: 10.1002/pssb.200982356.
- [122] J. Muster, G. T. Kim, V. Krstic, J. G. Park, Y. W. Park, S. Roth, and M. Burghard. Electrical transport through individual vanadium pentoxide nanowires. *Advanced Materials*, 12(6):420–424, 2000. doi: 10.1002/(SICI)1521-4095(200003)12:6<420::AID-ADMA420>3.0.CO;2-7.
- [123] Z. Li, A. Kornowski, A. Myalitsin, and A. Mews. Formation and function of bismuth nanocatalysts for the solution-liquid-solid synthesis of CdSe nanowires. *Small*, 4(10):1698–1702, 2008. doi: 10.1002/smll.200800858.
- [124] G. Hodes. A thin-film polycrystalline photoelectrochemical cell with 8 percent solar conversion efficiency. *Nature*, 285(5759):29–30, 1980. doi: 10.1038/285029a0.
- [125] R. Gillen, M. Mohr, C. Thomsen, and J. Maultzsch. Vibrational properties of graphene nanoribbons by first-principles calculations. *Physical Review B*, 80(15):155418–1–9, 2009. doi: 10.1103/physrevb.80.155418.
- [126] R. Gillen, M. Mohr, and J. Maultzsch. Symmetry properties of vibrational modes in graphene nanoribbons. *Physical Review B*, 81(20):205426–1–9, 2010. doi: 10.1103/physrevb.81.205426.
- [127] N. Rosenkranz, C. Till, C. Thomsen, and J. Maultzsch. Ab initio calculations of edge-functionalized armchair graphene nanoribbons: structural, electronic, and vibrational effects. *Physical Review B*, 84(19):195438–1–7, 2011. doi: 10.1103/physrevb.84.195438.
- [128] L. Xie, H. Wang, C. Jin, X. Wang, L. Jiao, K. Suenaga, and H. Dai. Graphene nanoribbons from unzipped carbon nanotubes: atomic structures, Raman spectroscopy, and electrical properties. *Journal of the American Chemical Society*, 133(27):10394–10397, 2011. doi: 10.1021/ja203860a.
- [129] R. Yang, Z. Shi, L. Zhang, D. Shi, and G. Zhang. Observation of Raman G-peak split for graphene nanoribbons with hydrogen-terminated zigzag edges. *Nano Letters*, 11(10):4083–4088, 2011. doi: 10.1021/nl201387x.
- [130] D. Bischoff, J. Güttinger, S. Dröscher, T. Ihn, K. Ensslin, and C. Stampfer. Raman spectroscopy on etched graphene nanoribbons. *Journal of Applied Physics*, 109(7):073710–1–4, 2011. doi: 10.1063/1.3561838.

-
- [131] S. Ryu, J. Maultzsch, M. Y. Han, P. Kim, and L. E. Brus. Raman spectroscopy of lithographically patterned graphene nanoribbons. *ACS Nano*, 5(5):4123–4130, 2011. doi: 10.1021/nn200799y.
- [132] T. Assmus, K. Balasubramanian, M. Burghard, K. Kern, M. Scolari, N. Fu, A. Myalitsin, and A. Mews. Raman properties of gold nanoparticle-decorated individual carbon nanotubes. *Applied Physics Letters*, 90(17):173109–1–3, 2007. doi: 10.1063/1.2731662.
- [133] L. G. Cancado, M. A. Pimenta, B. R. A. Neves, M. S. S. Dantas, and A. Jorio. Influence of the atomic structure on the Raman spectra of graphite edges. *Physical Review Letters*, 93(24):247401–1–4, 2004. doi: 10.1103/physrevlett.93.247401.
- [134] F. Schedin, E. Lidorikis, A. Lombardo, V. G. Kravets, A. K. Geim, A. N. Grigorenko, K. S. Novoselov, and A. C. Ferrari. Surface-enhanced Raman spectroscopy of graphene. *ACS Nano*, 4(10):5617–5626, 2010. doi: 10.1021/nn1010842.
- [135] H. Zhou, C. Qiu, F. Yu, H. Yang, M. Chen, L. Hu, and L. Sun. Thickness-dependent morphologies and surface-enhanced Raman scattering of Ag deposited on n-layer graphenes. *Journal of Physical Chemistry C*, 115(23):11348–11354, 2011. doi: 10.1021/jp112421q.
- [136] X. Fu, F. Bei, X. Wang, S. O’Brien, and J. R. Lombardi. Excitation profile of surface-enhanced Raman scattering in graphene-metal nanoparticle based derivatives. *Nanoscale*, 2(8):1461–1466, 2010. doi: 10.1039/c0nr00135j.
- [137] H. Xu, Y. Chen, W. Xu, H. Zhang, J. Kong, M. S. Dresselhaus, and J. Zhang. Modulating the charge-transfer enhancement in GERS using an electrical field under vacuum and an n/p-doping atmosphere. *Small*, 7(20):2945–2952, 2011. doi: 10.1002/smll.201100546.
- [138] B. Huard, N. Stander, J. A. Sulpizio, and D. Goldhaber-Gordon. Evidence of the role of contacts on the observed electron-hole asymmetry in graphene. *Physical Review B*, 78(12):121402–1–4, 2008. doi: 10.1103/physrevb.78.121402.
- [139] A. Das, S. Pisana, B. Chakraborty, S. Piscanec, S. K. Saha, U. V. Waghmare, K. S. Novoselov, H. R. Krishnamurthy, A. K. Geim, A. C. Ferrari, and A. K. Sood. Monitoring dopants by Raman scattering in an electrochemically top-gated graphene transistor. *Nature Nanotechnology*, 3(4):210–215, 2008. doi: 10.1038/nnano.2008.67.

- [140] J. Yan, Y. Zhang, P. Kim, and A. Pinczuk. Electric field effect tuning of electron-phonon coupling in graphene. *Physical Review Letters*, 98(16):166802–1–4, 2007. doi: 10.1103/physrevlett.98.166802.
- [141] R. S. Sundaram, M. Steiner, H.-Y. Chiu, M. Engel, A. A. Bol, R. Krupke, M. Burghard, K. Kern, and P. Avouris. The graphene-gold interface and its implications for nanoelectronics. *Nano Letters*, 11(9):3833–3837, 2011. doi: 10.1021/nl201907u.
- [142] B. Standley, W. Bao, H. Zhang, J. Bruck, C. N. Lau, and M. Bockrath. Graphene-based atomic-scale switches. *Nano Letters*, 8(10):3345–3349, 2008. doi: 10.1021/nl801774a.
- [143] Y. Li, A. Sinitskii, and J. M. Tour. Electronic two-terminal bistable graphitic memories. *Nature Materials*, 7(12):966–971, 2008. doi: 10.1038/nmat2331.
- [144] A. Sinitskii and J. M. Tour. Lithographic graphitic memories. *ACS Nano*, 3(9):2760–2766, 2009. doi: 10.1021/nn9006225.
- [145] J. Yao, L. Zhong, Z. Zhang, T. He, Z. Jin, P. J. Wheeler, D. Natelson, and J. M. Tour. Resistive switching in nanogap systems on SiO₂ substrates. *Small*, 5(24):2910–2915, 2009. doi: 10.1002/smll.200901100.
- [146] H. Zhang, W. Bao, Z. Zhao, J.-W. Huang, B. Standley, G. Liu, F. Wang, P. Kratz, L. Jing, M. Bockrath, and C. N. Lau. Visualizing electrical breakdown and on/off states in electrically switchable suspended graphene break junctions. *Nano Letters*, 12(4):1772–1775, 2012. doi: 10.1021/nl203160x.
- [147] E. U. Stützel, M. Burghard, K. Kern, F. Traversi, F. Nichele, and R. Sordan. A graphene nanoribbon memory cell. *Small*, 6(24):2822–2825, 2010. doi: 10.1002/smll.201000854.
- [148] J. B. Cui, R. Sordan, M. Burghard, and K. Kern. Carbon nanotube memory devices of high charge storage stability. *Applied Physics Letters*, 81(17):3260–3262, 2002. doi: 10.1063/1.1516633.
- [149] M. Radosavljevic, M. Freitag, K. V. Thadani, and A. T. C. Johnson. Non-volatile molecular memory elements based on ambipolar nanotube field effect transistors. *Nano Letters*, 2(7):761–764, 2002. doi: 10.1021/nl025584c.
- [150] M. S. Fuhrer, B. M. Kim, T. Durkop, and T. Brintlinger. High-mobility nanotube transistor memory. *Nano Letters*, 2(7):755–759, 2002. doi: 10.1021/nl025577o.

-
- [151] D. Estrada, S. Dutta, A. Liao, and E. Pop. Reduction of hysteresis for carbon nanotube mobility measurements using pulsed characterization. *Nanotechnology*, 21(8):085702–1–7, 2010. doi: 10.1088/0957-4484/21/8/085702.
- [152] L. Marty, A. Iaia, M. Faucher, V. Bouchiat, C. Naud, M. Chaumont, T. Fournier, and A. M. Bonnot. Self-assembled single wall carbon nanotube field effect transistors and AFM tips prepared by hot filament assisted CVD. *Thin Solid Films*, 501(1-2):299–302, 2006. doi: 10.1016/j.tsf.2005.07.218.
- [153] M. Rinkio, A. Johansson, G. S. Paraoanu, and P. Törmä. High-speed memory from carbon nanotube field-effect transistors with high-kappa gate dielectric. *Nano Letters*, 9(2):643–647, 2009. doi: 10.1021/nl8029916.
- [154] W. Kim, A. Javey, O. Vermesh, O. Wang, Y. M. Li, and H. Dai. Hysteresis caused by water molecules in carbon nanotube field-effect transistors. *Nano Letters*, 3(2):193–198, 2003. doi: 10.1021/nl0259232.
- [155] J. S. Lee, S. Ryu, K. Yoo, I. S. Choi, W. S. Yun, and J. Kim. Origin of gate hysteresis in carbon nanotube field-effect transistors. *Journal of Physical Chemistry C*, 111(34):12504–12507, 2007. doi: 10.1021/jp074692q.
- [156] T. O. Wehling, A. I. Lichtenstein, and M. I. Katsnelson. First-principles studies of water adsorption on graphene: the role of the substrate. *Applied Physics Letters*, 93(20):202110–1–3, 2008. doi: 10.1063/1.3033202.
- [157] A. Di Bartolomeo, M. Rinzan, A. K. Boyd, Y. Yang, L. Guadagno, F. Giubileo, and P. Barbara. Electrical properties and memory effects of field-effect transistors from networks of single- and double-walled carbon nanotubes. *Nanotechnology*, 21(11):115204–1–9, 2010. doi: 10.1088/0957-4484/21/11/115204.
- [158] D. B. Asay, A. L. Barnette, and S. H. Kim. Effects of surface chemistry on structure and thermodynamics of water layers at solid-vapor interfaces. *Journal of Physical Chemistry C*, 113(6):2128–2133, 2009. doi: 10.1021/jp806815p.
- [159] M. Lafkioti, B. Krauss, T. Lohmann, U. Zschieschang, H. Klauk, K. von Klitzing, and J. H. Smet. Graphene on a hydrophobic substrate: doping reduction and hysteresis suppression under ambient conditions. *Nano Letters*, 10(4):1149–1153, 2010. doi: 10.1021/nl903162a.
- [160] F. Bonaccorso, Z. Sun, T. Hasan, and A. C. Ferrari. Graphene photonics and optoelectronics. *Nature Photonics*, 4(9):611–622, 2010. doi: 10.1038/nphoton.2010.186.

- [161] H. Zhang, Q. Bao, D. Tang, L. Zhao, and K. Loh. Large energy soliton erbium-doped fiber laser with a graphene-polymer composite mode locker. *Applied Physics Letters*, 95(14):141103–1–3, 2009. doi: 10.1063/1.3244206.
- [162] F. Xia, T. Müller, Y.-M. Lin, A. Valdes-Garcia, and P. Avouris. Ultrafast graphene photodetector. *Nature Nanotechnology*, 4(12):839–843, 2009. doi: 10.1038/nnano.2009.292.
- [163] T. Müller, F. Xia, and P. Avouris. Graphene photodetectors for high-speed optical communications. *Nature Photonics*, 4(5):297–301, 2010. doi: 10.1038/nphoton.2010.40.
- [164] E. J. H. Lee, K. Balasubramanian, R. T. Weitz, M. Burghard, and K. Kern. Contact and edge effects in graphene devices. *Nature Nanotechnology*, 3(8):486–490, 2008. doi: 10.1038/nnano.2008.172.
- [165] F. Xia, T. Müller, R. Golizadeh-Mojarad, M. Freitag, Y.-M. Lin, J. Tsang, V. Perebeinos, and P. Avouris. Photocurrent imaging and efficient photon detection in a graphene transistor. *Nano Letters*, 9(3):1039–1044, 2009. doi: 10.1021/nl8033812.
- [166] J. Park, Y. H. Ahn, and C. Ruiz-Vargas. Imaging of photocurrent generation and collection in single-layer graphene. *Nano Letters*, 9(5):1742–1746, 2009. doi: 10.1021/nl8029493.
- [167] T. Müller, F. Xia, M. Freitag, J. Tsang, and P. Avouris. Role of contacts in graphene transistors: a scanning photocurrent study. *Physical Review B*, 79(24):245430–1–6, 2009. doi: 10.1103/physrevb.79.245430.
- [168] L. Prectel, L. Song, D. Schuh, P. Ajayan, W. Wegscheider, and A. W. Holleitner. Time-resolved ultrafast photocurrents and terahertz generation in freely suspended graphene. *Nature Communications*, 3:1–7, 2012. doi: 10.1038/ncomms1656.
- [169] X. Xu, N. M. Gabor, J. S. Alden, A. M. van der Zande, and P. L. McEuen. Photo-thermoelectric effect at a graphene interface junction. *Nano Letters*, 10(2):562–566, 2010. doi: 10.1021/nl903451y.
- [170] E. C. Peters, E. J. H. Lee, M. Burghard, and K. Kern. Gate dependent photocurrents at a graphene p-n junction. *Applied Physics Letters*, 97(19):193102–1–3, 2010. doi: 10.1063/1.3505926.

-
- [171] M. C. Lemme, F. H. L. Koppens, A. L. Falk, M. S. Rudner, H. Park, L. S. Levitov, and C. M. Marcus. Gate-activated photoresponse in a graphene p-n junction. *Nano Letters*, 11(10):4134–4137, 2011. doi: 10.1021/nl2019068.
- [172] A. Urich, K. Unterrainer, and T. Müller. Intrinsic response time of graphene photodetectors. *Nano Letters*, 11(7):2804–2808, 2011. doi: 10.1021/nl2011388.
- [173] D. Sun, G. Aivazian, A. M. Jones, J. S. Ross, W. Yao, D. Cobden, and X. Xu. Ultrafast hot-carrier-dominated photocurrent in graphene. *Nature Nanotechnology*, 7(2):114–118, 2012. doi: 10.1038/nnano.2011.243.
- [174] T. J. Echtermeyer, L. Britnell, P. K. Jasnós, A. Lombardo, R. V. Gorbachev, A. N. Grigorenko, A. K. Geim, A. C. Ferrari, and K. S. Novoselov. Strong plasmonic enhancement of photovoltage in graphene. *Nature Communications*, 2:1–5, 2011. doi: 10.1038/ncomms1464.
- [175] Y. Liu, R. Cheng, L. Liao, H. Zhou, J. Bai, G. Liu, L. Liu, Y. Huang, and X. Duan. Plasmon resonance enhanced multicolour photodetection by graphene. *Nature Communications*, 2:1–7, 2011. doi: 10.1038/ncomms1589.
- [176] M. Furchi, A. Urich, A. Pospischil, G. Lilley, K. Unterrainer, H. Detz, P. Klang, A. M. Andrews, W. Schrenk, G. Strasser, and T. Müller. Microcavity-integrated graphene photodetector. *Nano Letters*, 12(6):2773–2777, 2012. doi: 10.1021/nl204512x.
- [177] X. Li, X. Wang, L. Zhang, S. Lee, and H. Dai. Chemically derived, ultrasmooth graphene nanoribbon semiconductors. *Science*, 319(5867):1229–1232, 2008. doi: 10.1126/science.1150878.
- [178] V. Ryzhii, V. Mitin, M. Ryzhii, N. Ryabova, and T. Otsuji. Device model for graphene nanoribbon phototransistor. *Applied Physics Express*, 1(6):063002–1–3, 2008. doi: 10.1143/apex.1.063002.
- [179] G. Xu, C. M. Torres, Jr., J. Tang, J. Bai, E. B. Song, Y. Huang, X. Duan, Y. Zhang, and K. L. Wang. Edge effect on resistance scaling rules in graphene nanostructures. *Nano Letters*, 11(3):1082–1086, 2011. doi: 10.1021/nl103966t.
- [180] Y. Lu, B. Goldsmith, D. R. Strachan, J. H. Lim, Z. Luo, and A. T. C. Johnson. High-on/off-ratio graphene nanoconstriction field-effect transistor. *Small*, 6(23):2748–2754, 2010. doi: 10.1002/smll.201001324.
- [181] S.-F. Shi, X. Xu, D. C. Ralph, and P. L. McEuen. Plasmon resonance in individual nanogap electrodes studied using graphene nanoconstrictions as photodetectors. *Nano Letters*, 11(4):1814–1818, 2011. doi: 10.1021/nl200522t.

- [182] M. Freitag, T. Low, F. Xia, and P. Avouris. Photoconductivity of biased graphene. *Nature Photonics*, 7(1):53–59, 2013. doi: 10.1038/nphoton.2012.314.
- [183] S. Kim, J. Nah, I. Jo, D. Shahrjerdi, L. Colombo, Z. Yao, E. Tutuc, and S. K. Banerjee. Realization of a high mobility dual-gated graphene field-effect transistor with Al_2O_3 dielectric. *Applied Physics Letters*, 94(6):062107–1–3, 2009. doi: 10.1063/1.3077021.
- [184] A. D. Liao, J. Z. Wu, X. Wang, K. Tahy, D. Jena, H. Dai, and E. Pop. Thermally limited current carrying ability of graphene nanoribbons. *Physical Review Letters*, 106(25):256801–1–4, 2011. doi: 10.1103/physrevlett.106.256801.
- [185] H. Lee, M. L. Cohen, and S. G. Louie. Selective functionalization of halogens on zigzag graphene nanoribbons: a route to the separation of zigzag graphene nanoribbons. *Applied Physics Letters*, 97(23):233101–1–3, 2010. doi: 10.1063/1.3523252.
- [186] N. Jung, N. Kim, S. Jockusch, N. J. Turro, P. Kim, and L. Brus. Charge transfer chemical doping of few layer graphenes: charge distribution and band gap formation. *Nano Letters*, 9(12):4133–4137, 2009. doi: 10.1021/nl902362q.
- [187] S. W. Chu, S. J. Baek, D. C. Kim, S. Seo, J. S. Kim, and Y. W. Park. Charge transport in graphene doped with diatomic halogen molecules (I_2 , Br_2) near Dirac point. *Synthetic Metals*, 162(17-18):1689–1693, 2012. doi: 10.1016/j.synthmet.2012.06.008.
- [188] C. O. Girit, J. C. Meyer, R. Erni, M. D. Rossell, C. Kisielowski, L. Yang, C.-H. Park, M. F. Crommie, M. L. Cohen, S. G. Louie, and A. Zettl. Graphene at the edge: stability and dynamics. *Science*, 323(5922):1705–1708, 2009. doi: 10.1126/science.1166999.
- [189] F. Schäffel, M. Wilson, A. Bachmatiuk, M. H. Rummeli, U. Queitsch, B. Rellinghaus, G. A. D. Briggs, and J. H. Warner. Atomic resolution imaging of the edges of catalytically etched suspended few-layer graphene. *ACS Nano*, 5(3):1975–1983, 2011. doi: 10.1021/nn103035y.
- [190] C. L. Tan, Z. B. Tan, K. Wang, L. Ma, F. Yang, , F. M. Qu, J. Chen, C. L. Yang, and L. Lu. Observations of two-fold shell filling and Kondo effect in a graphene nano-ribbon quantum dot device. *arXiv.org*, arXiv:0910.5777, 2009.
- [191] X. Wang, Y. Ouyang, L. Jiao, H. Wang, L. Xie, J. Wu, J. Guo, and H. Dai. Graphene nanoribbons with smooth edges behave as quantum wires. *Nature Nanotechnology*, 6(9):563–567, 2011. doi: 10.1038/nnano.2011.138.

-
- [192] J. Nygard, D. H. Cobden, and P. E. Lindelof. Kondo physics in carbon nanotubes. *Nature*, 408(6810):342–346, 2000. doi: 10.1038/35042545.
- [193] A. Makarovski, J. Liu, and G. Finkelstein. Evolution of transport regimes in carbon nanotube quantum dots. *Physical Review Letters*, 99(6):066801–1–4, 2007. doi: 10.1103/physrevlett.99.066801.
- [194] J.-H. Chen, L. Li, W. G. Cullen, E. D. Williams, and M. S. Fuhrer. Tunable Kondo effect in graphene with defects. *Nature Physics*, 7(7):535–538, 2011. doi: 10.1038/nphys1962.
- [195] J. Jobst and H. B. Weber. Origin of logarithmic resistance correction in graphene. *Nature Physics*, 8(5):352, 2012. doi: 10.1038/nphys2297.
- [196] J.-H. Chen, L. Li, W. G. Cullen, E. D. Williams, and M. S. Fuhrer. Origin of logarithmic resistance correction in graphene, reply. *Nature Physics*, 8(5):353, 2012. doi: 10.1038/nphys2306.
- [197] S. Dröscher, H. Knowles, Y. Meir, K. Ensslin, and T. Ihn. Coulomb gap in graphene nanoribbons. *Physical Review B*, 84(7):073405–1–6, 2011. doi: 10.1103/physrevb.84.073405.
- [198] T. Ihn. *Electronic quantum transport in mesoscopic semiconductor structures*. Springer, 1st edition, 2004.
- [199] J. Güttinger, C. Stampfer, F. Libisch, T. Frey, J. Burgdörfer, T. Ihn, and K. Ensslin. Electron-hole crossover in graphene quantum dots. *Physical Review Letters*, 103(4):046810–1–4, 2009. doi: 10.1103/physrevlett.103.046810.
- [200] J. B. Oostinga, B. Sacepe, M. F. Craciun, and A. F. Morpurgo. Magnetotransport through graphene nanoribbons. *Physical Review B*, 81(19):193408–1–4, 2010. doi: 10.1103/physrevb.81.193408.
- [201] J. Bai, R. Cheng, F. Xiu, L. Liao, M. Wang, A. Shailos, K. L. Wang, Y. Huang, and X. Duan. Very large magnetoresistance in graphene nanoribbons. *Nature Nanotechnology*, 5(9):655–659, 2010. doi: 10.1038/nnano.2010.154.
- [202] J.-M. Poumirol, A. Cresti, S. Roche, W. Escoffier, M. Goiran, X. Wang, X. Li, H. Dai, and B. Raquet. Edge magnetotransport fingerprints in disordered graphene nanoribbons. *Physical Review B*, 82(4):041413–1–4, 2010. doi: 10.1103/physrevb.82.041413.

- [203] M. Bockrath, D. H. Cobden, P. L. McEuen, N. G. Chopra, A. Zettl, A. Thess, and R. E. Smalley. Single-electron transport in ropes of carbon nanotubes. *Science*, 275(5308):1922–1925, 1997. doi: 10.1126/science.275.5308.1922.
- [204] P. Jarillo-Herrero, S. Sapmaz, C. Dekker, L. P. Kouwenhoven, and H. S. J. van der Zant. Electron-hole symmetry in a semiconducting carbon nanotube quantum dot. *Nature*, 429(6990):389–392, 2004. doi: 10.1038/nature02568.
- [205] S. Schnez, F. Molitor, C. Stampfer, J. Güttinger, I. Shorubalko, T. Ihn, and K. Ensslin. Observation of excited states in a graphene quantum dot. *Applied Physics Letters*, 94(1):012107–1–3, 2009. doi: 10.1063/1.3064128.
- [206] J. Kondo. Resistance minimum in dilute magnetic alloys. *Progress of Theoretical Physics*, 32(1):37–49, 1964. doi: 10.1143/ptp.32.37.
- [207] T. Ihn. *Semiconductor nanostructures*. Oxford University Press, 1st edition, 2010.
- [208] M. Grobis, I. G. Rau, R. M. Potok, and D. Goldhaber-Gordon. *Handbook of magnetism and advanced magnetic materials, volume 5: spintronics and magnetoelectronics, chapter: the Kondo effect in mesoscopic quantum dots*. John Wiley & Sons, 2007.
- [209] B. Terres, J. Dauber, C. Volk, S. Trellenkamp, U. Wichmann, and C. Stampfer. Disorder induced Coulomb gaps in graphene constrictions with different aspect ratios. *Applied Physics Letters*, 98(3):032109–1–3, 2011. doi: 10.1063/1.3544580.
- [210] X. Zhang, O. V. Yazyev, J. Feng, L. Xie, C. Tao, Y.-C. Chen, L. Jiao, Z. Pedramrazi, A. Zettl, S. G. Louie, H. Dai, and M. F. Crommie. Experimentally engineering the edge termination of graphene nanoribbons. *ACS Nano*, XXX(X):000–000, ASAP. doi: 10.1021/nn303730v.
- [211] S. Lisenkov, A. N. Andriotis, and M. Menon. Magnetic anisotropy and engineering of magnetic behavior of the edges in Co embedded graphene nanoribbons. *Physical Review Letters*, 108(18):187208–1–5, 2012. doi: 10.1103/physrevlett.108.187208.
- [212] K. Pi, K. M. McCreary, W. Bao, W. Han, Y. F. Chiang, Y. Li, S.-W. Tsai, C. N. Lau, and R. K. Kawakami. Electronic doping and scattering by transition metals on graphene. *Physical Review B*, 80(7):075406–1–5, 2009. doi: 10.1103/physrevb.80.075406.

- [213] A. Chuvilin, E. Bichoutskaia, M. C. Gimenez-Lopez, T. W. Chamberlain, G. A. Rance, N. Kuganathan, J. Biskupek, U. Kaiser, and A. N. Khlobystov. Self-assembly of a sulphur-terminated graphene nanoribbon within a single-walled carbon nanotube. *Nature Materials*, 10(9):687–692, 2011. doi: 10.1038/nmat3082.
- [214] D.-K. Ki and A. F. Morpurgo. Crossover from coulomb blockade to quantum Hall effect in suspended graphene nanoribbons. *Physical Review Letters*, 108(26):266601–1–5, 2012. doi: 10.1103/physrevlett.108.266601.
- [215] D. Bischoff, T. Krähenmann, S. Dröscher, M. A. Gruner, C. Barraud, T. Ihn, and K. Ensslin. Reactive-ion-etched graphene nanoribbons on a hexagonal boron nitride substrate. *Applied Physics Letters*, 101(20):203103–1–4, 2012. doi: 10.1063/1.4765345.

Curriculum vitae

Personal information

Name	Eberhard Ulrich Stützel
Date of birth	29.03.1984
Place of birth	Esslingen am Neckar, Germany
Nationality	German

Education

April 2009	Research staff at the Max-Planck Institute for Solid State Research Stuttgart, Germany, Nanoscale Science Department of Prof. Klaus Kern, Dr. Marko Burghard (Quantum Materials group) PhD student at the Ecole Polytechnique Fédérale de Lausanne, Switzerland
Dec. 2008 - Feb. 2009	Research staff at the Technical University of Munich, Germany Walter Schottky Institute, Prof. Stutzmann, Experimental Semiconductor Physics
Nov. 2007 - Nov. 2008	Diploma thesis (equivalent to Master of Science degree) Technical University of Munich, Germany Walter Schottky Institute, Prof. Stutzmann, Experimental Semiconductor Physics, Dr. Jose Antonio Garrido (Diamond group) Title: Surface conductivity at the diamond electrolyte interface
Oct. 2005 - Oct. 2007	Diploma in physics Technical University of Munich, Germany
Oct. 2003 - Oct. 2005	Intermediate diploma in physics University of Constance, Germany
June 2003	Abitur (university entrance diploma) Alexander-von-Humboldt-Gymnasium Constance, Germany

Acknowledgements

The past 3 1/2 years at the Max-Planck Institute for Solid State Research in Stuttgart were very special to me. Not only did I have a good time, but I was also able to learn a lot. I want to say thank you to the following people, that directly or indirectly helped and supported me with this thesis.

First of all, I would like to thank **Prof. Klaus Kern** for supervising my thesis and giving me the opportunity to work on my PhD in his Nanoscale Science Department.

Many thanks also go to **Dr. Marko Burghard**, my direct advisor, for giving me the opportunity to work in his group. I would like to thank him for providing me with such an interesting topic, his guidance, our many discussions, and the continuous support.

I am also very grateful to **Dr. Kannan Balasubramanian**, **Dr. Thomas Dufaux** and **Pascal Gehring**. They helped me with so many things, that it is not possible to list them here.

Thanks to the people from L-NESS in Como for the valuable and scientific cooperation, specifically to **Dr. Roman Sordan**, **Laura Rizzi** and **Laura Polloni**.

Special thanks also go to **Dr. Stephan Rauschenbach** and **Gordon Rinke** for valuable discussions and STM measurements on graphene nanostructures.

Thanks to **Robert Preuss** for the numerous attempts to unzip carbon nanotubes, and his technical and scientific support of the functionalization of graphene.

Thanks to **Dr. Zhe Wang** and **Prof. Alf Mews** for providing CdSe nanowires.

My thanks also go to **Sebastian Lechner** and **Dr. Ilia Platzman** for their assistance with hydrogen plasma.

I also thank **Nils Scheuschner** and **Prof. Janina Maultzsch** for Raman measurements and **Simon Kurasch** and **Prof. Ute Kaiser** for TEM measurements

on Br₂-treated graphene samples.

Sabine Birtel, thank you, for your great help with all the administrative stuff.

I very much appreciated the continuous technical support related to the clean room facilities by **Marion Hagel**, **Thomas Reindl**, **Ulrike Waizmann** and **Achim Güth**, and also **Martin Siemens**, **Marko Memmler** and **Wolfgang Stiepany** who assisted me with all the electrical equipment and constructed several sample holders.

My thanks also go to the other department members who supported me in my work like **Dr. Theresa Lutz**, **Eva Carmen Peters**, **Dr. Adarsh Sagar**, **Dr. Ravi Shankar Sundaram**, **Dr. Bo Gao** and **Moritz Eßlinger**.

My time at the Max-Planck Institute wouldn't have been so nice without my colleagues **Tobias Herden**, **Steffen Kahle**, **Sören Krotzky**, **Dr. Markus Ternes**, **Carola Straßer**, **Janina Krieg**, **Dr. Tetiana Kurkina**, **Nassim Rafiefard**, **Dr. Vivek Pachauri**, **Dr. Amit Kumar**, **Gaurav Pathak**, **Kristina Vaklinova**, **Christian Cervetti** and **Alexander Hoyer**.

Finally, I am grateful to **my family**, who always support me in so many different ways, and especially to my wife, **Chaya**, for her love and support.

